UNIVERSITY OF OSLO
Department of Physics

Stability of the Large Low Shear Velocity Provinces: Thermomechanical modeling

Master thesis in Physics of Geological Processes

Elvira Mulyukova

June 3, 2011

Preface

My friend Kristin Paulsen, a former student at PGP, once told me that to do a Master's project is a once in a lifetime opportunity to do research without having to worry about getting published, or getting financed. I feel extremely lucky to have had the opportunity to follow my curiousity when working on this project. I feel even more lucky to have had a supervisor, Marcin Dabrowski, who kept me inspired this entire year. Dear Marcin, I realize how much of your time and patience I demanded throughout this project. You have learned my flaws and my strengths and found a way to make me a better scientist. I am very grateful to you for making this year so enriching and fun.
I have been truly lucky to get all the help I needed to make the most out of this project. Inspiring and refreshing perspective on geology, thanks to my second supervisor Trond H. Torsvik. Making me laugh at my own mistakes, without making me want to quit and run, thanks to my third supervisor Dani W. Schmid. Decyphering of the geoid anomalies, thanks to Stephanie Werner. Finding the water content in the deepest mantle, thanks to Oliver Plumper. Getting me excited about space, volcanoes, tsunamies and the equation of state for dusty gas, thanks to Galen Gisler. Forcing me off my chair and making me run till my feet fall off, thanks to Maya Kobchenko. Preparing me for all the horrors and joys of a PhD project, thanks to Kirsten Firstad. Fixing the embarassing Rayleigh number definition, thanks to Sergey Medvedev. Communicating with my computer, when all I want to do is throw it out the window, thanks to Marcin Krotkewski. Staying calm and repressing my panick the night before the Master's thesis deadline, thanks to Hkon Storheim.
It is a unique experience to be a Master's student at PGP, and this has been two years I will never forget. The room 437B started to feel like home shortly after I started here. This is the place where my friends come and meet me, because they know they can always find me here. This is the place where my mom comes and visits me, and delivers food to me knowing that I won't have time for a proper meal. This is where my sister comes and drags me out to town so I can remember what youth is all about. This is where I can express my frustration and not feel bad about it, knowing that tomorrow someone else will do exactly the same. Kristin Myhra, sweety, I am so happy that I got to share this two years with you! It is truly amazing how honest we are with each other and yet managed not to have a single fight for two years! Sweet Marta Adamuszek, I just don't know what I would do without you. You have made me feel so safe, giving me the right perspective on things when I was just being negative. Liene Spruzeniece, the funniest Latvian girl I ever met, you and your candy surely will be missED. ystein T. Haug, baby, I have really been a nerdy girlfriend, and I'm amazed how you put up with my lifestyle. Thank you for giving me all the support and understanding I need. You're the best!
This has been a great two years at PGP. I have gained a lot from studying in this group and I hope it will be reflected in this thesis. Enjoy the reading.

Elvira

Contents

Chapter 1

Results from other studies

We study the thermomechanical processes that are taking place within the Earth's interior. The current state of knowledge about this subject is based on interpretations of the surface measurements done by several geophysical studies, with additional insights provided by geodynamic modelling. We attempt to collect evidence from several disciplines: seismology, experimental mineral physics and geodynamic modeling. In this chapter, we present an overview over features in the lower mantle that are most robustly observed in other studies, and outline their influence on the convective flow of the mantle.

1.1 Parameters representative for the Mantle

An overview over physical parameters that govern mantle flow and their representative values are summarized in this section. These values are chosen from a range of results from several experimental and seismological studies.
The radial distributions of density, pressure and gravitational acceleration, according to the Preliminary Reference Earth Model (PREM) (Dziewonski and Anderson, 1981), are presented in Figure 1.1. These distributions are based on a range of values from a large set of data from astronomic geodesy, free oscillation and long-period surface waves, and body waves. A reference value for the dynamic viscosity of the mantle is chosen based on a study of post-glacial rebound (Peltier, 1996). The preferred values of parameters that we use in this study, including the dimensionless parameters, are presented in Table 1.1.

Anchor temperatures from phase transitions

Temperature values can be deduced for the depths of the mantle where seismic discontinuities are observed. The pressure and temperature conditions for the solid-state phase changes associated with these discontinuities can be estimated experimentally. The seismic

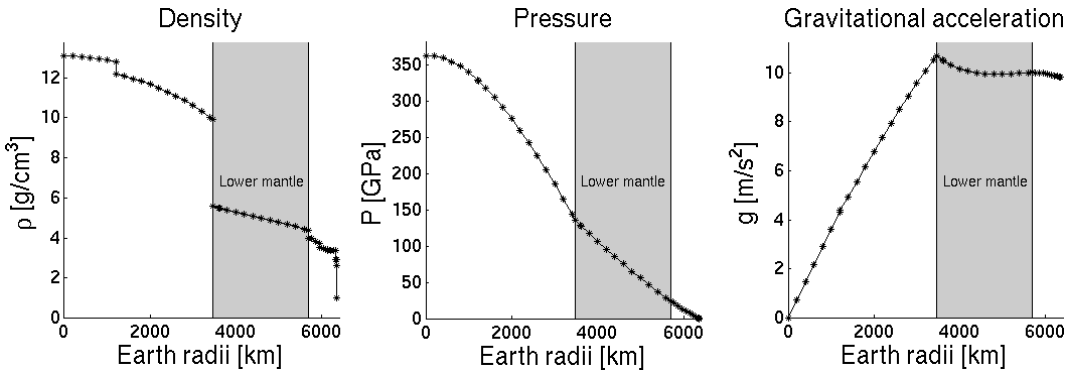

Figure 1.1: Radial distributions of density, pressure and gravitational acceleration in the Earth, based on the Preliminary Reference Earth Model (PREM) (Dziewonski and Anderson, 1981).

Dimensionless parameters	Values representative for the mantle	
$Ra \equiv \frac{\alpha g \rho \triangle T D^3}{\kappa \eta}$	g – gravitational constant $\approx 10 ms^{-2}$ α – thermal expansivity $\approx 3 \cdot 10^{-5} K^{-1}$ ρ – density $\approx 4 \cdot 10^3 kgm^{-3}$ $\triangle T$ – nonadiabatic temperature variations $\approx 10^3 K$	$Ra \approx 10^7$
$Pe \equiv \frac{Du}{\kappa}$	D – depth of the convecting region $\approx 3 \cdot 10^6 m$ κ – thermal diffusivity $\approx 10^{-6} m^2 s^{-1}$ η – dynamic viscosity $\approx 10^{21} Pas$ u – vertical velocity $\approx 10^{-2} myr^{-1} = 3 \cdot 10^{-10} ms^{-1}$	$Pe \approx 10^3$
$Pr \equiv \frac{\eta c_p}{k}$	c_p – specific heat $\approx 1 kJ(kgK)^{-1}$ k – thermal conductivity $\approx 4 W(mK)^{-1}$ E – Young's modulus $\approx 70 GPa$	$Pr \approx 2.5 \cdot 10^{23}$

Table 1.1: Table of the dimensionless parameters that are commonly used to characterize mantle properties and flow. Ra is the Rayleigh number, defined as the ratio of time scales of buoyancy forces driving convection and the dissipative effects opposing convection. Pe is the Peclet number, defined as the ratio of time scales for the conductive and convective heat transports. Pr is the Prandtl number, defined as the ratio of momentum diffusivity to thermal diffusivity. Values of the constituting physical parameters, representative of the Earth's mantle, are also included (Davies and Christensen, 2001) and (Schubert et al., 2001). These are the preferred values that we use for scaling analysis, the actual values may deviate up to a few orders of magnitude within the mantle.

Boundary	Depth [km]	Temperature [K]	Reference
MORB generation	50	$1590 - 1750$ †	Kinsler and Grove[1992]
Olivine-Wadsleyite	410	1760 ± 45	Katsura et al.[2004]
Post-spinel	660	1870 ± 50	Katsura et al.[2003, 2004]
Core-mantle	2900	4200 ± 500	Alfe et al.[2002]; Labrosse[2003]

Table 1.2: Anchor points for the mantle geotherm, deduced from seismic discontinuities and the associated solid-state phase changes (Jaupart et al., 2007). † indicates true range of temperatures in the upper mantle.

discontinuity at the 410 km depth is linked to the olivine-wadsleyite transition. Based on this phase change, the temperature of 1760 ± 45 K has been determined for this depth. The discontinuity at 660 km depth is linked to the dissociation of spinel to perovskite and magnetowustite. The temperature required for this phase change at the given depth is 1870 ± 50 K (Jaupart et al., 2007).
The outer core mainly consists of molten iron, while the lower mantle surrounding the core consists predominantly of silicates and oxides. The temperature at the CMB is therefore constrained by two conditions: it must be above the melting point of the iron alloy and below the melting point of the silicates and oxides. Another constraint is based on the assumption that the outer core is vigorously convecting and its geotherm is therefore an adiabat, as will be discussed in Section 1.2.4. The temperature at the inner core-outer core interface, inferred from the melting points, can thus be adiabatically extrapolated to the top of the core. Using these constraints, the temperature of $4400(\pm 600)$ K has been determined for the CMB (Jeanloz and Morris, 1986). The anchor points for the temperatures in the mantle are summarized in Table 1.2.

Rheology of the mantle

We argue that the mantle behaves like a fluid over geological time scales. An observational evidence for this is the vertical rebound of the Earth's surface over the last $10,000$ yr, as the crust has been relieved from the Pleistocene ice sheets (Jeanloz and Morris, 1986).
The rheological behavior of the mantle can also be inferred from its viscoelastic relaxation time, given by:

$$\tau_{ve} \equiv \frac{\eta}{E} \tag{1.1}$$

where η and E are the dynamic viscosity and the Young's modulus, respectively. The viscoelastic relaxation time characterizes the ability of a material to respond elastically or by viscous creep to an applied stress. Elastic behavior is observed over time scales much shorter than τ_{ve}, while fluid behavior is observed over time scales much longer than τ_{ve} (Schubert et al., 2001). Using the representative values listed in Table 1.1, we obtain $\tau_{ve} = 450$ yr. Comparing this value with the subduction time scales, which are millions of

years, explains that the mantle behaves like a fluid over time scales appropriate for tectonic plate motions (Hager, 1984).

1.2 Heat Transport in the Mantle

Heat loss and heat production are the main contribution to the Earth's total energy variation with time. Conduction, convection and radiation are the three general mechanisms for the transfer of heat. In this section we discuss these mechanisms and their relative efficiency in the mantle.

1.2.1 Heat budget

Comparing the amount of heat generation and heat loss in the mantle reveals that the mantle is cooling. The dominant heat sources are the heat flux from the core and the internal heat production by the radioactive elements, such as Uranium, Thorium and Potassium. Evidence for the heating of the mantle from below is based on the existence of a geomagnetic field, which implies that there are electric currents within the core. The ohmic heating generated by these currents must be transferred to the mantle to avoid a rising temperature within the core (Loper and Lay, 1995). These two heat sources sum up to an approximate heat generation rate of 21 TW (Jaupart et al., 2007). Excluding the contribution of the radioactive sources in the continental lithosphere from the total surface heat flux, the rate of heat loss from the mantle is 39 TW. Hence, the mantle is cooling at an approximate rate of 18 TW (Jaupart et al., 2007).

1.2.2 Convection

Convective heat transport involves motion of a fluid as response to a gravitational instability that arises when the density of the fluid changes due to temperature variations. The occurence of convection and its intensity in the mantle can be established by considering the Rayleigh number, which is the ratio of timescales of buoyancy forces driving convection and the dissipative effects opposing convection (Davies and Christensen, 2001). A detailed discussion about the Rayleigh number can be found in Section 2.2.5. For the mantle, temperature is the dominant factor determining the Rayleigh number. The value of the latter is estimated to lie between 10^5 and 10^9 (Jeanloz and Morris, 1986), as is demonstrated in Table 1.1. This implies vigorous convection in the Earth's mantle. The timescale of this convective motion, inferred from plate tectonics, is $10^7 - 10^9$ years (Loper and Lay, 1995).

1.2.3 Conduction

In most of the mantle radiation has shown to be a relatively ineffective heat transport mechanism due to the opacity of mantle minerals (Jeanloz and Morris, 1986). Combining the radiative and conductive heat transports, however, results in an effective heat transport mechanism in regions where convection cannot take place. An example of such location is the core-mantle boundary (CMB). The large density difference across this interface, 4.3 x $10^3 kg/m^3$, and the large viscosity ratio, $20 - 24$ orders of magnitude, prohibit the convective motions in this region (Loper and Lay, 1995). Thermal boundary layers develop on both sides of the interface across which a changeover from conduction to convection takes place. The temperature increase with depth is largest in these layers, compared to the other regions of the mantle (Jeanloz and Morris, 1986).

Thermal boundary layers at CMB

Some inferences can be made about the thermal boundary layers on both sides of the CMB, based on what is believed to be the main components of the core and the mantle. The iron-alloy outer core is believed to be a vigorously convecting fluid with a high thermal conductivity and a low viscosity, near that of water. The thermal boundary layer at the core-side of the CMB is therefore presumably thin, with a relatively uniform lateral temperature distribution within. The silicate-oxide mantle has a low thermal conductivity and a very high, temperature-dependent viscosity. The thermal boundary layer at the mantle-side of the CMB is therefore presumably thicker than the one inside the core, with a large temperature increase and a substantial viscosity reduction across it, the exact magnitudes of which are quite uncertain (Loper and Lay, 1995).

1.2.4 Efficiency of the convection and conduction

The heat transfer mechanism that dominates in the mantle may be established by considering the Peclet number, which is the ratio of conductive to advective time scales required to transport heat over a given distance. In the mantle, the Peclet number is much larger than one, as demonstrated in Table 1.1, implying that the convective heat transport is far more efficient on a global scale than conduction (Jeanloz and Morris, 1986).
A parameter that is used to describe the contribution of convection to the total heat flux is the Nusselt number, Nu. It is the ratio between the heat flux across the thermal boundary layer, $q_{TBL} = k\frac{\triangle T_{TBL}}{D_{TBL}}$, and the heat flux across the entire region if there were no convection, $q = k\frac{\triangle T}{D}$. Here, k is the thermal conductivity, $\triangle T_{TBL}$, $\triangle T$, and D_{TBL}, D are temperature differences across and the depths of the thermal boundary layer and the entire region, respectively. The Fourier's law of conduction is used to express the thermal fluxes. In cases of purely conductive heat transfer, $Nu = 1$. On the contrary, in case of vigorous convection, $Nu \gg 1$. It can be shown by dimensionless analysis that, except for some deviations due

to variable viscosity and compressibility of a fluid, the Nusselt number depends only on the Rayleigh number (Jeanloz and Morris, 1986).

Adiabatic geotherm

The above discussion on the heat transport mechanisms allows to make inferences on the geotherm of the mantle. The geotherm through the interior of a convecting region follows an adiabat if the following two assumptions are satisfied: (1) There are no entropy sources in the fluid and (2) any intial entropy variations have had time to decay. The large Peclet number of the mantle ensures that the first assumption is satisfied, although presence of the radioactive elements causes slight deviation from adiabadicity. The time scale for reaching the steady state has been estimated numerically for a single-layer incompressible convection. Adjusting this time scale for a compressible fluid infers that the second assumption is satisfied for a single-layer flow. For a two-layer flow, however, the initial entropy variations may still cause deviations from adiabadicity. The adiabatic geotherm of the mantle is also supported by seismological observations (Jeanloz and Morris, 1986).

1.3 Whole-Mantle Convection

Whether the compositional discontinuity in the mantle at 660 km depth completely prohibits convective motions across the transition zone, causing stratification into separate upper and lower convecting systems, remains under debate. In this study we assume that there is no stratification of the mantle flow, a case that is referred to as the whole-mantle convection. In this section we present arguments that justify this assumption.
The whole-mantle convection is characterized by the possibility for plumes forming at the CMB to ascend all the way to the Earth's surface, as well as for slabs of former oceanic lithosphere to subduct all the way down to the base of the mantle. Consequently, whole-mantle convection implies that processes taking place in the lower mantle have some form of manifestations at the Earth's surface. Large igneous provinces (LIPs) and hotspot volcanos, which eruption sites are correlated with the seismic structures at the CMB (Torsvik et al., 2006), are possible examples of such manifestations. The continuity of negative seismic anomalies, assumed to be denser and colder subducting slabs, from the surface to the CMB is also suggestive of the mantle wide flow (Van der Hilst et al.). Additionally, the dynamic topography predicted by the whole mantle flow model is in better agreement with the observations than the one predicted by the stratified flow model (Hager et al., 1985). In this section we elaborate on these observations by presenting results from other studies that support whole-mantle convection model. A detailed overview of alternative convection models may be found in (Puchkov, 2009).

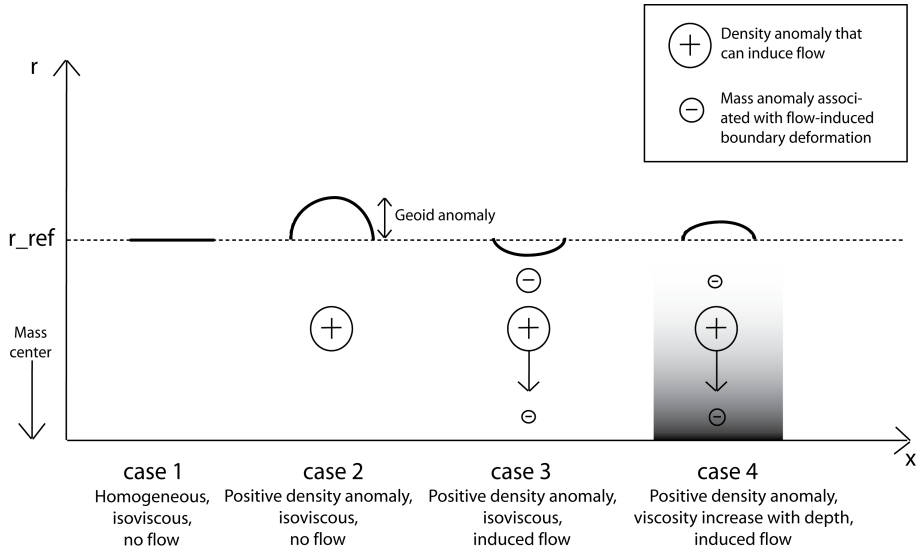

Figure 1.2: Plot of the altitude at which the gravity potential is measured for a viscous layer with different cases of mass anomalies. The dashed line represents the altitude of the reference geoid when no density anomalies are present. The solid line represents the altitude at which the measured potential has the value of the reference geoid. Positive and negative mass anomalies are marked with encircled + and − signs, respectively. Case 1: Homogeneous isoviscous layer that defines the altitude of the reference geoid. Case 2: Positive density anomaly in an isoviscous layer with no boundary deformation, resulting in a positive geoid anomaly. Case 3: Positive density anomaly in an isoviscous layer where the boundaries are allowed to deform, resulting in a negative geoid anomaly. The negative contribution to the geoid comes from the deformed top and bottom boundaries. Case 4: Positive density anomaly in a layer where the viscosity increases with depth and the boundaries are allowed to deform, resulting in a positive geoid anomaly.

1.3.1 Dynamic topography

Earth's geoid

An element of mass at the Earth's surface experiences gravitational attraction towards and centrifugal repulsion away from the Earth's center of mass. The combined effect of these forces is referred to as gravity. Thus, an element of mass at the Earth's surface is positioned in a gravity field and has a potential energy that is inversely related with its altitude above the center of mass. We define a gravity equipotential as a surface on which the value of the potential energy per unit mass is a constant. The geoid is an equipotential surface that defines the sea level (Turcotte and Schubert, 2002).
Consider an idealized model of the Earth with a homogeneous density distribution in its interior. We can derive an expression for the distance from the mass center of this model,

the altitude r_{ref}, at which the potential value is equal to some reference value, for example the geoid. The difference between r_{ref} and the altitude at which the measured potential is equal to the reference potential is called the geoid anomaly (Turcotte and Schubert, 2002).

Geoid anomalies in a convecting layer

Convective flow in the mantle gives rise to geoid anomalies. Presence of internal density contrasts and the deformation of the boundaries due to the flow induced by these density contrasts contribute to the measured geoid (Hager, 1984). Let us consider a case with a high density anomaly introduced in the interior of an isoviscous layer, before it induces any flow. This is illustrated in case 2 in Figure 1.2. The altitude at which the measured potential is equal to the geoid is higher with the density anomaly present, case 2, than without it, case 1. Hence, a positive density contrast results in a positive geoid anomaly.
Now let us consider the effect of deforming boundaries in this isoviscous layer. The sinking positive density anomaly pulls the material behind it and pushes the material in front of it. This results in a downward deflection of the boundaries, which changes with time until a steady state is achieved. We only consider the configurations of boundary deformations after the steady state has been reached. It is an appropriate approximation when applying this model to the mantle, since the steady state is reached over time scales of the postglacial rebound. These are essentially instanteneous compared to the time scales of subduction (Hager, 1984). The contribution to the total geoid anomaly is stronger from the deflection of the top boundary, because it is positioned at a higher altitude, although the magnitude of deflections at top and bottom is the same. Downward boundary deformation gives a negative change in the altitude at which the measured geoid is equal to the reference geoid. This is illustrated in case 3 in Figure 1.2. Hence, the total geoid anomaly is negative for a positive density contrast when the boundaries are allowed to deform (Hager, 1984).
We increase the complexity of the problem further by allowing the viscosity to increase with depth. The sinking rate of the positive density anomaly is slower in this case than in case 3, resulting in a larger deflection of the bottom than of the top boundary. As was discussed earlier, deformation at higher altitude has most effect on the geoid. Hence, the total negative contribution to the geoid anomaly is smaller in this case than in case 3. The situation is illustrated in case 4 in Figure 1.2. The total geoid anomaly is positive for a positive density contrast in a layer where the boundaries are allowed to deform and the viscosity increases with depth (Hager, 1984).

Depth-dependent viscosity and whole-mantle convection

The magnitude of the geoid anomaly that arises due to convective flow in the mantle depends on the spatial distribution of the effective viscosity and the depth of the convecting region (Hager, 1984). The latter is directly related to whether or not the mantle is chemically stratified, with a discontinuity at ca 660 km depth acting as a barrier to convection

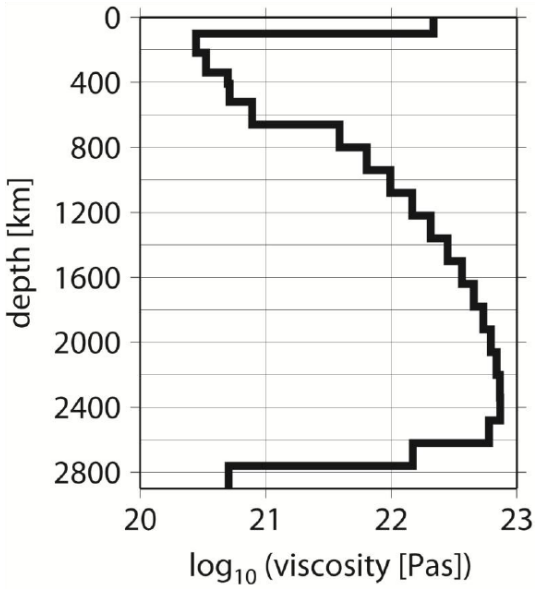

Figure 1.3: Radial viscosity staructure constrained by models of the geoid and the results from mineral physics (Steinberger and Calderwood, 2006)

(Hager, 1984). Estimating the positive density anomalies in the mantle associated with subducted slabs, the geoid anomalies can be predicted for different models of the mantle. Comparing the predicted geoid with the one observed can place a constraint on the viscosity distribution in the mantle (Hager, 1984). The observed correlation of the geoid highs with the high density subducted slabs infers that the viscosity of the mantle increases with depth. A viscosity ratio of at least a factor of 30 is required for a mantle that is assumed to be a Newtonian, radially symmetrical fluid (Hager, 1984). Comparing the magnitudes of the observed and predicted geoid anomalies suggests whole mantle convection (Hager, 1984).
Using the constraints from the modelled geoid, together with the results from mineral physics, a model of the radial viscosity structure is obtained by (Steinberger and Calderwood, 2006) and presented in Figure 1.3.

1.3.2 Deep Subduction

One of the alternatives to the whole mantle convection model that has been proposed is a layered convection model. The layered model permits no material transport across the upper mantle transition zone at 660km discontinuity into the lower mantle. Tomography reveals three features that, in combination, strongly support the possibility of such material transport (Van der Hilst et al.). First, there is a continuity between the long narrow structures of higher than average seismic velocities in the lower mantle to the slabs in the

upper mantle. Second, there is a strong correlation between the geographical distribution of these high velocity structures with locations at the surface of plate convergent margins in the past 120 Ma. Finally, there is a continuation of some of these narrow downwellings all the way to the base of the mantle, where they spread out to form a long wavelength structure. Whole-mantle flow with substantial flux across the upper mantle transition zone into the lower mantle provides a good explanation for these seismological observations. Additionally, the time scale for dynamic processes is significantly longer in the lower mantle, due to its high viscosity, compared to the upper mantle. Consequently, the strong correlation between locations of high seismic velocity anomalies in the upper and lower mantle is hard to explain by separate flow regimes coupled by heat exchange alone, in favor of the whole-mantle convection model (Van der Hilst et al.).

1.3.3 Deep Mantle Plumes

Whether the material that produced large igneous provinces (LIPs) and hotspots stems from a deep or shallow source remains a disputed subject (Sleep, 2006). Correlation of the geographical distribution of their eruption sites with tomographically resolved structures at the base of the mantle seems to infer a deep mantle source (Torsvik et al., 2006). Using four different restoration methods, involving paleomagnetic as well as fixed and moving reference frames, current locations of LIPs as old as 200Ma were rotated back to their eruption sites (Torsvik et al., 2006). This lead to the observation that 90% of the eruption sites project radially downwards to the margins of the two large low shear velocity provinces (LLSVPs) close to the CMB, which were resolved by seismic tomography. The same is true for most hotspots of arguably deep origin. Results of this study are illustrated in Figure 1.4. These observations support the evidence that LIPs and hotspots are generated by plumes originating at the CMB and therefor also the idea of a whole-mantle flow regime.

1.4 Structure of the lowermost mantle

Despite the whole-mantle flow regime, the planform of convection appears to be significantly distorted in two depth intervals: $500-800$km depth and $1800-2300$km depth (Van der Hilst et al.). We choose to focus on the behavior of the mantle structures that may be causing the deepest distortion and do not discuss the influence that the transition zone has on the mantle flow. An overview over ideas concerning reorganization of the mantle flow across the transition zone may be found in (Dziewonski et al., 2010). Constraints on the CMB region proposed by seismology, experimental mineral physics and numerical calculations are presented in the following sections.

1.4.1 D" region

Pioneering studies of the Earths density variations, divided the Earth's spherical shells into regions named A to G (Bullen, 1940). The layer between 984 km depth and the CMB

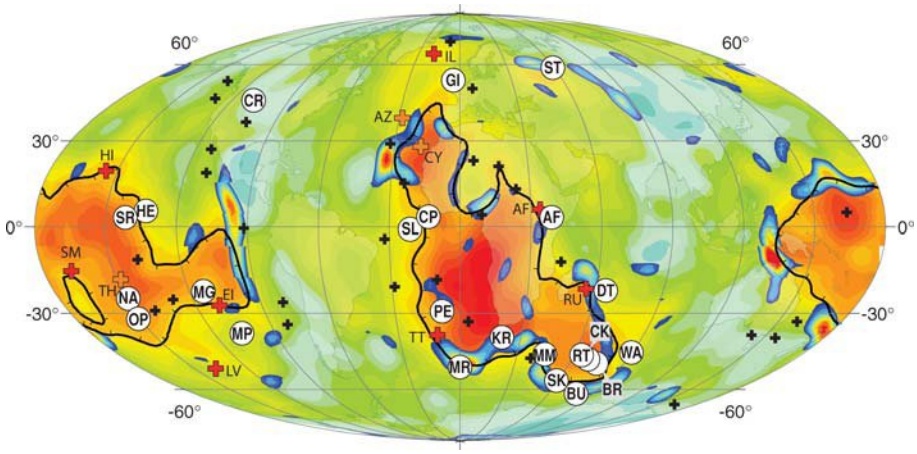

Figure 1.4: Original LIP eruption sites and hotspots (crosses) on the SMEAN shear wave velocity anomaly model for 2800 km. There is a strong tendency for LIP and hotspot eruption sites to overlie the high horizontal gradients in seismic velocity peripheral to the 'Africa' and 'Pacific' low-velocity regions (red) (Torsvik et al., 2006).

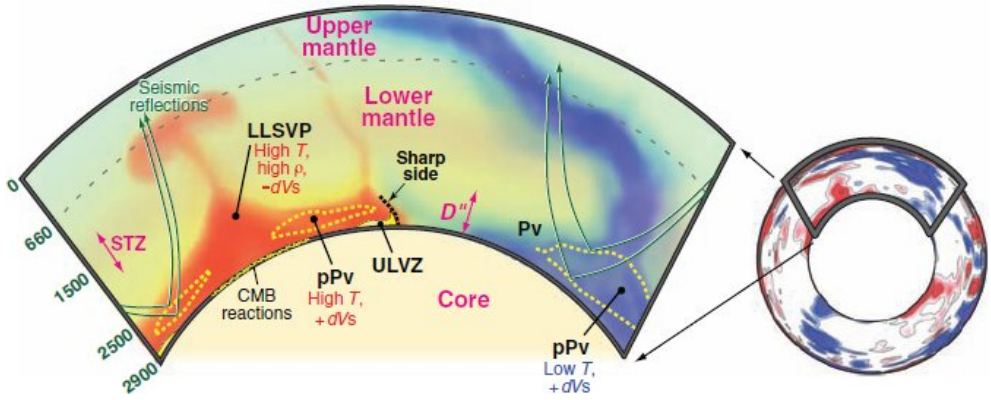

Figure 1.5: Tomographically derived high and low seismic shear velocity variations in Earth's mantle (blue and red, respectively) are shown in an equatorial cross section (right) viewed from the south, along with an enlarged panel (left) depicting several seismic findings in the D" region (Garnero and McNamara, 2008).

was named D and corresponded to the lower mantle. As seismic studies revealed more details about the structure of the lower mantle, and specifically the velocity discontinuity in the lowermost mantle, it became convenient to further divide the D-layer. In the recent literature, most of the lower mantle is referred to as D', while D" represents the deepest 250-300 km of the mantle.

1.4.2 Level of heterogeneity in the lowermost mantle

One of the characteristics of the D" layer is that it is much more anomalous than the rest of the lower mantle (Garnero and McNamara, 2008). Some of the features are illustrated in Figure 1.5. Sharp increase in the amplitude of the lateral heterogeneity has been revealed by tomography models for both fast- and slow-velocity regions, dominated by degrees 2 and 3 large-scale heterogeneity (Liu et al., 1998). This large-scale heterogeneity is associated with the Large Low Shear Velocity Provinces (LLSVPs) (Dziewonski et al., 2010) and will be discussed in more detail in the following sections.

1.4.3 Heterogeneities of non-thermal origin

Another characteristic of the D" layer is the significant decrease in the gradients of both P- and S-wave velocities with depth into that region, some places even becoming negative. This is a persisten result from many seismological studies. Using signals reflected or scattered from internal structures, an approach that has the advantage in locating rapid changes in seismic wave speed, a radial discontinuity in shear-velocity was found. The discontinuity is of the order $2-3\%$ and is located $200-300$ km above the CMB in various parts of the world (Liu et al., 1998). This discontinuity was confirmed by other studies to be present in both high- and low-velocity regions of the lower mantle, with geographical variation of the depth and velocity change across it (Garnero and McNamara, 2008).
The observed reduction in seismic velocity gradient with depth was initially iterpreted as being caused by the rapid temperature increase within the lowermost-mantle thermal boundary layer. However, the observed lateral heterogeneities are of much higher amplitude that what could be expected if they were of purely thermal origin (Garnero and McNamara, 2008). Therefore, the question arises of whether the D" region is a separate layer from the overlying lower mantle (Loper and Lay, 1995). We present some of the evidence that support the existence of non-thermal variations.
If both P- and S- velocity variations were linearly related to variations in temperature, they should be perfectly correlated. Similarly, if density models determined using normal modes and S-wave tomography were only temperature-dependent, they should also be positively correlated. However, an anti-correlation is observed in both cases (Steinberger and Holme, 2008). In addition, it is speculated that the abruptness of observed velocity increases over no more than a few tens of kilometers requires a chemical contrast or a phase transition (Loper and Lay, 1995).

The origin of the anomalies in the lowermost mantle remains a disputed subject and poses a limit for the validity of the physical models. Composition of the D" layer is crucial to constrain the CMB topography that is predicted as part of the mantle flow computation in the geodynamic models (Dziewonski et al., 2010).

1.4.4 Insights from mineral physics

Further insight into what constitutes the D" layer in particular, and the lower mantle in general, has been gained from mineral physics studies. Although there is still a large range of acceptable models for the lower mantle composition, equation-of state measurements indicate that silicate perovskite ($(Mg, Fe)SiO_3$) is the predominant mineral of that region (Loper and Lay, 1995). The experiments performed using a laser-heated diamond anvil cell revealed that the synthesis conditions for the perovskites (silicate perovskite and coexisting melts) are representative of those in the lower mantle: pressures of > 50 GPa and temperatures of $2000 - 4500$ K (Knittle, 1998). In the same study it was found that upon melting of silicate perovskite, the melting point of which remains uncertain, iron partitioning takes place with the effect of producing a melt which is $1 - 3\%$ denser than its coexisting solid. Occurence of these negatively buoyant melts anywhere in the deep mantle would result in them draining down to the CMB region and could potentially explain some of the heterogeneities of the D" layer, for example the seismically detected ultra-low velocity zones (Knittle, 1998).
Another mechanism that could create dense melts at the CMB, indicated by mineral physics, is the chemical reactions between the silicate perovskite and the molten iron, assuming a flux of the latter from the core into the mantle (Loper and Lay, 1995). To estimate the quantity of partial melts in the hot regions of the D", it is critical to know the melting point of silicate perovskites. The latter could also provide an upper bound on the temperature at the CMB, as well as the viscosity structure of the mantle, which would have a major impact on physical models of the mantle. But, as already mentioned, the melting point is still uncertain and ranges from less than 5000 to 8500 K (Loper and Lay, 1995). This temperature range is comparable to the temperature estimates of the core side of the CMB - 4000 K and temperature just above the D" - 2500 K (Torsvik et al., 2006).
Experiments also revealed that presence of water strongly influences the perovskite-iron reactions (Loper and Lay, 1995), as well as properties of the silicate mantle such as its viscosity and melting temperature (Murakami et al., 2002). However, the possible sites for water in lower mantle minerals have been controversial. An experimental study has shown that Mg-perovskite and magnesiowstite, both of which are present in the lower mantle, contain about 0.2 weight percent water at a pressure of 25.5 GPa and at temperatures between about $1850 - 1900$ K (Murakami et al., 2002).
Mineral physics research provides an additional argument for non-thermal heterogeneities within the D" layer. The seismic anomalies near the CMB are mapped into thermal variations using estimates of the seismic velocity of minerals, and their thermal expansion coefficient as function of composition, pressure and temperature. The inferred temperature

variations exceed 1200 K, which is argued to be implausible and requires presence of chemical heterogeneity in the region (Loper and Lay, 1995).
Recent experimental production of a post-perovskite phase transition in magnesium silicate ($MgSiO3$) has suggested that it is likely to occur $200 - 300$ km above the CMB. The post-perovskite transition may explain the seismically observed discontinuty at that depth. A large positive Clapeyron slope was obtained for the phase change, both from experiments and calculations, which could explain why the D" discontinuity is mainly observed in the regions of higher than average shear wave velocities. More explicitly, faster regions have been suggested to be colder and hence lower pressures are required to reach phase-change conditions, compared to higher temperature regions (Torsvik et al., 2006).
The last argument for non-thermal temperature variations in the D" layer that we present here, is based on the estimated temperatures of the plume material ascends. Using olivines to estimate differences in mantle potential temperature of Iceland and Hawaii, it has been indicated that at least the plumes underlying these locations are approximately 200 K hotter than normal mantle (Sleep, 2006). This rather low excess temperature, compared with the implied temperature drop across D" of > 1000 K, is easiest to explain by plumes rising from the top of a chemically distinct layer at the base of the mantle (Torsvik et al., 2006). A more complete overview of studies that favour the idea of D" zone having a chemically distinct composition can be found in (Torsvik et al., 2006).

1.4.5 Large Low Shear Velocity Provinces

Based on the interpretation of the travel time anomalies, a method that has the advantage of recovering large scale structure, it has been inferred that the seismic velocity anomaly in the lowermost mantle is dominated by the degrees 2 and 3 spherical harmonics (Liu et al., 1998). This signal is characterized by two antipodal regions of lower than average seismic velocities. A study that synthesises results from the seismic constraints and considerations of the non-hydrostatic moment of inertia tensor infers that this giant degree 2 anomaly is long-lived and imposes control on mantle circulation (Dziewonski et al., 2010).
This large-scale structure, which begins at about 2000 km depth and increases to the CMB, is associated with the two low velocity regions, the so-called African and Pacific Large Low Shear Velocity Provinces (LLSVPs) (Dziewonski et al., 2010). The height of the LLSVPs is estimated to be about 1000 km for the African anomaly and at least 500 km for the Pacific anomaly, where the latter is less certain. The LLSVPs appear to cover nearly 50% of the CMB, both extending about $15,000$ km across (Garnero and McNamara, 2008). Seismic waves reveal that the boundaries between the LLSVPs and surrounding mantle are sharp, with an outward tilt of the edge observed for the African anomaly (Ni et al., 2002).
The negative correlation between the bulk sound velocity and the shear velocity within the LLSVPs suggests that the anomalies are of chemical origin (Ni et al., 2002). This hypothesis is also supported by a study that used normal-mode data to resolve density heterogeneity within the mantle, and indicated an increased density in the location of superplumes (Ishii and Tromp, 2004). The sharp and steeply dipping edges of the African LLSVP are also

best explained as compositionally controlled (Torsvik et al., 2006).
The fact that the seismic shear velocities are lower than average in the LLSVPs suggests that these are hotter than the surrounding mantle. The correlation with the restored eruption sites of hotspots and Large Igneous Provinces (Torsvik et al., 2006), as well as the anti-correlation with regions of long term subduction, supports the evidence for higher than average temperature in LLSVPs(Tan and Gurnis, 2005).
The observed correlation between the restored LIPs and hotspots eruption sites of the past 200 Ma and the margins of the LLSVPs suggests that the latter have occupied their current positions for at least that long (Torsvik et al., 2006).

1.4.6 Previous numerical modeling by other authors

Chemical origin of the LLSVPs

Geodynamic models propose different scenarios for how the LLSVPs are formed and maintained. One of these involves mantle convection that sweeps a chemically distinct and intrinsically denser material in the mantle toward the upwelling regions, creating piles which shapes resemble the LLSVPs. The origin of chemical heterogeneity is suggested to be the accumulated subducted crust, or, alternatively, a primordial layer that have existed since the Earth's early differentiation (Garnero and McNamara, 2008). The former has been shown to satisfy seismological, geodynamical, mineralogical and geochemical constraints (Tan and Gurnis, 2005).
Formation of the thermochemical piles that satisfy the geometrical constraints inferred from seismological observations has been studied in (McNamara and Zhong, 2005). The geometrical constraints include a sharp-edged linear, ridge-like morphology for the African anomaly and a more rounded pile-shape for the Pacific anomaly. The model used in their study incorporates an initial layer of dense material at the base of the mantle, which is swept into ridges in the course of simulation. The thickness of the layer determines the areal extent and the height of the resulting thermochemical piles. The study emphasises the importance of a depth- and temperature-dependent rheology of the mantle model together with a realistic plate history as surface boundary conditions. Results of the simulations with an isochemical model of the mantle are shown to be inconsistent with observational constraints, such as tomography maps.
Results of the numerical modeling of mantle flow in the study of (Steinberger and Holme, 2008) revealed the importance of considering the non-thermal density variations. The results of their simulations satisfied the constraints posed by the long-wavelength geoid, heat flux profile, average viscosity based on the postglacial rebound and the CMB topography.
The study of (Ni et al., 2002) supports the evidence that the superplumes are of chemical origin, based on the results of thermal convection modeling with presence of a dense basal layer. Their conclusion is derived from the geodynamic models that succeed in reproducing the seismically observed sharp interfaces and shapes of the superplumes.

Stability of the LLSVPs

The longevity and gravitational stability of the LLSVPs are achieved if their thermal and compositional buoyancies are roughly balanced (Garnero and McNamara, 2008). Geodynamic models suggest that an intrinsic density elevation of a few percent for the material constituting the heterogeneity, with respect to the surrounding mantle, is required to satisfy this constraint. If the percent value of density elevation is too high, the structures flatten out, while a too low value results in excessive entrainment into upwellings (Garnero and McNamara, 2008).
The compositional viscosity difference between the dense basal layer and the ambient material has an effect on the entrainment rate when exposed to convection. Experimental studies suggest that a significantly lower viscosity of the basal layer counteracts the mixing with the ambient material (Beuchert et al., 2010). Numerical studies, however, provide evidence that the opposite is the case (Beuchert et al., 2010).
Gravitational stability of the superplumes has been investigated in (Tan and Gurnis, 2005), using a compressible thermochemical convection model. The density contrast between chemically distinct materials in their model is expressed as a sum of contributions from the thermal and chemical variations. The authors suggest that a chemically distinct material with a thermal expansion coefficient that decreases with depth has an effect of increasing the total density contrast with depth. Structures with high topography and steep sides are unlikely to form in this case. A compositional density difference that decreases with depth, on the other hand, can lead to formation of metastable superplumes with high topography. The compositional density difference between the materials depends on their shear bulk moduli, different values of which are investigated. The study of (Tan and Gurnis, 2005) reveals a specific range of values of bulk modulus and density contrast for which a single plume with steep sides is formed at the base of the thermochemical model. Values outside this range result in either too much entrainment, or a layer at the base that is too heavy to be swept into a pile.
Geodynamic models show that the thermomechanical piles move laterally along the base (Beuchert et al., 2010). Hence, the stability of the equatorial, antipodal positions of the LLSVPs, suggested in (Torsvik et al., 2006), requires investigation. The centrifugal forces have been suggested to have an effect of moving the LLSVPs towards the equator (Beuchert et al., 2010). The study of this effect was not conclusive, however, and further investigation is required.

Chapter 2

Equations Governing Mantle Convection

2.1 Governing equations

We assume that the mantle deforms as a fluid on geological timescales. Further, we assume that the mantle is a fluid continuum, since the lengthscales of changes in its properties, such as velocity, are presumably very large compared to its atomic or molecular scale (Schubert et al., 2001). This enables us to apply the continuum partial differential equations to compute mantle flow. The equations are simplified assuming that the mantle is an infinite Prandtl number fluid with simple Newtonian rheology and that the Boussinesq approximation applies. The validity of these approximations is discussed.

2.1.1 Conservation of mass

We first consider the law of mass conservation, known as the continuity equation. It states that the time rate of change of the mass of a material region is zero. The mass of a material region is given by the integral over its density, resulting in following formulation of mass-conservation:

$$\frac{d}{dt}\int_{V(t)} \rho dV = 0 \tag{2.1}$$

The time rate can be evaluated inside the integral using Leibnitz's theorem. Using Gauss's theorem, all terms can be combined into a single volume integral. At last, the restriction to a material region may be eliminated, since the resulting expression applies at every point (Panton, 1996). At the end of the day, we stand with the following relation:

$$\frac{\partial \rho}{\partial t} + \nabla \cdot (\rho \vec{v}) = 0 \tag{2.2}$$

This is the Eulerian formulation of the continuity equation, meaning that it is written for a fixed observation point P. Each term of the Equation 2.2 is interpreted as following: $\frac{\partial \rho}{\partial t}$ is the rate of accumulation of mass per unit volume at P and $\nabla \cdot (\rho \vec{v})$ is the net flow of mass out of P per unit volume.
For a moving point of reference, the Lagrangian formulation is used (Gerya, 2010):

$$\frac{D\rho}{Dt} + \rho \nabla \cdot \vec{v} = 0 \tag{2.3}$$

where the substantial derivative, which allows to evaluate the time derivative as we follow a material particle, was introduced:

$$\frac{D}{Dt} = \frac{\partial}{\partial t} + \vec{v} \cdot \nabla \tag{2.4}$$

Each term of the Equation 2.3 is interpreted as following: $\frac{D\rho}{Dt}$ is the rate of change of the density of a fluid particle, ρ is the mass per unit volume and $\nabla \cdot \vec{v}$ is the particle volume expansion rate. An incompressible flow implies that the density of the fluid doesn't change, reducing the continuity equation to the following form:

$$\nabla \cdot \vec{v} = 0 \tag{2.5}$$

2.1.2 Conservation of momentum

Next, we consider the law of momentum conservation, which for a fluid continuum is the analogue of Newton's second law for a point mass (Panton, 1996). The momentum equation states that any imbalance of forces on an elemental fluid parcel will cause it to accelerate (Schubert et al., 2001). We express the acceleration term as the time rate of change of the linear momentum. Momentum within a material region is given by a volume integral of the product of density and velocity. The momentum-conservation may thus be expressed as following:

$$\frac{d}{dt} \int_{V(t)} \rho \vec{v} dV = \text{net force on the material region} \tag{2.6}$$

Two types of forces that act on the elemental parcel need to be considered: surface forces acting on its boundary surfaces and volume forces acting throughout its volume, denoted $\vec{R}$ and $\vec{F}$, respectively. Using Leibnitz's and Gauss's theorems, like for the continuity equation above, the Eulerian formulation of the momentum equation can be expressed as following (Panton, 1996):

$$\frac{\partial}{\partial t}(\rho \vec{v}) + \nabla \cdot (\rho \vec{v} \vec{v}) = \vec{F} + \vec{R} \tag{2.7}$$

The Lagrangian formulations is as following:

$$\rho \frac{D\vec{v}}{Dt} = \vec{F} + \vec{R} \tag{2.8}$$

Surface forces, Volume forces

The surface forces are proportional to the extent of the area on which they act. The surface force per unit area depends on the position P in which it is evaluated and the orientation of the surface that passes through P. Defining this surface by an outward normal vector $\vec{n}$, the stress acting on this surface is given by the product of the normal vector and the stress tensor evaluated at point P (Panton, 1996). The stress tensor is required to be symmetric by the torque balance (Schubert et al., 2001). The net surface forces are decomposed into those that act independent of whether there is flow or not, the thermodynamic pressure p, and those that arise when there is flow, the deviatoric stresses $\vec{\tau}$.
The volume forces are proportional to the volume of fluid on which they act and are expressed in terms of a force per unit volume, $\vec{f}$. Inserting for the surface and volume forces, we arrive at the following expression for the momentum conservation:

$$\rho \frac{D\vec{v}}{Dt} = -\nabla p + \nabla \cdot \vec{\tau} + \rho \vec{f} \tag{2.9}$$

Each term of the Equation 2.9 for a fixed point P is interpreted as following: $\frac{\partial}{\partial t}(\rho\vec{v})$ is the rate of momentum increase, $\nabla \cdot (\rho\vec{v}\vec{v})$ is the net rate at which momentum is carried into P by fluid flow $\rho\vec{v}$, ∇p is the net pressure force, $\nabla \cdot \vec{\tau}$ is the net viscous force and $\rho\vec{f}$ is the net body force (Panton, 1996).

Constitutive equation - Newtonian rheology

To apply the expression of momentum conservation to our problem, a constitutive equation must be introduced. The constitutive equation relates the stress and deformation in a fluid continuum (Kundu, 2008), and is also known as the rheological law for the fuid (Turcotte and Schubert, 2002). The deviatoric stress tensor mentioned earlier is related to the velocity gradient tensor. Only the symmetric part of the velocity gradient tensor, known as the strain rate tensor e_{ij}, can generate stresses and is given by:

$$e_{ij} \equiv \frac{1}{2}\left(\frac{\partial v_i}{\partial x_j} + \frac{\partial v_j}{\partial x_i}\right), \tag{2.10}$$

where the Einstein summation convention is adopted. We will assume that the mantle is a Newtonian fluid. This means that the components of its strain rate tensor are linearly related to its stress components (Turcotte and Schubert, 2002). For an isotropic fluid, two constants of proportionality need to be considered: the viscosity μ associated with the rates of shear deformation, and the second viscosity λ associated with the volume expansion rate (Turcotte and Schubert, 2002). The deviatoric stress tensor can be expressed as:

$$\tau_{ij} = 2\mu e_{ij} + \lambda e_{mm}\delta_{ij} \tag{2.11}$$

where the Kronecjer delta tensor was introduced.
The normal stresses acting on a fluid parcel combine the thermodynamic pressure and the

normal components of the viscous stresses that arise due to motion of the fluid. We define the mechanical pressure to be the average of the normal components of the viscous stresses. The difference between the mechanical and thermodynamic pressures, denoted as p_m and p_t, respectively, is given by:

$$p_t - p_m = (\frac{2}{3}\mu + \lambda)\nabla \cdot \vec{v} \tag{2.12}$$

where we replaced the notation e_{mm} to $\nabla \cdot \vec{v}$ for the volume expansion rate. The term $\frac{2}{3}\mu + \lambda$ is known as the coefficient of bulk viscosity, k_B, and has a very small value for many fluids (Schubert et al., 2001). Using $k_B = 0$ is known as the Stokes assumption. Inserting $k_B = 0$ into Equation 2.12 results in $p_t = p_m$. Hence, with the Stokes assumption there's no need to distinguish between the thermodynamic and the mechanical pressure. From now on, the pressure term in the momentum equation will refer to the mechanical pressure.
Applying the incompressibility constraint $\nabla \cdot \vec{v}$ to Equation 2.11 and expressing the strain rate tensor in terms of the velocity gradients, we obtain the constitutive equation for an incompressible Newtonian fluid:

$$\tau_{ij} = \mu(\frac{\partial v_i}{\partial x_j} + \frac{\partial v_j}{\partial x_i}) \tag{2.13}$$

Stokes equation

The conservation of momentum can be expressed for a Newtonian fluid by inserting the rheological law in Equation 2.13 into Equation 2.9:

$$\rho\frac{Dv_i}{Dt} = -\frac{\partial p}{\partial x_i} + \frac{\partial}{\partial x_j}\Big[\mu(\frac{\partial v_i}{\partial x_j} + \frac{\partial v_j}{\partial x_i})\Big] + \rho g_i \tag{2.14}$$

where we have also assumed that gravity is the only body force acting on the fluid.

2.1.3 Conservation of energy

In this section, we discuss the conservation of thermal energy, which describes the balance of heat in a continuum and the related temperature changes (Gerya, 2010). The second law of thermodynamics relates the heat added to the system, dq, and the related change in specific entropy, ds, as following:

$$dq = Tds \tag{2.15}$$

Hence, the entropy of the system may change due to internal heat generation, viscous dissipation, as well as due to conductive and convective heat transport (Schubert et al., 2001). This is summarized in the following expression for the time rate of change of the specific entropy for a moving point of reference:

$$\rho T\frac{Ds}{Dt} = \frac{\partial}{\partial x_i}\Big(k\frac{\partial T}{\partial x_i}\Big) + \Phi + \rho H \tag{2.16}$$

where k is the thermal conductivity, Φ is the dissipation function and H is the rate of internal heat production per unit mass. Here it is assumed that Fourier's law of heat conduction for an isotropic medium applies:

$$q_i = -k\frac{\partial T}{\partial x_i} \tag{2.17}$$

where q_i is the heat flux vector. Using the thermodynamic quantities c_p, the specific heat at constant pressure, and α, the thermal expansivity, the thermal energy conservation may be expressed in terms of temperature and pressure, as following:

$$\rho c_p \frac{DT}{Dt} - \alpha T \frac{Dp}{Dt} = \frac{\partial}{\partial x_i}\left(k\frac{\partial T}{\partial x_i}\right) + \Phi + \rho H \tag{2.18}$$

2.2 Approximate equations

2.2.1 Linearization

Density changes in the mantle are mostly due to the hydrostatic compression, but also due to the temperature and pressure variations accompanying convection (Schubert et al., 2001). The latter are small compared to the spherically averaged density of the mantle. It is therefore justified to represent physical parameters in terms of a sum of a reference state value, denoted by an overbar, and perturbations from that reference state, denoted by the primes. The equation of state then takes the linearized form:

$$\begin{aligned}
\rho &= \bar{\rho}(\bar{T},\bar{p}) + \rho' = \bar{\rho}(\bar{T},\bar{p}) + \bar{\rho}\bar{\chi_T}p' - \bar{\rho}\bar{\alpha}T' \\
T &= \bar{T} + T' \\
p &= \bar{p} + p'
\end{aligned}$$

where we have assumed that the density is only a function of temperature and pressure. The thermodynamic variables χ_T, isothermal compressibility, and α, thermal expansivity, were introduced in the linearized equation of state.

2.2.2 Reference state

We choose the reference state to be steady and motionless. The form of Equation 2.14 that satisfies such conditions gives the hydrostatic reference state pressure:

$$\frac{\partial \bar{p}}{\partial x_i} = \bar{\rho}\bar{g}_i \tag{2.19}$$

Because we have a vigorously convecting system, as was described in the introductory chapter, we choose an adiabatic reference state temperature. We choose all other physical quantities of the reference state to be contants.

2.2.3 Nondimensionalization

The following representative values, denoted by subscript r, are used for nondimensionalizing the governing equations and the equation of state:

$$
\begin{aligned}
\rho_r &\equiv \text{representative density in a convecting state} \\
\triangle T_r &\equiv \text{characteristic temperature difference driving thermal convection} \\
H_r &\equiv \text{representative internal heating rate} \\
\chi_{T_r} &\equiv \text{representative isothermal compressibility} \\
\alpha_r &\equiv \text{representative thermal expansivity} \\
\mu_r &\equiv \text{representative viscosity} \\
k_r &\equiv \text{representative conductivity} \\
c_{p_r} &\equiv \text{representative specific heat} \\
\kappa_r &= \frac{k_r}{\rho_r c_{p_r}} \equiv \text{representative thermal diffusivity} \\
\nu_r &= \frac{\mu_r}{\rho_r} \equiv \text{representative kinematic viscosity, or momentum diffusivity} \\
b &\equiv \text{depth of the convecting region} \\
\gamma_r &= \frac{\alpha_r}{\rho_r c_{v_r} \chi_{T_r}} \equiv \text{representative Gruneisen ratio} \\
u_r &= \frac{k_r}{\rho_r c_{p_r} b} \equiv \text{representative velocity} \\
p_r &= \frac{\mu_r u_r}{b} = \frac{\mu_r k_r}{\rho_r c_{p_r} b^2} \equiv \text{representative pressure}
\end{aligned}
$$

where in the last relation we have assumed that the pressure and viscous forces are comparable (Schubert et al., 2001). Using these scaling factors, we introduce the following

dimensionless variables, denoted with an asterisk:

$$
\begin{aligned}
T'^* &= \frac{T'}{\triangle T_r} \\
\rho^* &= \frac{\rho}{\rho_r} \\
p'^* &= \frac{p' b^2 \rho_r c_{p_r}}{\mu_r k_r} \\
u_i^* &= \frac{u_i b \rho_r c_{p_r}}{k_r} \\
x_i^* &= \frac{u_i}{b} \\
t^* &= \frac{t k_r}{b^2 \rho_r c_{p_r}} \\
\bar{\chi}_T^* &= \frac{\bar{\chi}_T}{\chi_{T_r}} \\
\bar{\alpha}^* &= \frac{\bar{\alpha}}{\alpha_r}
\end{aligned}
$$

Using these dimensionless variables, the linearized equation of state may be expressed as following:

$$\frac{\rho^*}{\bar{\rho^*}} = 1 + \bar{\chi}_T^* p'^* M^2 Pr - \bar{\alpha}^* T'^* \epsilon \tag{2.20}$$

where the following dimensionless parameters were introduced:

$$
\begin{aligned}
M^2 &\equiv \frac{k_r^2 \chi_{T_r}}{\rho_r c_{p_r}^2 b^2} - \text{measures influence of compressibility} \\
Pr &\equiv \frac{\nu_r}{\kappa_r} = \frac{\mu_r c_{p_r}}{k_r} - \text{ratio of momentum diffusivity to thermal diffusivity} \\
\epsilon &\equiv \alpha_r \triangle T_r - \text{fractional density change due to temperature} \\
&\qquad \text{variations driving convection}
\end{aligned}
$$

Inserting the values representative of the mantle, introduced in the introductory chapter, we obtain following values for the dimensionless parameters:

$$
\begin{aligned}
M^2 &\approx 10^{-33} \\
Pr &\approx 2.5 \cdot 10^{23} \\
\epsilon &\approx 3 \cdot 10^{-2}
\end{aligned}
$$

We will use the introduced dimensionless variables and the dimensionless form of the linearized equation of state to investigate the validity of the incompressible flow assumption for the mantle and to nondimensionalize the governing equations derived in the previous sections.

2.2.4 Incompressibility of the mantle

In this section we will discuss the validity of the incompressible flow assumption for the convecting mantle. The derivation closely follows (Schubert et al., 2001).
We can discuss the validity of the incompressibility constraint by considering the change in density with depth in an adiabatic (isentropic) model. First, we introduce the adiabatic compressibility - precentage increase in density per unit change in pressure at constant entropy (here shown for the reference state values, denoted by overbars):

$$\bar{\chi_a} \equiv -\frac{1}{\bar{v}}\Big(\frac{\partial \bar{v}}{\partial \bar{p}}\Big)_s = \frac{1}{\bar{\rho}}\Big(\frac{\partial \bar{\rho}}{\partial \bar{p}}\Big)_s \tag{2.21}$$

Another thermodynamic parameter we use is the Gruneisen ratio, which is a dimensionless parameter that describes the relative change in adiabatic temeprature with compression (Jeanloz and Morris, 1986), and is given by:

$$\bar{\gamma} \equiv \frac{\bar{\alpha}}{\bar{\rho}\bar{c_p}\bar{\chi_a}} \tag{2.22}$$

We also need the hydrostatic relation for pressure gradient, equivalent to the motionless and steady form of the Navier-Stokes equation, stated in Equation 2.14:

$$\frac{\partial \bar{p}}{\partial x_i} = \bar{\rho}\bar{g_i} \tag{2.23}$$

Using the chain rule to rewrite the derivatives, the gradient of the reference state density in an adiabatic model can be expressed as:

$$\frac{\partial \bar{\rho}}{\partial x_i} = \Big(\frac{\partial \bar{\rho}}{\partial \bar{p}}\Big)_s \frac{\partial \bar{p}}{\partial x_i} = \Big(\frac{\partial \bar{\rho}}{\partial \bar{p}}\Big)_s \bar{\rho}\bar{g_i} = \bar{\rho}^2 \bar{\chi_a}\bar{g_i} \tag{2.24}$$

We introduce a characteristic length scale, $\bar{h}_d$, for the increase of reference state density with depth:

$$\bar{h}_d \equiv \Big[\frac{1}{\bar{\rho}}\Big|\frac{\partial \bar{\rho}}{\partial x_i}\Big|\Big]^{-1} = (\bar{\rho}\bar{\chi_a}\bar{g_i})^{-1} = \frac{\bar{\gamma}\bar{c_p}}{\bar{\alpha}\bar{g_i}} \tag{2.25}$$

Incompressibility constraint implies that the density change across the mantle is small. This implies that the density scale height, $\bar{h}_d$, is large compared to the depth of the mantle,b. Hence, the following must hold:

$$\frac{b}{\bar{h}_d} = \frac{\alpha^* g_i^*}{\gamma^* c_p^*}\Big(\frac{\alpha_r g_{i_r} b}{\gamma_r c_{p_r}}\Big) \ll 1 \tag{2.26}$$

Which reduces to the following constraint, given that the dimensionless quantities are of order unity:

$$\frac{1}{\gamma_r}\frac{\alpha_r g_{i_r} b}{c_{p_r}} = \frac{D}{\gamma_r} \ll 1 \tag{2.27}$$

where we have introduced the dissipation number D. Inserting the values representative for the mantle, given in the introductory chapter, we obtain following:

$$\frac{D}{\gamma_r} \sim \frac{0.5}{1} = 0.5 \tag{2.28}$$

It may be concluded that the incompressible flow assumption is only approximately valid for the convective mantle flow. However, the influence of compressibility, measured by the dimensionless parameter M^2, is shown to be small for the mantle: $M^2 = 10^{-33}$. With these considerations in mind, we adopt the incompressible flow assumption due to the resulting simplicity of the governing equations.
The three requirements: $\epsilon \to 0$, $M^2 Pr \to 0$ and $D \to 0$ are known as the Boussinesq approximation and in this study we assume that it holds for mantle convection.

2.2.5 Dimensionless form of the Navier-Stokes equation

In this section, we introduce the dimensionless form of the Navier-Stokes equation in the Boussinesq approximation, and discuss the Rayleigh number, which is the dimensionless parameter that governs the vigor of convection.
Inserting the dimensionless variables, gradient of the reference state pressure and the dimensionless linearized equation of state into Equation 2.14, results in following expression:

$$\begin{aligned}\frac{1}{Pr}\Big[\bar{\rho}^* + \bar{\rho}^*\bar{\chi}_T^* p'^* M^2 Pr - \bar{\rho}^*\bar{\alpha}^* T'^* \epsilon\Big]\frac{Du_i^*}{Dt^*} = \\ -\frac{\partial p'^*}{\partial x_i^*} + \bar{g_i}^*\bar{\rho}^*\bar{\chi_T}^*\bar{p'}^*\frac{D}{\gamma_r}\frac{c_{p_r}}{c_{v_r}} - \bar{g_i}^*\bar{\rho}^*\bar{\alpha}^* T'^* Ra + \frac{\partial}{\partial x_j^*}\Big[\mu^*\Big(\frac{\partial u_i^*}{\partial x_j^*} + \frac{\partial u_j^*}{\partial x_i^*} - \frac{2}{3}\delta_{ij}\frac{\partial u_k^*}{\partial x_k^*}\Big)\Big]\end{aligned} \tag{2.29}$$

where it has been assumed that the variations in the gravitational acceleration due to convection are negligible. We have also introduced the dimensionless parameter Ra, which is the Rayleigh number given by:

$$Ra = \frac{g_r \rho_r^2 \alpha_r \triangle T_r b^3 c_{p_r}}{k_r \mu_r} = \frac{g_r \rho_r \alpha_r \triangle T_r b^3}{\kappa_r \mu_r} \tag{2.30}$$

The Rayleigh number is discussed in more detail later in this section. The Prandtl number, Pr, has been shown to have a large value for the mantle. It is therefore justified to approximate mantle as an infinite Prandtl number fluid and set the left side of the Equation 2.29 to zero. The consequence is that we neglect the inertial forces in the flow, which is known as the flow in Stokes regime, and the resulting equation is known as the Stokes equation. It has also been shown that assuming incompressible flow implies that $\frac{D}{\gamma_r} \to 0$ and that the continuity equation has the form $\frac{\partial u_k^*}{\partial x_k^*} = 0$. We assume that the dimensionless variables are of order unity and set them to $\bar{\rho}^* = \bar{\alpha}^* = 1$. The result is the Stokes equation in dimensionless form:

$$0 = -\frac{\partial p'^*}{\partial x_i^*} - \bar{g_i}^* T'^* Ra + \frac{\partial}{\partial x_j^*}\Big[\mu^*\Big(\frac{\partial u_i^*}{\partial x_j^*} + \frac{\partial u_j^*}{\partial x_i^*}\Big)\Big] \tag{2.31}$$

Rayleigh number

We illustrate how the Rayleigh number reflects the ratio of the efficiency of heat transport by conduction and convection by studying a problem in the regime that is just above marginal stability. It is shown that the timescales of the Rayleigh Taylor instability and thermal diffusion define the Rayleigh number in this regime. The derivation closely follows (Davies and Christensen, 2001).
Rayleigh-Taylor instability refers to a fluid of lower density that wants to rise through an overlying fluid of higher density. A buldge of height h and width w develops at the interface between the two fluids. The rise of the lighter fluid is represented by the increasing height of this buldge. The buoyancy forces drive this motion, while the viscous resistance opposes it.
Buoyancy force B arises due to gravity acting on density differences:

$$B = -gV\triangle\rho \tag{2.32}$$

where g is gravitational acceleration, V is volume and $\triangle\rho$ is the density difference. Viscous stresses σ, and hence the resisting force R, arise due to drag acting on the buldge as it flows through a viscous material:

$$\begin{aligned}\sigma &= \mu \cdot \text{representative velocity gradient}\\ R &= \sigma \cdot \text{length scale}\end{aligned}$$

where μ is the effective viscosity. We consider two extreme cases with the width of the buldge, w, much larger and much smaller than the depth of the two fluid layers, D. The representative velocity gradient is chosen appropriately for each case and the w is chosen to be the length scale for the resisting force. Equating the buoyancy and the resisting forces, as the system tries to reach balance, results in the time-dependent expression for the height of the buldge:

$$h = h_0\exp(t/\tau_{RT}) \tag{2.33}$$

where τ_{RT} is the time scale for the Rayleigh-Taylor instability. The time scale is found to have a minimum at $w = D$, given by:

$$\tau_{RT} = \frac{\mu}{g\triangle\rho D} \tag{2.34}$$

This implies that the perturbations at the interface between the two fluids that have width comparable to the layer depth will grow most quickly and come to dominate.
We will now consider density difference due to higher temperature:

$$\begin{aligned}\rho &= \rho_0[1-\alpha(T-T_0)] = \rho_0[1-\alpha\triangle T]\\ \triangle\rho &= \rho_0\alpha\triangle T\end{aligned}$$

where ρ_0 is the density at reference temperature T_0. Thermal diffusion tends to smear out the buldge that arises due to the density contrast. Hence, there is a competition between the buoyancy and the thermal diffusion. The timescale for thermal diffusion is given by:

$$\tau_\kappa = \frac{D^2}{\kappa} \tag{2.35}$$

and characterizes the time it would take for a fluid layer to cool significantly by conduction in the absence of convection. The competition may be characterized by the ratio of the timescales of these two processes, which is known as the Rayleigh number:

$$Ra = \frac{\tau_\kappa}{\tau_{RT}} = \frac{g\rho\alpha T D^3}{\kappa\mu} \tag{2.36}$$

The critical Rayleigh number defines the regime when the transition from pure conductive heat transport to onset of convection takes place. This value is usually of the order 1000. In the case of the mantle, the Rayleigh number is in the range between $10^5 - 10^9$, as was mentioned in the introductory chapter, implying vigorous convection.

2.2.6 Dimensionless form of the thermal energy conservation equation

In this section, we derive the expression for the adiabatic temperature profile, following (Turcotte and Schubert, 2002), and introduce the dimensionless form of the thermal energy conservation equation in the Boussinesq approximation, following (Schubert et al., 2001). In the introductory chapter we discussed that due to the vigorously convecting mantle, its geotherm is given by an adiabat, and hence the temperature increases isentropically with depth. The specific change in entropy is given by the following thermodynamic relation:

$$ds = \frac{c_p}{T} dT - \frac{\alpha}{\rho} dp \tag{2.37}$$

For an isentropic process $ds = 0$, and we obtain the following relation:

$$\left(\frac{dT}{dp}\right)_s = \frac{\alpha}{\rho c_p} T \tag{2.38}$$

We make use of the hydrostatic pressure gradient from Equation 2.19, that was assumed for the reference state pressure, to obtain the following result for the adiabatic geotherm:

$$\left(\frac{dT}{dx_i}\right)_s = \left(\frac{dT}{dp}\frac{dp}{dx_i}\right)_s = \frac{\alpha g_i}{c_p} T \tag{2.39}$$

where we have dropped the overbars for shortness. The dimensionless form of the Equation 2.39 is given by:

$$\frac{d\bar{T}^*}{dx_i^*} = \frac{\bar{\alpha}^* D \bar{g_i}^*}{\bar{c_p}^*} \bar{T}^* \tag{2.40}$$

Using the dimensionless expression for the geotherm and the fact that the reference temperature is time-independent, we obtain the following relation for the substantial temperature-derivative:

$$\bar{\rho}^* {\bar{c_p}}^* \frac{D\bar{T}^*}{Dt^*} = \bar{\rho}^* {\bar{c_p}}^* u_i^* \frac{d\bar{T}^*}{dx_i^*} = \bar{\rho}^* \bar{\alpha}^* D {\bar{g_i}}^* u_i^* \bar{T}^* \tag{2.41}$$

We can also use Equation 2.40 to derive an expression for heat conduction along the adiabat:

$$\frac{\partial}{\partial x_i^*}\Big(\bar{k}^* \frac{\partial \bar{T}^*}{\partial x_i^*}\Big) = \frac{\partial}{\partial x_i^*}\Big(\frac{\bar{k}^* \bar{\alpha}^* D {\bar{g_i}}^*}{{\bar{c_p}}^*} \bar{T}^*\Big) = \frac{\bar{k}^* \bar{\alpha}^{*2} D^2 {\bar{g_i}}^{*2}}{{\bar{c_p}}^{*2}} \bar{T}^* \tag{2.42}$$

where we assumed that $\bar{k}^*$, $\bar{\alpha}^*$, ${\bar{c_p}}^*$ and ${\bar{g_i}}^*$ are constants.
Inserting the dimensionless variables and the dimensionless linearized equation of state into the thermal energy conservation, given by Equation 2.18, results in following expression:

$$\begin{aligned}
&\Big[\bar{\rho}^* + \bar{\rho}^* \bar{\chi}_T^* p'^* M^2 Pr - \bar{\rho}^* \bar{\alpha}^* T'^* \epsilon\Big]({\bar{c_p}}^*) \frac{D}{Dt^*}(\bar{T}^* + T'^*) \\
&\quad - \bar{\alpha}^*(\bar{T}^* + T'^*) \frac{Dp'^*}{Dt^*} \frac{\epsilon D}{Ra} - \bar{\alpha}^*(\bar{T}^* + T'^*) {\bar{g_i}}^* u_i^* \bar{\rho}^* D \\
&\quad = \frac{\partial}{\partial x_i^*}\Big[\bar{k}^* \frac{\partial}{\partial x_i^*}(\bar{T}^* + T'^*)\Big] + \Phi^* \frac{D}{Ra} \\
&\quad + \Big[\bar{\rho}^* + \bar{\rho}^* \bar{\chi}_T^* p'^* M^2 Pr - \bar{\rho}^* \bar{\alpha}^* T'^* \epsilon\Big] H^* \Big(\frac{b^2 H_r \rho_r}{k_r \triangle T_r}\Big)
\end{aligned} \tag{2.43}$$

Using Equations 2.41 and 2.42 and the limits $M^2 Pr \to 0$, $\epsilon \to 0$, and $D \to 0$, as is adopted in the Boussinesq approximation, we arrive at the following dimensionless form of the thermal energy conservation equation:

$$\bar{\rho}^* {\bar{c_p}}^* \frac{DT'^*}{Dt^*} = \frac{\partial}{\partial x_i^*}\Big(\bar{k}^* \frac{\partial T'^*}{\partial x_i^*}\Big) + \bar{\rho}^* H^* \Big(\frac{b^2 H_r \rho_r}{k_r \triangle T_r}\Big) \tag{2.44}$$

It may be pointed out that one of the consequences of applying the limits of the Boussinesq approximation to the linearized energy conservation equation is that the viscous dissipation effects, represented by Φ, become neglected. Remembering that all the reference state quantities, except the temperature and pressure, are constants, we can express energy conservation as following:

$$\frac{DT'^*}{Dt^*} = \frac{\partial}{\partial x_i^*}\Big(\bar{\kappa}^* \frac{\partial T'^*}{\partial x_i^*}\Big) + \frac{H^*}{{\bar{c_p}}^*}\Big(\frac{b^2 H_r \rho_r}{k_r \triangle T_r}\Big) \tag{2.45}$$

2.3 Summary

In this section, we presented the the differential equations that govern mantle convection: the conservation laws of mass, momentum and thermal energy. We used linearized equations and introduced variables representative for the mantle to derive the approximate and

dimensionless forms of these equations. We assumed that the mantle is an infinite Prandtl number fluid with Newtonian rheology and that the Boussinesq approximation applies. The resulting dimensionless equations are presented below, where we have dropped the asterisk for shortness:

$$\begin{aligned} \frac{\partial u_i}{\partial x_i} &= 0 && \text{Mass conservation} \\ 0 = -\frac{\partial p'}{\partial x_i} - \bar{g}_i T' Ra + \frac{\partial}{\partial x_j}\Big[\mu\Big(\frac{\partial u_i}{\partial x_j} + \frac{\partial u_j}{\partial x_i}\Big)\Big] &&& \text{Momentum conservation} \\ \frac{DT'}{Dt} = \frac{\partial}{\partial x_i}\Big(\bar{\kappa}\frac{\partial T'}{\partial x_i}\Big) + \frac{H}{\bar{c_p}}\Big(\frac{b^2 H_r \rho_r}{k_r \triangle T_r}\Big) && \text{Energy conservation} \end{aligned} \tag{2.46}$$

Chapter 3

FEM Thermal Diffusion Solver

The conductive heat transport is modeled by solving the discretized equation of transient heat diffusion. In this section we present a Finite Element Method (FEM) code that is devised for solving this problem in two dimensions. The code is applied to model heat diffusion on a cylindrical geometry and is benchmarked against analytical solutions. The computational domain is partitioned using an unstructured mesh comprised of triangular or quadratic elements. We compare the accuracy of the solution obtained using four different element-types: first- and second-order triangles and quads.

3.1 Outline of the problem

The strong, or classical, formulation of heat diffusion without advection is given by the following partial differential equation:

$$\begin{aligned} \rho c_p \frac{\partial T}{\partial t} &= -(\frac{\partial}{\partial x} q_x + \frac{\partial}{\partial y} q_y) + \rho H, \quad (x, y) \in \Omega \\ q_x &= -(k \frac{\partial T}{\partial x}) \\ q_y &= -(k \frac{\partial T}{\partial y}) \end{aligned} \tag{3.1}$$

where T is temperature, ρ density, c_p heat capacity at constant pressure, H rate of internal heat production per unit mass, Ω the domain in which the problem is defined, k is the thermal conductivity, assuming that the system is isotropic, matrix that is assumed to be symmetric positive definite and q_x and q_y are thermal fluxes, expressed according to Fourier's law.
To complete the problem formulation, initial and boundary conditions must be specified. At the boundary, we either specify temperature values, known as the Dirichlet boundary

conditions, or the normal heat flux, known as the Neumann boundary conditions. We assume that the boundary conditions are not time-dependent and express them, together with the intial conditions, as following:

$$\begin{aligned} T(x,y) &= g, \quad (x,y) \in \Gamma_g \\ -(q_x n_x + q_y n_y) &= h, \quad (x,y) \in \Gamma_h \\ T(x,y,t=0) &= T_0(x,y) \end{aligned} \tag{3.2}$$

where Γ_g and Γ_h are the nonoverlapping Dirichlet and Neumann boundary segments, respectively, and n_x and n_y are components of the unit vector normal to the boundary.

3.2 Weak formulation

In FEM we use the weak formulation of the differential equations. To obtain the weak form of Equation 3.1, two classes of functions are introduced. The first collection of functions is called the *trial solutions* and consists of all functions that have square integrable derivatives, denoted H^1, and take on the value g at $(x,y) \in \Gamma_g$. Trial solutions space is expressed as following:

$$\mathcal{S} = \{s | s \in H^1, s((x,y) \in \Gamma_g) = g\} \tag{3.3}$$

The second collection of functions is called the *weighting functions*, or *variations*, and consists of all functions that have square integrable derivatives and take on the value 0 at $(x,y) \in \Gamma_g$. Variational space is expressed as following:

$$\mathcal{V} = \{w | w \in H^1, w((x,y) \in \Gamma_g) = 0\} \tag{3.4}$$

Multiplying Equation 3.1 with a function w from variational space and integrating it over Ω, results in following:

$$\int_\Omega w \rho c_p \frac{\partial T}{\partial t} d\Omega - \int_\Omega w \rho H d\Omega = -\int_\Omega w (\frac{\partial}{\partial x} q_x + \frac{\partial}{\partial y} q_y) d\Omega \tag{3.5}$$

Using integration by parts for the right-hand-side of Equation 3.5:

$$\int_\Omega w (\frac{\partial}{\partial x} q_x + \frac{\partial}{\partial y} q_y) d\Omega = \int_\Omega (\frac{\partial}{\partial x} w q_x + \frac{\partial}{\partial y} w q_y) d\Omega - \int_\Omega (q_x \frac{\partial}{\partial x} w + q_y \frac{\partial}{\partial y} w) d\Omega \tag{3.6}$$

as well as result from Ostrogradsky-Gauss' divergence theorem:

$$\int_\Omega (\frac{\partial}{\partial x} w q_x + \frac{\partial}{\partial y} w q_y) d\Omega = \int_\Gamma w (q_x n_x + q_y n_y) d\Gamma \tag{3.7}$$

following relation is obtained:

$$\int_\Omega w (\frac{\partial}{\partial x} q_x + \frac{\partial}{\partial y} q_y) d\Omega = \int_\Gamma w (q_x n_x + q_y n_y) d\Gamma - \int_\Omega (q_x \frac{\partial}{\partial x} w + q_y \frac{\partial}{\partial y} w) d\Omega \tag{3.8}$$

Using this relation, Equation 3.5 may be rewritten as following:

$$\int_\Omega w\rho c_p \frac{\partial T}{\partial t} d\Omega - \int_\Omega w\rho H d\Omega - \int_\Omega (q_x \frac{\partial}{\partial x} w + q_y \frac{\partial}{\partial y} w) d\Omega = -\int_\Gamma w(q_x n_x + q_y n_y) d\Gamma \quad (3.9)$$

Applying Neumann boundary conditions and remembering that $w((x, y) \in \Gamma_g) = 0$, we finally arrive at the *weak formulation* of Equation 3.1:

$$\int_\Omega w\rho c_p \frac{\partial T}{\partial t} d\Omega - \int_\Omega w\rho H d\Omega + \int_\Omega (\frac{\partial T}{\partial x}\frac{\partial w}{\partial x} + \frac{\partial T}{\partial y}\frac{\partial w}{\partial y}) d\Omega = \int_{\Gamma_h} whd\Gamma_h \quad (3.10)$$

where the expression for thermal flux from Equation 3.1 was also used. The fact that the Neumann boundary conditions were automatically incorporated into this formulation through divergence theorem, is the reason why they are also called the natural boundary conditions.
At this point, it is useful to introduce following operators to simplify further writing:

$$\begin{aligned} a(w, T) &= \int_\Omega (\frac{\partial w}{\partial x}\frac{\partial T}{\partial x} + \frac{\partial w}{\partial y}\frac{\partial T}{\partial y}) d\Omega \\ (w, f) &= \int_\Omega wf d\Omega \\ (w, h)_\Gamma &= \int_\Gamma whd\Gamma \end{aligned} \quad (3.11)$$

These three operators are symmetric bilinear forms, meaning that they satisfy following relations, exemplified for operator $a(\cdot, \cdot)$:

$$\begin{aligned} a(u, v) &= a(v, u) \\ a(c_1 u + c_1 v, z) &= c_1 a(u, z) + c_2 a(v, z) \end{aligned} \quad (3.12)$$

Using Equation 3.11, the weak form may be expressed as following:

$$a(w, T) = -(w, \rho c_p \frac{\partial T}{\partial t}) + (w, \rho H) + (w, h)_\Gamma \quad (3.13)$$

3.3 FEM discretization

Approximate solution of Equation 3.13 is found using FEM. The the weak form is discretized using finite element basis functions, or shape functions, with compact support. Approximate solution is expressed as a linear combination of these. When the weighting functions, w, are expressed as a linear combination of the same shape functions used to approximate the solution, the method is called the Galerkin FEM, or GFEM. In this study, we use piecewise polynomials for the shape functions.
We denote the finite-dimensional approximations of $\mathcal{S}$ and $\mathcal{V}$ as $\mathcal{S}^h$ and $\mathcal{V}^h$, respectively.

Observing that the collections of functions comprising $\mathcal{S}$ and $\mathcal{V}$ only differ from each other at the boundary Γ_g, we may construct a function in the solution space, $s^h \in \mathcal{S}$, for any member of the variational space, $v^h \in \mathcal{V}$, as following:

$$\begin{aligned} s^h &= v^h + g^h \\ g^h((x,y) \in \Gamma_g) &= g \end{aligned} \tag{3.14}$$

Remembering the bilinearity of the operators in Equation 3.11, the weak form in Equation 3.13 may be rewritten as following:

$$\begin{aligned} a(w^h, v^h + g^h) &= -(w^h, \rho c_p \frac{\partial (v^h + g^h)}{\partial t}) + (w^h, \rho H) + (w^h, h)_\Gamma \\ a(w^h, v^h) &= -(w^h, \rho c_p \frac{\partial v^h}{\partial t}) + (w^h, \rho H) + (w^h, h)_\Gamma - a(w^h, g^h) \end{aligned} \tag{3.15}$$

where independence of boundary function g^h on time was assumed.
The solution of the discretized weak form is defined in a finite number of points, or nodes, that lie within the domain Ω and on the boundary segments Γ_g and Γ_h. We denote the set of all nodes as η and the Dirichlet-nodes as η_g. To construct the discretized variational space $\mathcal{V}^h$, we introduce basis functions $N_A(x,y)$, where $A = 1, 2..\eta$. Each node A, with position (x_A, y_A), has a shape function $N_A(x,y)$ associated with it.

$$\begin{aligned} N_A(x_B, y_B) &= \delta_{AB} \\ N_A((x,y) \in \Gamma_g) &= 0, \quad A \in \eta - \eta_g \\ N_A((x,y) \in \Gamma_g) &= 1, \quad A \in \eta_g \end{aligned} \tag{3.16}$$

Any function $w^h, v^h, g^h \in \mathcal{V}^h$ can thus be expressed as following linear combinations:

$$\begin{aligned} w^h &= \sum_{A \in \eta - \eta_g} c_A N_A(x,y) \\ v^h &= \sum_{A \in \eta - \eta_g} T_A N_A(x,y) \\ g^h &= \sum_{A \in \eta_g} g_A N_A(x,y), \quad g_A = g(x_A, y_A) \end{aligned} \tag{3.17}$$

The weak form in Equation 3.15 can be expressed in terms of linear combination of shape functions as following:

$$
\begin{aligned}
a(\sum_{A\in\eta-\eta_g} c_A N_A, \sum_{B\in\eta-\eta_g} T_B N_B) = \\
&- (\sum_{A\in\eta-\eta_g} c_A N_A, \sum_{B\in\eta-\eta_g} \rho c_p \frac{\partial T_B}{\partial t} N_B) \\
&+ (\sum_{A\in\eta-\eta_g} c_A N_A, \rho H) + (\sum_{A\in\eta-\eta_g} c_A N_A, h)_\Gamma \\
&- a(\sum_{A\in\eta-\eta_g} c_A N_A, \sum_{B\in\eta_g} g_B N_B)
\end{aligned} \tag{3.18}
$$

Using the bilinearity of the operators, the expression may be simplified to:

$$
\begin{aligned}
\sum_{A\in\eta-\eta_g} c_A(\sum_{B\in\eta-\eta_g} a(N_A, N_B) T_B) = \\
&- \sum_{A\in\eta-\eta_g} c_A(\sum_{B\in\eta-\eta_g} (N_A, \rho c_p N_B) \frac{\partial T_B}{\partial t}) \\
&+ \sum_{A\in\eta-\eta_g} c_A(N_A, \rho H) + \sum_{A\in\eta-\eta_g} c_A(N_A, h)_\Gamma \\
&- \sum_{A\in\eta-\eta_g} c_A(\sum_{B\in\eta_g} a(N_A, N_B) g_B)
\end{aligned} \tag{3.19}
$$

Since the coefficients c_A are arbitrary, Equation 3.19 must hold for each A. Hence, we have the following system of $\eta - \eta_g$ linear equations with $\eta - \eta_g$ unknowns, namely d_B's:

$$
\begin{aligned}
&\sum_{B\in\eta-\eta_g} a(N_A, N_B) T_B = \\
&- \sum_{B\in\eta-\eta_g} (N_A, \rho c_p N_B) \frac{\partial T_B}{\partial t} + (N_A, \rho H) + (N_A, h)_\Gamma - \sum_{B\in\eta_g} a(N_A, N_B) g_B
\end{aligned} \tag{3.20}
$$

3.4 Matrix form

Equation 3.20 may be expressed in a matrix form. Operator $a(N_A, N_B)$ forms the stiffness matrix $\mathbf{K}$, while operator $(N_A, \rho c_p N_B)$ forms them mass-matrix $\mathbf{M}$. The right-hand-side (RHS) of Equation 3.20 is combined into the vector $\mathbf{F}$. Resulting matrix form of the

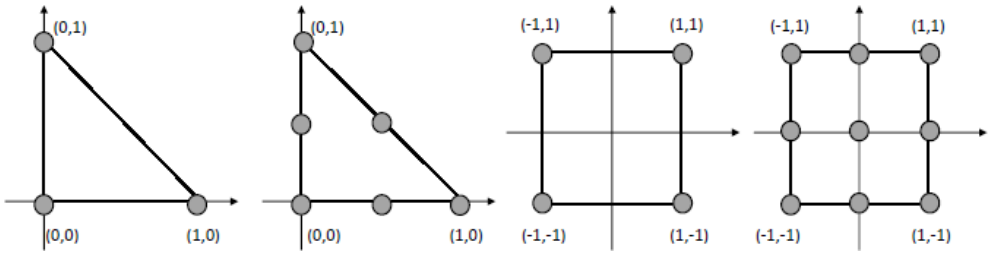

Figure 3.1: 3- and 6-nodes Triangle-element and 4- and 9-nodes Quad-elements

discretized weak formulation is as following:

$$\mathbf{K} = a(N_A, N_B) = \int_\Omega (\frac{\partial N_A}{\partial x}\frac{\partial N_B}{\partial x} + \frac{\partial N_A}{\partial y}\frac{\partial N_B}{\partial y}) d\Omega$$

$$\mathbf{M} = (N_A, \rho c_p N_B) = \int_\Omega N_A \rho c_p N_B d\Omega$$

$$\mathbf{F} = (N_A, \rho H) + (N_A, h)_\Gamma - \sum_{B \in \eta_g} a(N_A, N_B) g_B =$$

$$= \int_\Omega N_A \rho H d\Omega + \int_\Gamma N_A h d\Gamma - \sum_{B \in \eta_g} \int_\Omega (\frac{\partial N_A}{\partial x}\frac{\partial N_B}{\partial x} + \frac{\partial N_A}{\partial y}\frac{\partial N_B}{\partial y}) \cdot g_B d\Omega$$

$$\mathbf{K}T + \mathbf{M}v = \mathbf{F}, \quad v = \frac{\partial T}{\partial t} \tag{3.21}$$

3.5 Isoparametric representation

So far, the problem has been discussed in the global point of view, with shape functions defined everywhere in the domain. We now introduce the local, or element, point of view, and construct $\mathbf{K}$, $\mathbf{M}$ and $\mathbf{F}$ by summing the contributions of element stiffness and mass matrices, and right hand side vector:

$$\mathbf{K} = \sum_{e=1}^{n_{el}} \mathbf{K^e}, \quad \mathbf{M} = \sum_{e=1}^{n_{el}} \mathbf{M^e}, \quad \mathbf{F} = \sum_{e=1}^{n_{el}} \mathbf{F^e} \tag{3.22}$$

where n_{el} is the number of elements. Coordinates (x, y) and node-numbering $A = 1, 2, ...\eta$ are defined in the global point of view. For the local point of view, we define coordinates (ξ, ν) and node-numbering $a = 1, 2, ...n$, where n is the number of nodes in each element, and hence the dimension of the piecewise polynomials that define shape functions. In this study, four different element-types are investigated, as depicted in Figure 3.1. To map elements from local to global systems, we use the same shape functions that we used to

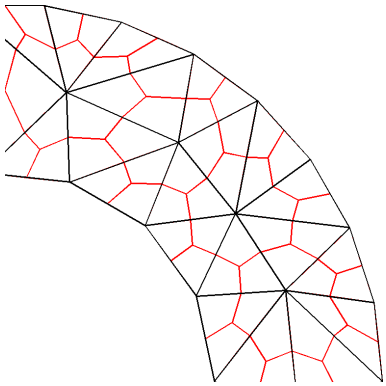

Figure 3.2: An unstructured triangular mesh split into quadratic elements.

discretize the weak form. This method is known as isoparametric representation. Mapping from local to global system is thus given by:

$$\begin{aligned} x &= \sum_{a=1}^{n} x_i N_i(\xi, \nu) \\ y &= \sum_{a=1}^{n} y_i N_i(\xi, \nu) \\ (x_i, y_i) &= (x(\xi_i, \nu_i), y(\xi_i, \nu_i)) \end{aligned} \tag{3.23}$$

where (x_i, y_i) and (ξ_i, ν_i) are the global and local coordinates of the element nodes, respectively. After the approximate solution T_A is obtained for the all the nodes, $A = 1, 2, ...\eta$, the solution value in any point (x, y) of the domain may be estimated:

$$T(x, y) = \sum_{a=1}^{n} d_i N_i(\xi, \nu) \tag{3.24}$$

3.6 Discretization in space

We use triangular mesh generator to construct an unstructured grid with triangular elements. The size of the elements is constrained by prescribing their maximum area. The order of the shape functions used for these elements is determined by the number of element nodes. To generate an unstructured mesh consisting of quads, the elements produced by the triangular mesh generator are split into three quadratic elements, as illustrated in Figure 3.2.
The local coordinates of the four types of elements we used for discretization in this study

are presented in Figure 3.1. It is convenient to define the following functions of local coordinates:

$$\begin{aligned} w &= 1 - \xi - \nu \\ u &= \xi \\ v &= \nu \end{aligned} \tag{3.25}$$

Shape functions for the three-node triangular elements can now be expressed as following:

$$\begin{aligned} N_1(\xi, \nu) &= w \\ N_2(\xi, \nu) &= u \\ N_3(\xi, \nu) &= v \end{aligned} \tag{3.26}$$

For the six-node triangular elements, the shape functions are:

$$\begin{aligned} N_1(\xi, \nu) &= w * (2 * w - 1) \\ N_2(\xi, \nu) &= u * (2 * u - 1) \\ N_3(\xi, \nu) &= v * (2 * v - 1) \\ N_4(\xi, \nu) &= 4 * u * v \\ N_5(\xi, \nu) &= 4 * w * v \\ N_6(\xi, \nu) &= 4 * w * u \end{aligned} \tag{3.27}$$

We use Lagrange polynomials as shape functions for the quadratic elements. In one dimension the Lagrange polynomials are given by:

$$P_i(\xi) = \prod_{a=1, a \neq i}^{n} \frac{\xi - \xi_a}{\xi_i - \xi_a} \tag{3.28}$$

and in two dimensions:

$$P_{ij}(\xi, \nu) = P_i(\xi) P_j(\nu) \tag{3.29}$$

The shape functions for the four-node quadratic elements are thus given by:

$$\begin{aligned} N_1(\xi, \nu) &= P_{11}(\xi, \nu) \\ N_2(\xi, \nu) &= P_{21}(\xi, \nu) \\ N_3(\xi, \nu) &= P_{22}(\xi, \nu) \\ N_4(\xi, \nu) &= P_{12}(\xi, \nu) \end{aligned} \tag{3.30}$$

These are also the first four shape functions for the nine-node quadratic elements, and the other five shape functions are found analogously.

3.7 Discretization in time

To solve Equation 3.21, a discretization in time is needed. To do this, we consider the general trapezoidal family of methods, which are finite difference methods, stated in following equations:

$$\begin{aligned} \mathbf{K}T_{n+1} + \mathbf{M}v_{n+1} &= \mathbf{F}_{n+1} \\ T_{n+1} &= T_n + \triangle t v_{n+\alpha} \\ v_{n+\alpha} &= (1-\alpha)v_n + \alpha v_{n+1} \end{aligned} \tag{3.31}$$

In this section we derive an implementation of the Equations 3.31 that eliminates v_n's. Since the weak form must hold in all points in time, we consider advancing Equation 3.21 from time t_n to time $t_{n+\alpha\triangle t}$. This gives following:

$$\mathbf{K}T_{n+\alpha} + \mathbf{M}v_{n+\alpha} = \mathbf{F}_{n+\alpha} \tag{3.32}$$

Using Equations 3.31, following relations are obtained:

$$\begin{aligned} v_{n+\alpha} &= \frac{T_{n+1} - T_n}{\triangle t} \\ T_{n+\alpha} &= T_n + \alpha\triangle t v_{n+\alpha} = T_n + \alpha\triangle t \frac{T_{n+1} - T_n}{\triangle t} = (1-\alpha)T_n + \alpha T_{n+1} \\ \mathbf{F}_{n+\alpha} &= (1-\alpha)\mathbf{F}_n + \alpha\mathbf{F}_{n+1} \end{aligned} \tag{3.33}$$

Insertion into Equation 3.32, multiplying by $\triangle t$ and some rearranging results in the following expression:

$$(\mathbf{M} + \alpha\triangle t\mathbf{K})T_{n+1} = (\mathbf{M} - (1-\alpha)\triangle t\mathbf{K})T_n + \triangle t(\alpha\mathbf{F}_{n+1} + (1-\alpha)\mathbf{F}_n) \tag{3.34}$$

Parameter α is a value between $[0, 1]$. The time discretization schemes resulting from values of α equal to 0, $\frac{1}{2}$ and 1 are known as the forward Euler, Crank-Nicolson, and backward Euler schemes, respectively. In this study, we choose to implement the fully implicit backward Euler scheme. This scheme is first order accurate and is unconditionally stable. The final linear system of equations that we implement in MATLAB to obtain the approximate solution of the transient heat equation is as following:

$$(\mathbf{M} + \triangle t\mathbf{K})T_{n+1} = \mathbf{M}T_n + \triangle t\mathbf{F}_{n+1} \tag{3.35}$$

3.8 Testing of the FEM Thermal Diffusion solver

3.8.1 Steady-state diffusion

Thermal solver outlined above is benchmarked by applying it to problems with known analytical solutions. Our first test-application is a steady-state problem, formulated as

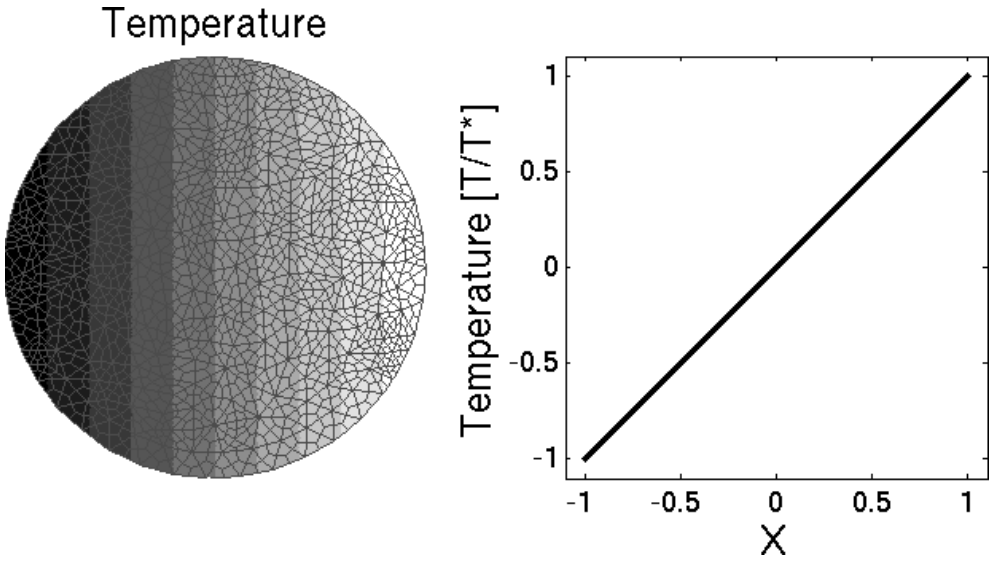

Figure 3.3: Solution of a steady state heat diffusion problem for a cylinder, with boundary conditions given by a linear function of x. We use an unstructured grid constituted of 9-node quads. Maximum element size of the triangular grid that was used to construct the quads is $1.5 \cdot 10^{-2}[R^2]$.

following:

$$0 = \frac{\partial^2 T}{\partial x^2} + \frac{\partial^2 T}{\partial y^2} \tag{3.36}$$

with boundary conditions given by:

$$T(x, y, t) = x, \quad (x, y) \in \Gamma_g$$

The analytical solution to this problem is a temperature distribution that is a linear function of x. In Figure 3.3, the solution obtained using the FEM diffusion solver is demonstrated for an unstructured grid constituted of 3-nodes triangles. The solutions obtained using 6-nodes triangles and 4- and 9-nodes quads is identical to this one. It may be observed that the correct solution is, indeed, reproduced.

3.8.2 Transient diffusion

Analytical solution of a cooling cylinder problem

The transient problem we choose to study is cooling of a circular cylinder. We assume axis symmetry and no variation in z-direction, which reduces the problem to two dimensions: radius r and time t. Following derivation closely follows (Boas, 1983). In cylindrical

coordintes the problem is stated as following:

$$\begin{aligned} &\frac{\partial T}{\partial t} = \frac{1}{r}\frac{\partial}{\partial r}(r\frac{\partial T}{\partial r}) \\ &T(r=0,t) < \infty \\ &T(r=r_b,t) = 0 \\ &T(r,t=0) = 1 \end{aligned} \tag{3.37}$$

where r_b is the radius of the cylinder. Separation of variables results in the following:

$$\begin{aligned} &T(r,t) = R(r)\cdot F(t) \\ &\frac{1}{F}\frac{\partial F}{\partial t} = \frac{1}{rR}\frac{\partial}{\partial r}(r\frac{\partial R}{\partial r}) = -K^2 \end{aligned} \tag{3.38}$$

where the separation constant is expressed as $-K^2$ since we want the temperature to tend to zero as time goes to infinity. The function of time can be integrated to give:

$$F(t) = Ae^{-K^2 t} \tag{3.39}$$

where A is a constant. Equation for the radial component of $T(r,t)$ can be rewritten as following:

$$r\frac{\partial}{\partial r}(r\frac{\partial R}{\partial r}) + (r^2K^2 - 0^2)R = 0 \tag{3.40}$$

Equation 3.40 is recognized as Bessel's equation of zeroth order and has the general solution:

$$R(r) = aJ_0(Kr) + bY_0(Kr) \tag{3.41}$$

where a and b are constants and J_0 and Y_0 are Bessel functions. The function Y_0 is singular at the origin, thus we must have $b = 0$ such that $T(r=0,t)$ is finite. Boundary condition $T(r=r_b,t) = 0$ implies that $J_0(Kr_b) = 0$, and therefor possible values of Kr_b are the roots of J_0. We define a new parameter $g_m = Kr_b$, for $m = 1, 2, 3...$ and express the solution as following:

$$T(r,t) = \sum_{m=1}^{\infty} a_m J_0(\frac{g_m}{r_b}r)\cdot Ae^{-(\frac{g_m}{r_b})^2 t} \tag{3.42}$$

The constants a_m can be determined using boundary conditions and the orthogonality of Bessel functions of the same order and kind. Applying the last two relations of Equation 3.38 to Equation 3.42 results in the following expression:

$$\frac{1}{A} = \sum_{m=1}^{\infty} a_m J_0(\frac{g_m}{r_b}r) \tag{3.43}$$

Multiplying the solution by $rJ_0(\frac{g_\mu}{r_b}r)$, where $\mu = 1, 2, 3...$, and integrating from $r = 0$ to $r = r_b$, such that only the terms $m = \mu$ are non-zero due to the orthogonality of Bessel functions, allows to express the solution as following:

$$\frac{1}{A}\int_0^{r_b} rJ_0(\frac{g_\mu}{r_b}r)dr = a_\mu \int_0^{r_b} r[J_0(\frac{g_\mu}{r_b}r)]^2 dr \tag{3.44}$$

Equation 3.44 may be rewritten using recurrence relations of ordinary Bessel functions:
Left-hand side:

$$\begin{aligned}
\frac{d}{dr}(rJ_1(r)) &= rJ_0(r) \quad \text{Recurrence relation} \\
\frac{r_b}{g_\mu}\frac{d}{dr}[(\frac{g_\mu}{r_b}r)J_1(\frac{g_\mu}{r_b}r)] &= (\frac{g_\mu}{r_b}r)J_0(\frac{g_\mu}{r_b}r) \\
\int_0^{r_b}\frac{d}{dr}[rJ_1(\frac{g_\mu}{r_b}r)]dr &= \frac{g_\mu}{r_b}\int_0^{r_b} rJ_0(\frac{g_\mu}{r_b}r)dr \\
\int_0^{r_b} rJ_0(\frac{g_\mu}{r_b}r)dr &= \frac{r_b^2}{g_\mu}J_1(g_\mu)
\end{aligned} \tag{3.45}$$

Right-hand side:

$$\begin{aligned}
\int_0^1 rJ_p(\alpha r)J_p(\beta r)dr &= \begin{cases} 0 & \text{for} \quad \alpha \neq \beta \\ \frac{1}{2}J_{p+1}^2(\alpha) & \text{for} \quad \alpha = \beta \end{cases} \quad \text{Orthogonality} \\
\int_0^{r_b} r[J_0(\frac{g_\mu}{r_b}r)]^2dr &= \frac{r_b^2}{2}J_1^2(g_\mu)
\end{aligned} \tag{3.46}$$

Combining these two results gives the following expression for the constants a_μ:

$$\begin{aligned}
\frac{1}{A}\frac{r_b^2}{g_\mu}J_1(g_\mu) &= a_\mu\frac{r_b^2}{2}J_1^2(g_\mu) \\
a_\mu &= \frac{2}{g_\mu J_1(g_\mu)}\frac{1}{A}
\end{aligned} \tag{3.47}$$

Finally, the complete solution stated in Equation 3.42 may be expressed as:

$$T(r,t) = 2\sum_{m=1}^{\infty}\frac{J_0(\frac{g_m}{r_b}r)}{g_\mu J_1(g_m)}\cdot e^{-(\frac{g_m}{r_b})^2 t} \tag{3.48}$$

Numerical solution of a cooling cylinder problem

We apply FEM diffusion solver to obtain the transient solution of a cooling cylinder problem that is stated in Equation 3.38 and has an analytical solution given by Equation 3.48. The intial and boundary conditions are the same as in Equation 3.38. We prescribe the cylinder radius $r_b = 1$. Roots of the Bessel functions, that are a part of the analytical solution, are found numerically and it is assumed that the sum of the first 80 positive roots is a good approximation to the infinite sum.
We compare the numerical and analytical solutions after the total simulation time of $3\cdot10^{-4}$, which is an early stage of cooling compared to the time it takes to reach a steady-state. The time step we use is $\triangle t = 1\cdot10^{-5}$. The results for the 3-node triangles, 4-node quads and

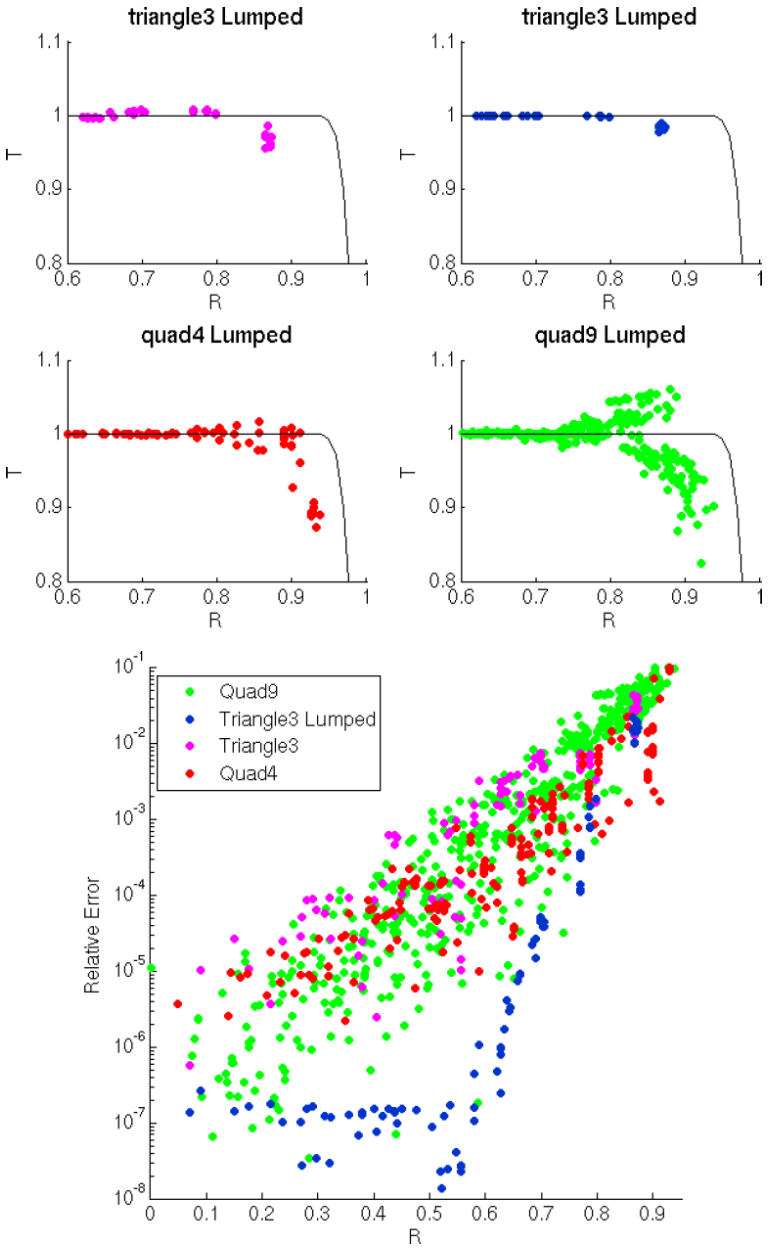

Figure 3.4: *Top*: Numerical and analytical solutions of the cooling cylinder problem. Scaled values of temperature and radius are plotted. For the numerical solutions, grids consisting of 3-node triangles, 4-node quads and 9-node quads are used. The solution obtained with a lumped mass matrix for the 3-node triangle grid is also presented. *Bottom*: Relative error of the numerically obtained solutions. The timestep size is $\triangle t = 1 \cdot 10^{-5}[\frac{R^2}{\kappa}]$ and the total simulation time is $1.5 \cdot 10^{-4}[\frac{R^2}{\kappa}]$. Maximum element size is $2 \cdot 10^{-2}[R^2]$.

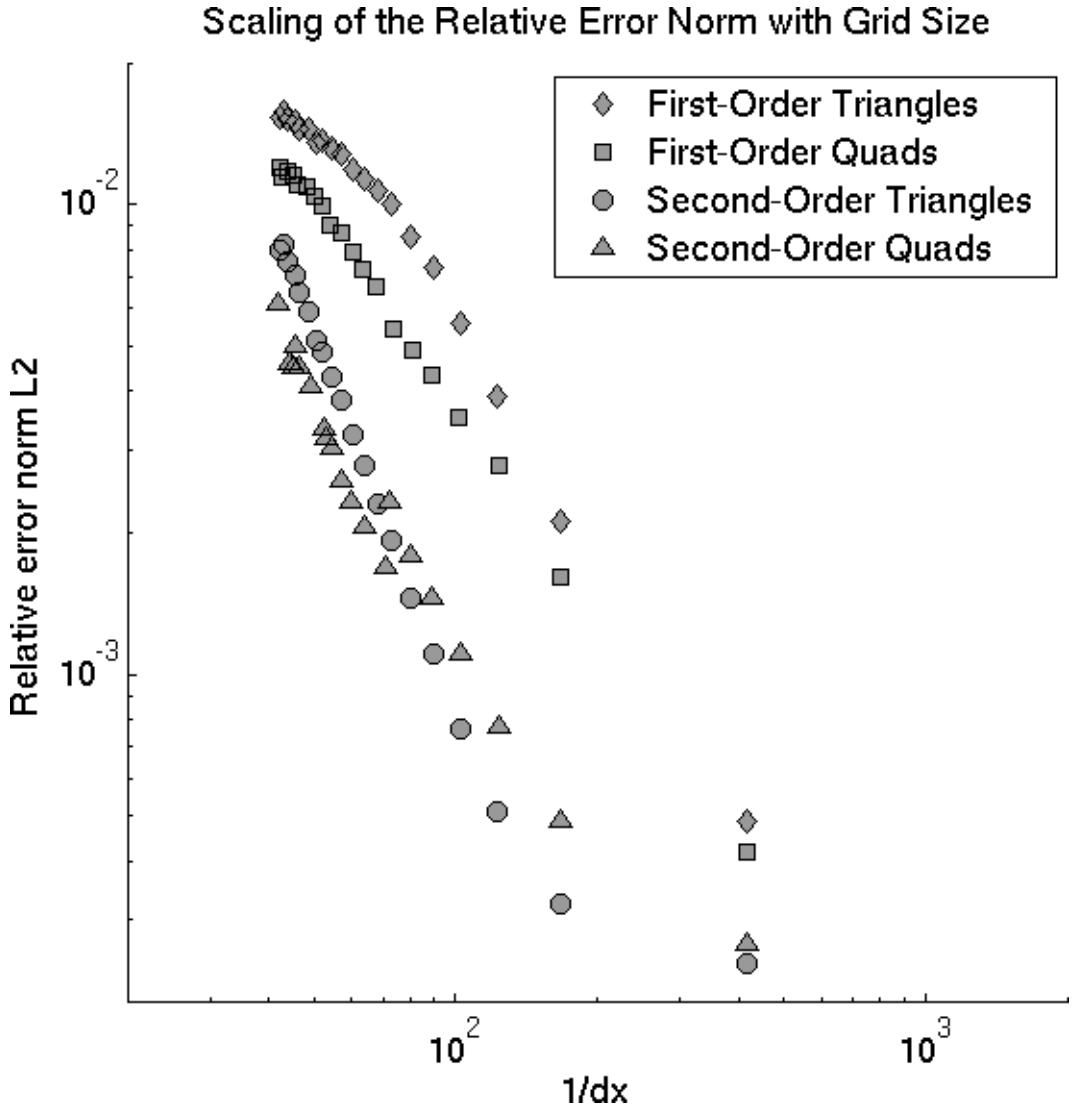

Figure 3.5: Scaling of the relative error norm with grid size for triangular and quadratic elements. Error norm is computed after the total simulation time of $1.5 \cdot 10^{-4}[\frac{R^2}{\kappa}]$, with timestep size $\triangle t = 1 \cdot 10^{-5}[\frac{R^2}{\kappa}]$

9-node quads are presented in Figure 3.4. It may be observed that during the intial stage of cooling, the numerically calculated temperature in some of the nodes actually increases. Introducing lumping of the mass matrix in the FEM diffusion solver for the first-order elements results in a monotonically decreasing temperature, as demonstrated for the 3-node triangles in Figure 3.4.
Some temperature oscillations are observed in some of the nodes during the simulation with second-order elements, as demonstrated for 9-node quads in Figure 3.4. The origin of this artificial oscillation lies in the initial temperature distribution. The latter is given by a function with rapidly changing higher derivatives at the outer boundary, where a sharp temperature drop is applied as a thermal boundary condition. Using higher-order polynomials to interpolate this function results in oscillations between the nodes. This artifact is absent when first-order polynomials are used, which are generally better suited for interpolating functions with rapidly changing higher derivatives.
The temperature distribution becomes smoother with time, as a result of diffusion, and hence more accurately interpolated by the higher-order polynomials. Followingly, the oscillations will dissipate earlier in the simulation when a larger timestep is used.
The oscillation of temperature values due to higher-order polynomial interpolation may be decreased or completely avoided by prescribing a smoother initial temperature distribution.

3.8.3 Grid Refinement vs Higher-Order Shape Functions

The accuracy of the numerical solution may be improved by refining the grid or increasing the order of the shape functions. We wish to estimate which of the approaches gives most accuracy gain.
We use a lumped mass matrix for the first-order elements. The timestep size is $\triangle t = 1 \cdot 10^{-6}$ and the total simulation time is $1.5 \cdot 10^{-4}$. The simulation is performed for different element types and grid sizes. For each configuration the relative error norm L2 is computed as

$$L2 = \sqrt{\frac{\int_\Omega (T_{exact} - T_{numerical})^2 d\Omega}{\int_\Omega T_{exact}^2 d\Omega}} \tag{3.49}$$

Scaling of the relative error norm with grid size for triangular and quadratic elements is presented in Figure 3.5. The scaling of the error appears to be of first order for the first-order elements, and of second and third order for the second-order quads and triangles, respectively.

Chapter 4

Advection solvers

Transport of material due to convective dynamics is modeled by solving the disretized advection equation. This involves numerical integration of an ordinary differential equation (ODE). In this chapter we present comparison of three methods to solve this problem: Euler, fourth-order Runge-Kutta and fifth-order Runge-Kutta with adaptive stepsize control. Their performance is evaluated by applying them to one- and two-dimensional initial-value problems. The ODE-solvers are compared based on the number of integrand-evaluations required each step and the resulting global error. Comparison is performed for different step-sizes.

4.0.4 Outline of the problem

Given an ordinary differential equation (ODE):

$$\frac{d\vec{x}}{dt} = \vec{v} \tag{4.1}$$

and an initial value $\vec{x}_i = \vec{x}(t_i)$, evaluation of function $\vec{x}$ in point t_{i+1}, $\vec{x}_{i+1} = \vec{x}(t_{i+1})$, can be obtained from:

$$\vec{x}_{i+1} = \vec{x}_i + \int_{t_i}^{t_{i+1}} \vec{v}\,\mathrm{d}t \tag{4.2}$$

This problem is characterized as an initial value problem. Numerical techniques for integrating Equation 4.1 as accurately as possible, while keeping the number of function evaluations of the integrand as low as possible, are the focus of this study.

4.0.5 Outline of the methods

In the following, three different ODE-solvers are presented. The leading term of the truncation error, denoted $O(\triangle t^{n+1})$, constitutes the *local* error. The *global* error, which is the

accumulation of local errors at the end of the integration, is then of nth order, making the method also an nth order method. Description of the methods closely follows (Press et al., 2007).

Euler method

Expanding $\vec{x}_{i+1}$ in the Taylor series and truncating it at the first derivative, results in the following expression for the updated positions:

$$\vec{x}_{i+1} = \vec{x}_i + \triangle t \vec{v}(t_i, \vec{x}_i) + O(\triangle t^2) \tag{4.3}$$

where Equation 4.1 has been used. Equation 4.3 is the formula for Euler's method. As indicated in the error term, it is locally second order accurate, making Euler's method globally only first-order accurate. This method requires the derivative, or velocity, information at the beginning of the time-interval in order to evaluate the function at the end of the interval. This makes it an explicit method. The advantage of this method is that the integrand has to be evaluated only once for each time step.

Fourth-order Runge-Kutta method

Improved accuracy in the evaluation of the integral may be obtained by introducing intermediate steps. This is the philosophy behind the Runge-Kutta methods. Fourth-order Runge-Kutta method uses Simpson's rule to evaluate the integral on the right-hand side of Equation 4.2, but with midpoint evaluation split in two steps. The position of the intermediate step is found using Euler's method. The method is outlined in the following:

$$\begin{aligned} k_1 &= \triangle t \vec{v}(t_i, \vec{x}_i) \\ k_2 &= \triangle t \vec{v}(t_i + \frac{1}{2}\triangle t, \vec{x}_i + \frac{1}{2}k_1) \\ k_3 &= \triangle t \vec{v}(t_i + \frac{1}{2}\triangle t, \vec{x}_i + \frac{1}{2}k_2) \\ k_4 &= \triangle t \vec{v}(t_i + \triangle t, \vec{x}_i + k_3) \\ \vec{x}_{i+1} &= \vec{x}_i + \frac{1}{6}k_1 + \frac{1}{3}k_2 + \frac{1}{3}k_3 + \frac{1}{6}k_4 + O(\triangle t^5) \end{aligned} \tag{4.4}$$

As indicated in the error term, it is globally fourth-order accurate and it requires four evaluations of the integrand for each timestep.

Fifth-order Runge-Kutta method with adaptive stepsize control (RK45)

Accuracy in the evaluation of the integral may be further improved by introducing adaptive stepsize control. The goal is to satisfy some predetermined accuracy constraint in the

c_i	a_{ij}						$\hat{b}_i$	b_i
0							$\frac{35}{384}$	$\frac{5179}{57600}$
$\frac{1}{5}$	$\frac{1}{5}$						0	0
$\frac{3}{10}$	$\frac{3}{40}$	$\frac{9}{40}$					$\frac{500}{1113}$	$\frac{7571}{16695}$
$\frac{4}{5}$	$\frac{44}{45}$	$-\frac{56}{15}$	$\frac{32}{9}$				$\frac{125}{192}$	$\frac{393}{640}$
$\frac{8}{9}$	$\frac{19372}{6561}$	$-\frac{25360}{2187}$	$\frac{64448}{6561}$	$-\frac{212}{729}$			$-\frac{2187}{6784}$	$-\frac{92097}{339200}$
1	$\frac{9017}{3168}$	$-\frac{355}{33}$	$\frac{46732}{5247}$	$\frac{49}{176}$	$-\frac{5103}{18656}$		$\frac{11}{84}$	$\frac{187}{2100}$
1	$\frac{35}{384}$	0	$\frac{500}{1113}$	$\frac{125}{192}$	$-\frac{2187}{6784}$	$\frac{11}{84}$	0	$\frac{1}{40}$

Figure 4.1: Dormand-Prince 5(4) Parameters for Embedded Runge-Kutta Method

solution with minimum computational effort, or as large timestep as possible. This is achieved by introducing error control. Embedded Runge-Kutta formulas examplify this approach. In the following, a fifth-order Runge-Kutta method with stepsize control, RK45, is outlined.

As in previously described fourth-order Runge-Kutta method, a weighted combination of function evaluations is used. There is a combination of six functions that gives a fifth-order method, while another combination of six functions gives a fourth-order method. Difference between the two estimates of the integral is used to estimate the truncation error and adjust the stepsize. The general fifth-order Runge-Kutta method is as following:

$$\begin{aligned} k_1 &= \triangle t\vec{v}(t_i, \vec{x}_i) \\ k_2 &= \triangle t\vec{v}(t_i + c_2\triangle t, \vec{x}_i + a_{21}k_1) \\ &\dots \\ k_6 &= \triangle t\vec{v}(t_i + c_6\triangle t, \vec{x}_i + a_{61}k_1 + a_{62}k_2 + \ldots + a_{65}k_5) \\ \vec{x}_{i+1} &= \vec{x}_i + b_1k_1 + b_2k_2 + \ldots + b_6k_6 + O(\triangle t^6) \end{aligned} \tag{4.5}$$

The embedded fourth-order formula is as following:

$$\vec{x}^*_{i+1} = \vec{x}_i + b^*_1k_1 + b^*_2k_2 + \ldots + b^*_6k_6 + O(\triangle t^5) \tag{4.6}$$

Hence, the truncation error estimate is given by

$$\triangle = \vec{x}_{i+1} - \vec{x}^*_{i+1} \tag{4.7}$$

Various constants used in Equation 4.5 and Equation 4.6 are those found by Dorman and Prince (Dormand and Prince, 1980) and are presented in Figure 4.1. The error is required

to satisfy following:

$$|\triangle| = |\vec{x}_{i+1} - \vec{x}^*_{i+1}| \leq scale \tag{4.8}$$

where the *scale* is given by

$$scale = atol + |x|rtol \tag{4.9}$$

and *atol* and *rtol* are absolute and relative error tolerances, respectively, which are both chosen to be equal to 10^{-6}. Relative tolerance measures the error relative to the integrand-value at the end of the step and represents a percentage of the integrands value. Absolute tolerance is a threshold error value and represents the acceptable error as the integrands value approaches zero. $|x|$ is defined as $max(|x_i|, |x_{i+1}|)$. The error after each time step is given by the Euclidian norm:

$$err = \sqrt{\frac{1}{N}\sum_{j=1}^{N}(\frac{\triangle_i}{scale_i})^2} \tag{4.10}$$

where N is the number of equations, or markers in this case. As seen from Equation 4.5 and Equation 4.6, $\triangle$ scales globally as $\triangle t^5$. Error values, err_0 and err_1, produced by two different step-sizes, $\triangle t_0$ and $\triangle t_1$, are thus related as following:

$$\triangle t_0 = \triangle t_1 |\frac{err_0}{err_1}|^{\frac{1}{5}} \tag{4.11}$$

Taking $err_0 = 1$ as the desired error value, Equation 4.11 provides the most efficient step-size, in terms of originally attempted stepsize and its error. The RK45 method requires 6 evaluations of the integrand for each accepted timestep.
In this study we use RK45 solver provided by MATLAB, an inbuilt function called ode45. As its input parameters, it takes a function handle to evaluate the integrand, an interval over which the integral is estimated and the value of integrand at the beginning of this interval. Optionally, one may specify the absolute and relative tolerances to control the error. The error in ode45 is given by

$$e_i \leq max(rtol \cdot |y_i|, atol_i) \tag{4.12}$$

During each step, the solver computes the integrand value at the end of the step, as well as the local error. The latter is then compared to the value given by equation 4.12. If local error is greater than than e_i, the stepsize is reduced and the solver tries again. Applying ode45 to the entire integrational interval at once will ideally result in the prescribed error. Whether this is actually the case is investigated in the next section. However, applying this solver to the coupled advection-diffusion problem, we are forced to split the time-interval into timesteps, since the diffusion problem is solved simultaneously with the advection. Hence, the error prescribed to ode45 will accumulate with each timestep, resulting in lower accuracy.

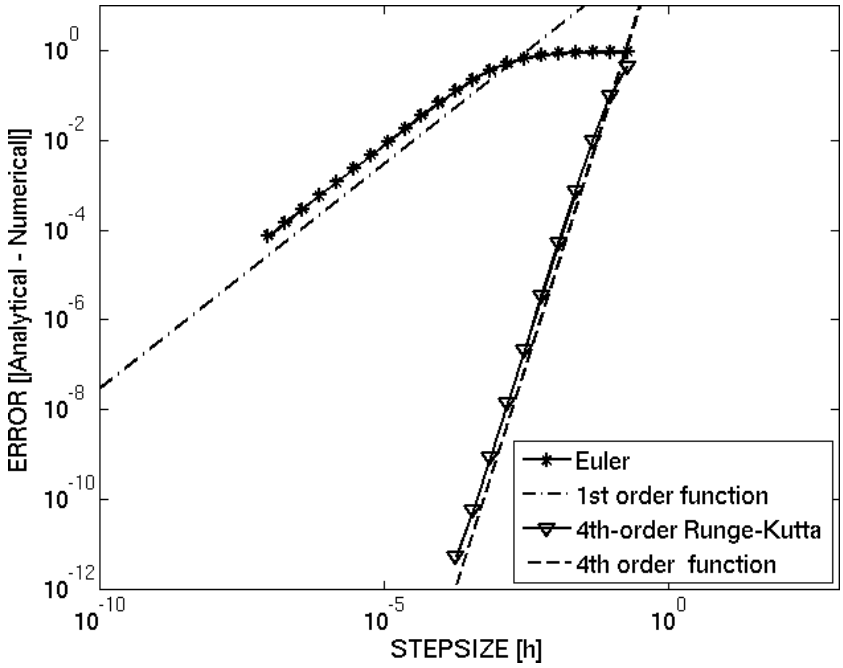

Figure 4.2: Scaling of error with stepsize for Euler's and fourth-order Runge-Kutta methods

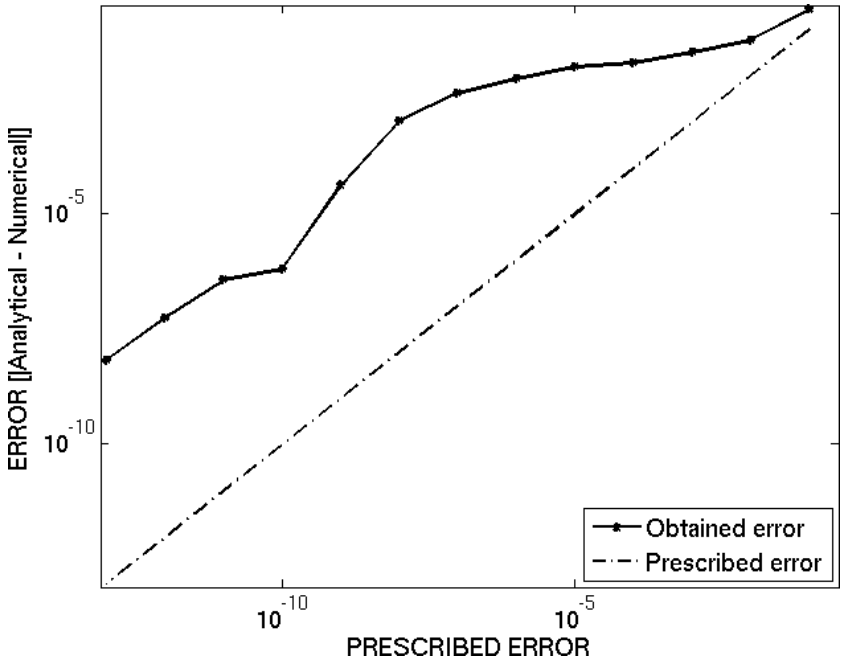

Figure 4.3: Correspondence between prescribed and achieved error for RK45 method

4.0.6 Application of ODE-solvers to a 1D problem

A simple one-dimensional problem with a known analytical solution is solved using the outlined ODE-solvers, to ensure that the error behaves as predicted. For Euler's and Fourth-order Runge-Kutta methods, the scaling of the error with stepsize is investigated and expected to be first- and fourth-order, respectively. For the RK45 method, it is investigated wether the prescribed error tolerance is, in fact, achieved. The calculated error is given by the difference between the analytical and numerical solutions.
The problem we wish to solve is as following:

$$\frac{\partial y}{\partial x} = -200xy^2 \tag{4.13}$$

with initial conditions given by:

$$\begin{aligned} x_0 &= -3 \\ x_f &= 0 \\ y(x_0) &= \frac{1}{901} \end{aligned} \tag{4.14}$$

The value of y at the end of the interval is found analytically using separation of variables, and the result is:

$$y(x_f) = 1 \tag{4.15}$$

The numerically calculated value of y at the end of the interval is compared to $y(x_f)$ to obtain the error.
Equation 4.13 was solved using Euler's and the Fourth-order Runge-Kutta methods with different stepsizes. The resulted error was plotted against stepsize and the scaling was compared to first- and fourth-order functions. The results are presented in Figure 4.2. It may be observed that Euler's method is highly inaccurate and achieves the first-order scaling only for very small stepsizes. Error resulting from the Fourth-order Runge-Kutta method satisfies the prescribed fourth-order scaling.
Solving Equation 4.13 with the RK45 method, using the inbuilt MATLAB function 'ode45', we varied absolute and relative tolerances, while keeping $rtol = atol$. Correspondence between the prescribed and achieved errors was calculated by comparing the value given by equation 4.12 with difference between analytical and numerical solutions. The results are presented in Figure 4.3.

4.0.7 Application of ODE-solvers to a 2D problem

The 2D test-model consists of a marker with some given initial position, $\vec{x}(t)$, advecting in a shear cell setup. The constant in time velocity field $\vec{V} = (V_x, V_y)$ is given by Equation 4.16:

$$\begin{aligned} V_x &= |\vec{V}| cos(\frac{\pi}{2}\frac{x}{L_x}) sin(\frac{\pi}{2}\frac{y}{L_y}) \\ V_y &= -|\vec{V}| sin(\frac{\pi}{2}\frac{x}{L_x}) cos(\frac{\pi}{2}\frac{y}{L_y}) \end{aligned} \tag{4.16}$$

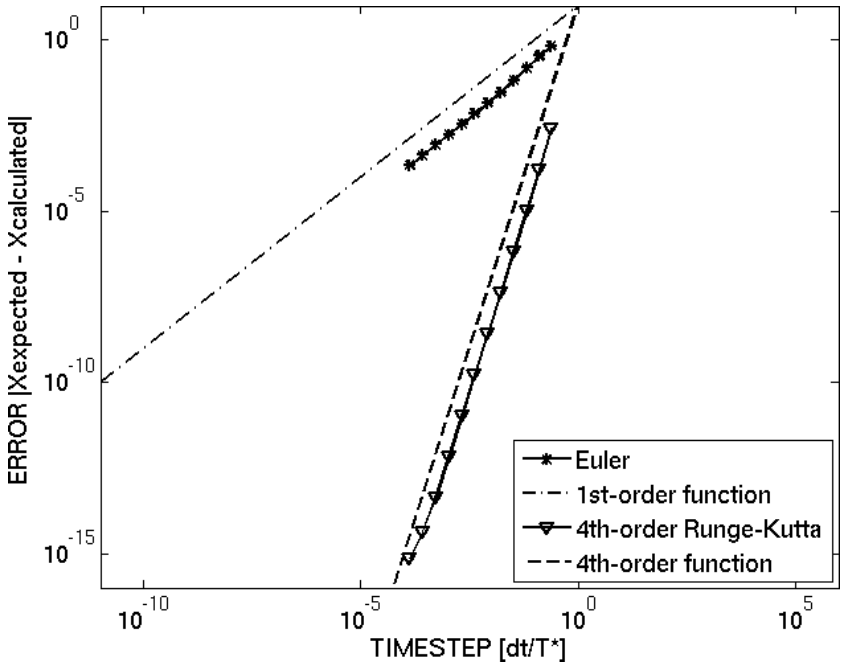

Figure 4.4: Scaling of error with stepsize for Euler and fourth-order Runge-Kutta methods

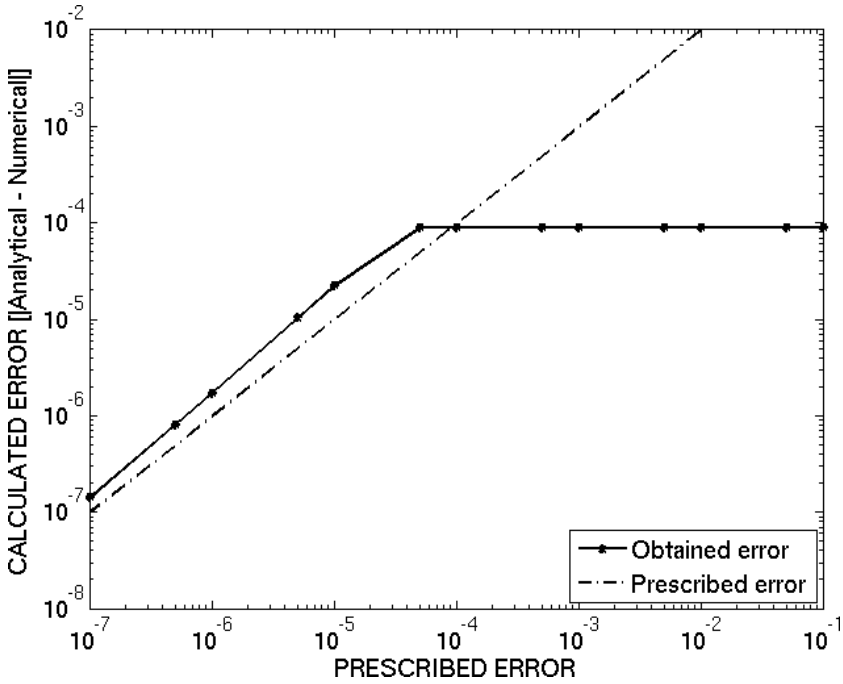

Figure 4.5: Correspondence between prescribed and achieved error for RK45 method

where $2L_x$ and $2L_y$ are the horizontal and vertical sizes of the domain, respectively. To shorten the notation, we define $a = \frac{\pi}{2L_x}$ and $b = \frac{\pi}{2L_y}$. Streamlines of this velocity field constitute marker-trajectories. By definition, streamlines are instantaneously parallel to the velocity field, which allows to express them as functions of spatial coordinates. Defining a position vector:

$$\begin{aligned} \vec{r} &= x(t)\hat{i} + y(t)\hat{j} \\ d\vec{r} &= dx\hat{i} + dy\hat{j} \end{aligned} \tag{4.17}$$

where $\hat{i}$ and $\hat{j}$ are unit vectors in x- and y-directions, respectively, streamlines may be derived as following:

$$\begin{aligned} \vec{V} \times d\vec{r} &= 0 \\ V_x dy &= V_y dx \\ cos(ax)sin(by)dy &= -cos(by)sin(ax)dx \\ \int tan(by)dy &= -\int tan(ax)dx \\ -\frac{1}{b}ln(cos(by)) &= \frac{1}{a}ln(cos(ax)) + C_1 \\ \frac{1}{cos^{a/b}(by)} &= cos(ax)e^{C_1} \\ cos(ax)cos^{a/b}(by) &= C \end{aligned}$$

where C_1 and C are constants. The resulting streamlines are closed curves, symmetric about x- and y-axes and centered at origo, that are more circular closer to origo and the form of rectangles closer to the boundaries of the domain. Followingly, each streamline crosses the y-axes in two points and we can uniquely define a streamline by defining an x-position at which one of the y-axes intersections occurs. We define this crossing point as $(x = x_0, y = 0)$, which results in following expression for a streamline in the velocity field given by Equation 4.16:

$$\begin{aligned} cos(ax_0) &= C \\ cos(ax)cos^{a/b}(by) &= cos(ax_0) \end{aligned} \tag{4.18}$$

The time it takes for a particle to travel one cycle along its trajectory may be found using the theory of elliptic integrals. This task is further simplified by the symmetry of the streamlines, since we only need to integrate over a quarter of the entire trajectory. It is convenient to choose the quarter that goes from $x = 0$ to $x = x_0$, where the latter is the x-coordinate of the crossing point, as defined earlier. The time it takes to travel quarter of

the trajectory is given by the following integral:

$$\begin{aligned} I_{time} &= \int_0^{x_0} \sqrt{\frac{1+(\frac{dy}{dx})^2}{V_x^2+V_y^2}}dx \\ &= \int_0^{x_0} \frac{dx}{V_x} \\ &= \int_0^{x_0} \frac{dx}{cos(ax)sin(by)} \\ &= \int_0^{x_0} \frac{dx}{\sqrt{cos^2(ax)-cos^2(ax)cos^2(by)}} \end{aligned}$$

Recognizing the expression for streamline from Equation 4.18, for a case when $a = b$, we may rewrite I_{time} as following:

$$\begin{aligned} I_{time} &= \int_0^{x_0} \frac{dx}{\sqrt{cos^2(ax)-cos^2(ax_0)}} \\ &= \int_0^{x_0} \frac{dx}{\sqrt{sin^2(ax_0)-sin^2(ax)}} \\ &= \frac{1}{sin(ax_0)} \int_0^{x_0} \frac{dx}{\sqrt{1-(\frac{1}{sin(ax_0)})^2 sin^2(ax)}} \end{aligned} \tag{4.19}$$

Equation 4.19 may be expressed in form of a complete elliptic integral of the first kind, $K(k)$, which equals the quarter period of an elliptic function with eccentricity k:

$$K(k) = \int_0^1 \frac{dt}{\sqrt{(1-t^2)(1-k^2t^2)}}, \quad 0 \le k \le 1 \tag{4.20}$$

Using following substitution:

$$\begin{aligned} w &= \frac{sin(ax)}{sin(ax_0)} \\ dx &= \frac{dw}{a\sqrt{(\frac{1}{sin(ax_0)})^2 - w^2}} \end{aligned}$$

Equation 4.19 may be rewritten as:

$$\begin{aligned} I_{time} &= \frac{1}{asin(ax_0)} \int_0^1 \frac{dw}{\sqrt{((\frac{1}{sin(ax_0)})^2 - w^2)(1-w^2)}} \\ &= \frac{1}{a} \int_0^1 \frac{dw}{\sqrt{(1-w^2)(1-sin^2(ax_0)w^2)}} \end{aligned} \tag{4.21}$$

Equation 4.21 may be solved numerically using an inbuilt MATLAB-function 'ellipke(M)', where M is the squared eccentricity $M = k^2$.
After completing one cycle of its trajectory, the marker should return to its starting position. Whether this is actually the case when the marker-trajectory is computed numerically, gives an estimate of the global error produced by the ODE-solver. Scaling of the error resulting from advecting a marker one full cycle, using Euler's and the Fourth-order Runge-Kutta methods with different timesteps, is presented in Figure 4.2. It may be observed that Euler's method still has first-order scaling in two dimensions and the Fourth-order Runge-Kutta method still has fourth-order scaling. This result was found to be independent of the starting position. Using RK45 method to advect the marker, we varied absolute and relative tolerances, while keeping $rtol = atol$. Correspondence between the prescribed and achieved errors was calculated and the results are presented in Figure 4.5. It may be observed that the achieved error satisfies well the prescribed one for tolerances lower than 10^{-4}. The difference between prescribed and achieved errors grows for higher tolerance values.

Chapter 5

Benchmarking of the thermomechanical code

5.1 Description of the physical model

To benchmark the devised thermomechanical FEM code, we apply it to model convection in a rectangular domain. The modelled fluid is isoviscous and homogeneous. It is confined in an impermeable box and is heated from below, with no internal heating. The geometry of the model is presented in Figure 5.1. We assume that we have an infinite Prandtl number fluid with Newtonian rheology and that the Boussinesq approximation applies. The nondimensional form of the governing equations is as following:

$$\begin{aligned} \frac{\partial u_i}{\partial x_i} &= 0 && \text{Mass conservation} \\ 0 = -\frac{\partial p}{\partial x_i} - \bar{g}_i T Ra + \frac{\partial}{\partial x_j}\Big[\mu\Big(\frac{\partial u_i}{\partial x_j} + \frac{\partial u_j}{\partial x_i}\Big)\Big] &&\text{Momentum conservation} \\ \frac{DT}{Dt} &= \frac{\partial}{\partial x_i}\Big(\bar{\kappa}\frac{\partial T}{\partial x_i}\Big) && \text{Energy conservation} \end{aligned} \tag{5.1}$$

Heat transport is modelled using the diffusion and advection solvers that were presented in detail in the preceding chapters. The mechanical solver MILAMIN (Dabrowski et al., 2008) is utilized for solving the Stokes equation.

5.2 Description of the numerical model

5.2.1 Initial and boundary conditions

The rectangular domain is discretized using a structured grid consisting of quadratic elements. The nodes of the grid that do not have a boundary value prescribed to them are

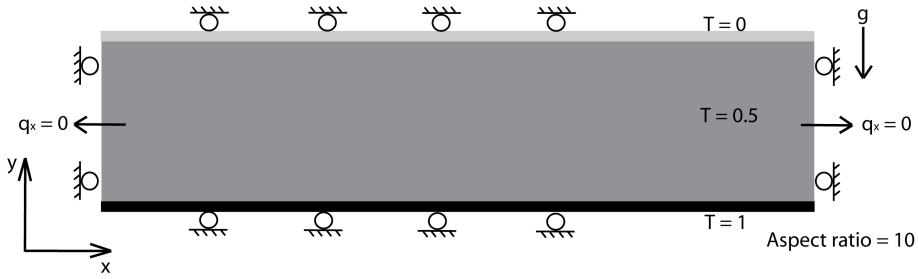

Figure 5.1: Initial and boundary conditions of the model for simulating thermomechanical convection in a rectangular domain.

referred to as free nodes. The approximate solution is obtained for all the free nodes by solving the discretized governing equations. In order to find a solution, the initial and boundary conditions must be specified.
The mechanical boundary conditions are free slip. This implies that the normal velocity component is equal to zero at the boundary, known as the no-penetration condition, and that the tangential component of the traction is zero along the boundary. The free slip boundary conditions can be formulated as following:

$$\begin{aligned} v_n &= \vec{v} \cdot \vec{n} = 0 \\ t_s &= \frac{1}{2}\Big(\frac{\partial v_s}{\partial x_n} + \frac{\partial v_n}{\partial x_s}\Big) = 0 \end{aligned} \tag{5.2}$$

where $\vec{n}$ is the unit vector normal to the boundary, and x_n and x_s are spatial coordinates that are normal and tangential to the boundary, respectively.
The thermal boundary conditions are given by constant temperatures at the top and bottom surfaces and zero heat flux across the lateral boundaries. This is formulated as following:

$$\begin{aligned} T\Big|_{x,y=y_T} &= 0 \quad \text{Top surface} \\ T\Big|_{x,y=y_B} &= 1 \quad \text{Bottom surface} \\ \frac{\partial T}{\partial x}\Big|_{x=x_L,y} &= 0 \quad \text{Left surface} \\ \frac{\partial T}{\partial x}\Big|_{x=x_R,y} &= 0 \quad \text{Right surface} \end{aligned} \tag{5.3}$$

The initial temperature profile is given by $T_B = 1$ and $T_T = 0$ at the bottom and top boundaries, respectively, and in the interior we have the mean temperature $T_I = \frac{T_T+T_B}{2} = 0.5$. The intial thermal conditions vary with the grid resolution. This is because the temperature is prescribed in the nodes and interpolated in the interior of the element. Coarser grid implies a larger distance between the nodes, and interpolating temperature between them results in a smaller gradient than for a finer grid. This is illustrated for a

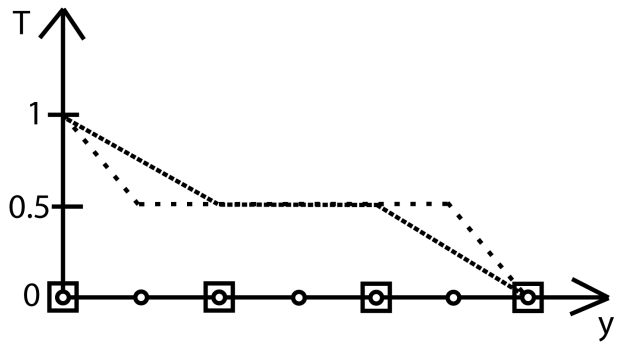

Figure 5.2: Illustration of the resolution-dependence of the intial temperature distribution. A smaller temperature gradient at the boundaries may be observed for the coarser resolution (nodes marked with squares) than for the finer resolution (nodes marked with circles).

one-dimensional grid with linear interpolation between the nodes in Figure 5.2.
The initial and boundary conditions for our model are illustrated in Figure 5.1. We study the evolution of the convective pattern and the Nusselt number with time for different grid and time resolutions. The Nusselt number is given by:

$$Nu = \frac{(y_T - y_B)\bar{q}_y}{k(T_T - T_B)} \tag{5.4}$$

where $\bar{q_y}$ is the horizonally averaged heat flux in y-direction, and k is the thermal conductivity of the fluid.

5.2.2 Advection-diffusion equation

The thermal energy conservation equation describes the advective and conductive heat transport in the system. Assuming no internal heat generation, neglecting heating due to viscous dissipation, and dropping the primes for shortness of notation, the energy equation may be expressed as following:

$$\frac{\partial T}{\partial t} = \frac{\partial}{\partial x_i}\Big(\bar{k}\frac{\partial T}{\partial x_i}\Big) - u_i\frac{\partial T}{\partial x_i} \quad \text{Energy conservation, no internal heating} \tag{5.5}$$

We use operator splitting to model the two heat transport mechanisms separately. In the first half of the time step, we update the temperature according to the conductive heat transport, assuming no advection. This is done by numerical solution of the following equation:

$$\frac{\partial T}{\partial t}\Big|_{[t_0, t_0+\frac{1}{2}\triangle t]} = \frac{\partial}{\partial x_i}\Big(\bar{k}\frac{\partial T}{\partial x_i}\Big) \quad \text{Diffusion} \tag{5.6}$$

where t_0 is the time at the beginning of the time interval. The method for numerical solution of the Equation 5.6 was described in the chapter about the FEM diffusion solver. In the

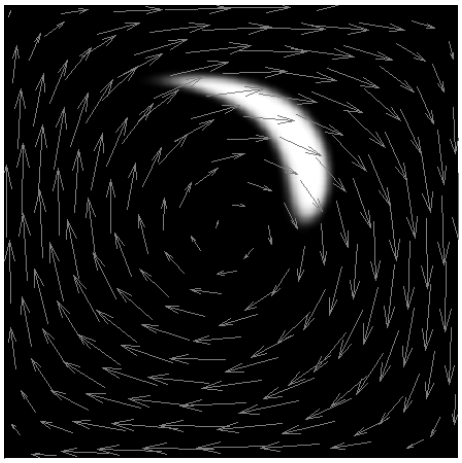

Figure 5.3: An example of temperature distribution after a total time of $2[\frac{w}{max|V|}]$ for the model that is used to study numerical diffusion of the method of shooting back characteristics. The background has temperature equal to zero, and the sheared disk has temperature equal to one.

second half of the time step, we model the convective heat transport, assuming no diffusion. This is done by numerical solution of the following equation:

$$\frac{\partial T}{\partial t}\Big|_{[t_0+\frac{1}{2}\triangle t, t_0+\triangle t]} = -u_i \frac{\partial T}{\partial x_i} \quad \text{Advection} \tag{5.7}$$

To solve the Equation 5.7 numerically, we use the method of shooting back characteristics. This method is based on the fact that the temperature doesn't change along the characteristic lines that follow the flow (Baptista, 1987). We first calculate the positions of the current temperature values one timestep ago, by tracking back characteristics. The fourth-order Runge-Kutta method is used to perform this step, with mechanical shape functions used to interpolate velocities at the intermediate positions. Then we interpolate the temperature values in nodes onto the feet of characteristic lines, using thermal shape functions. The temperature values in thermal nodes are then set equal to the temperature values at the feet of characteristics.

5.2.3 Numerical Diffusion

Interpolating temperature values from thermal nodes to the feet of characteristics during modelling of the advective heat transport, introduces a numerical error, commonly referred to as numerical diffusion. To study the effect of numerical diffusion when using the method of shooting back characteristics, we apply this method to model advection of a hot disc in cold environment in a shear cell setup. The dimensionless width of the cell is $w = 1$, with aspect ratio 1. The radius of the hot disc is $r = \frac{1}{10}w$. We set the diffusion constant equal

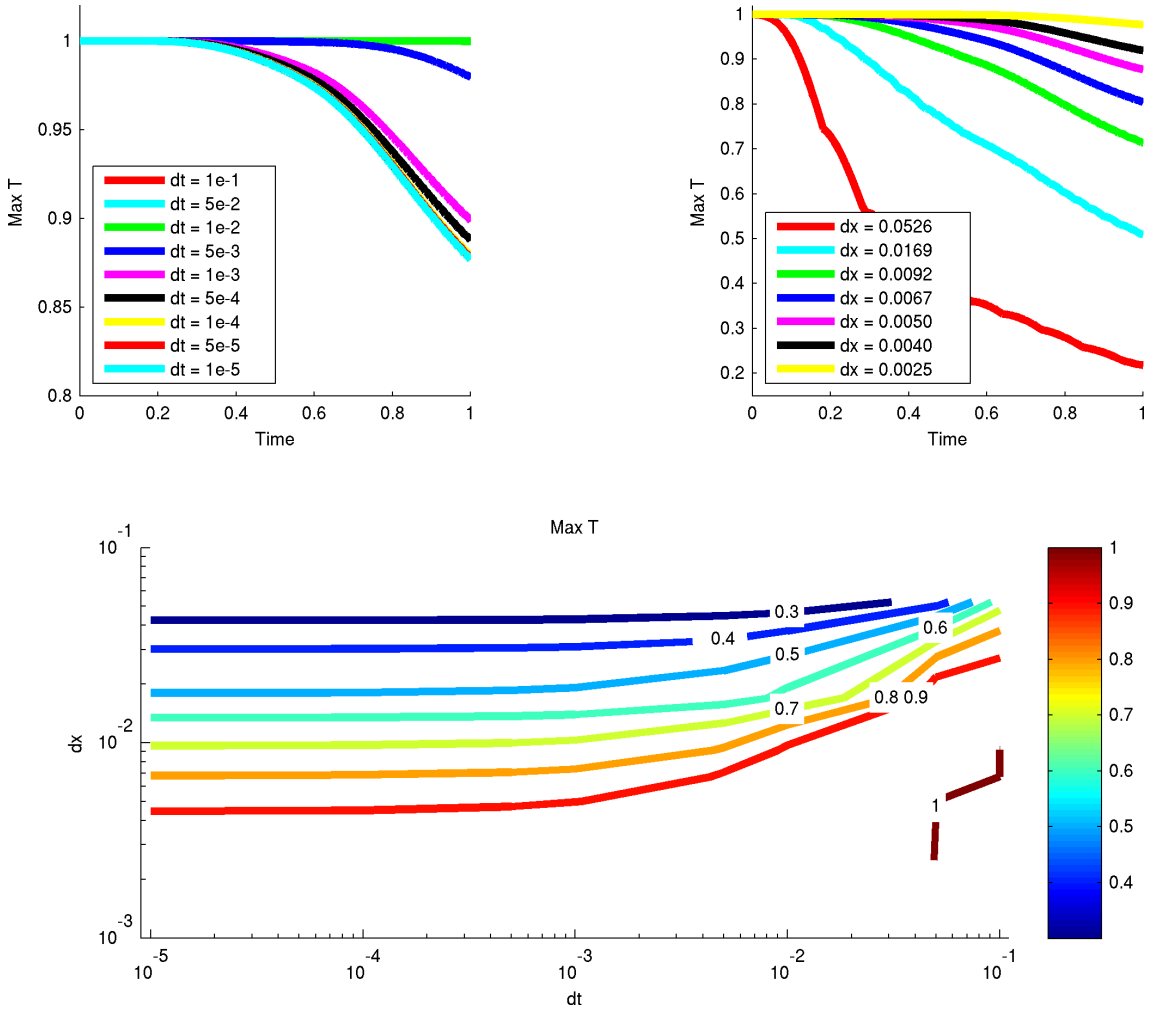

Figure 5.4: Maximum temperature monitored throughout the simulation of a hot disk advecting in a shear cell setup. Temperature decay is only due to the numerical diffusion, since the physical diffusion is turned off by setting the thermal diffusivity equal to zero. Results for different space- and time-resolutions are presented. The spatial resolution used for the plot on the left is $dx = 5 \cdot 10^{-2}[w]$. The timestep used for the plot on the right is $\triangle t = 1 \cdot 10^{-5}[\frac{w}{max|V|}]$. The contours of the maximum temperature at the end of each simulation, as a function of dx and dt, is presented in the bottom figure.

to zero, so that any temperature decay in the system can be directly related to numerical diffusion. An example of temperature distribution after a total time of $2[\frac{w}{max|V|}]$ is presented in Figure 5.3.
We monitor the maximum temperature of the system as it evolves through time. Different time- and space-resolutions are tested, with the time of simulation being the same for all configurations. The results are presented in Figure 5.4. We observe that for a given grid resolution, the numerical diffusion is higher for smaller timesteps. This is an expected result, since smaller timestep sizes require a larger number of timesteps to reach the same simulation time, and hence the number of interpolations of temperature is also larger, leading to more numerical diffusion. We also observe that the amount of numerical diffusion saturates, and refining the timestep to values smaller than around $1 \cdot 10^{-4}$ doesn't change the effect of numerical diffusion. Refining the grid resolution for a given timestep leads to less numerical diffusion. This is also an expected result, since the interpolation is more accurate when we have more nodes in the system. The maximum temperature values at the end of simulations preformed for the different timestep and grid sizes are also presented in Figure 5.4. The two-dimensional contour plot shows that the numerical diffusion saturates, such that for small enough timesteps, decreasing the timestep size doesn't lead to more numerical diffusion.

5.2.4 Computational time

We study how the computational time required by the different parts of our code varies with grid resolution. The parts of the code that we study are (i) assembling and factorization of global matrices entering the Stokes solver, (ii) factorization of the global matrices entering the thermal solver, (iii) evaluation of the right hand side (RHS) of the Stokes solver, (iv) Uzawa iterations to compute velocity field, (v) computing temperature field with thermal solver, and (vi) advecting the temperature field using characteristics and the fourth-order Runge-Kutta method. We introduce two independent grids for computing velocity and temperature, called mechanical and thermal grids, respectively. This allows us to independently increase the resolution for the temperature field, without affecting the time of computation of the mechanical field.
The scaling of the computational time as we refine the mechanical grid, while keeping the number of thermal per mehanical elements constant, is presented in Figure 5.5. We also study the dependence of the computation time on the number of thermal per mechanical elements. We present the results for two different mechanical grid resolutions, with 50 and 100 mechanical elements in vertical direction, with the number of thermal per mechanical elements varying from 1x1 to 3x3 in Figure 5.6. We observe that for a given mechanical grid resolution, the number of thermal per mechanical elements may be increased up to 2x2 without significantly affecting the total time of simulation.
The thermal and mechanical grid resolutions are chosen depending on how frequently the different parts of the code need to be used. For an isoviscous homogeneous material, the assembling and factorization of global matrices entering the Stokes solver and the ones entering the thermal solver only need to be evaluated once, outside the time loop. As we refine

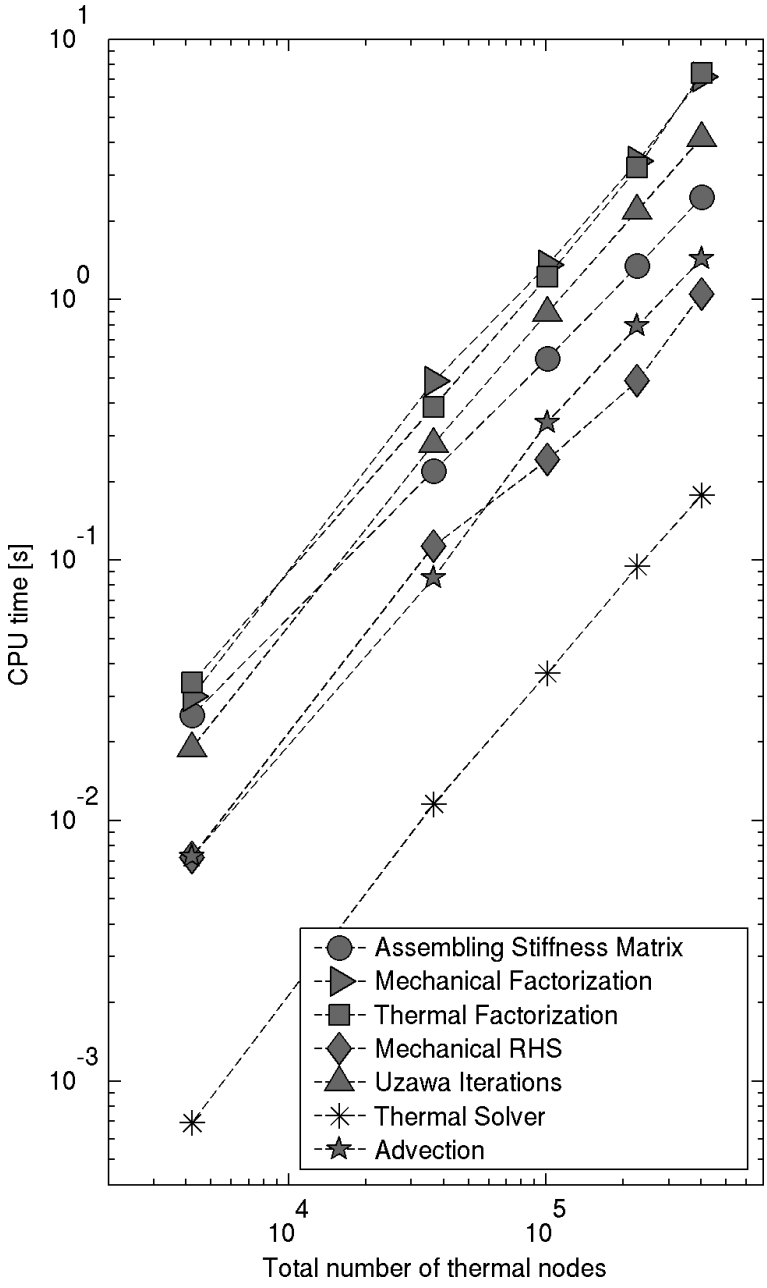

Figure 5.5: Computational time spent by individual components of the thermomechanical FEM code. Results for different total numbers of thermal nodes are presented. The total number of thermal nodes is determined by the number of mechanical elements, varying from 10 to 100 in vertical direction in this case, and the number of thermal per mechanical elements, 2x2 in this case.

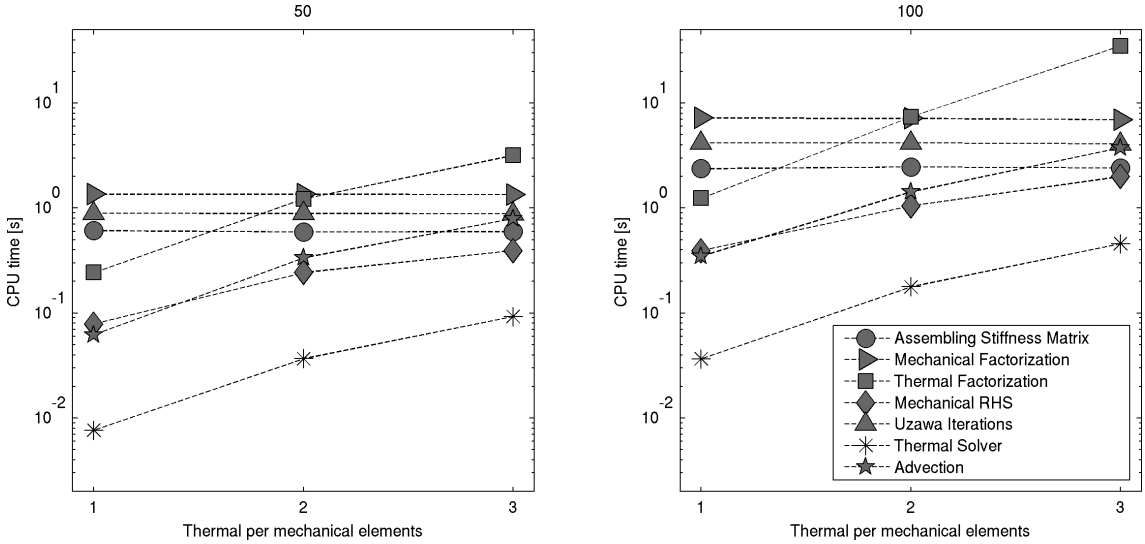

Figure 5.6: Computational time spent by individual components of the thermomechanical FEM code. Results for different numbers of mechanical elements in vertical direction are presented: 50 on the left and 100 on the right. The number of thermal per mechanical elements varies from 1x1 to 3x3.

the thermal grid for such systems, while keeping the mechanical grid resolution the same, the advection step becomes the limiting factor of how much we gain from independently refining the thermal grid resolution, in terms of computaional time. If the viscosity, and/or the diffusivity of the system are not constants, then all parts of the thermomechanical code need to be used in order to compute each time step. In that case, the factorization of the thermal matrices poses the limit for how much we gain from refining the thermal grid, while keeping the mechanical grid the same, compared to refining of the mechanical grid.
Using two independent grids for temperature and velocity fields raises the question of whether it is justified, in terms of accuracy, to have a lower resolution for one of these fields. As is presented in the following sections, we obtain higher accuracy of the results in our homogeneous and isoviscous model, by refining the thermal grid up to 5x5 thermal per mechanical elements.

5.2.5 Coupled thermomechanical solver

An example of a mechanical and thermal grids used to discretize the rectangular domain is illustrated in Figure 5.7. We use four-node quads for the elements of the thermal grid and nine-node quads for the elements of the mechanical grid. The mechanical grid resolution is determined by the aspect ratio and the number of mechanical elements in the vertical direction. The thermal grid resolution is determined by the number of thermal elements per mechanical element.

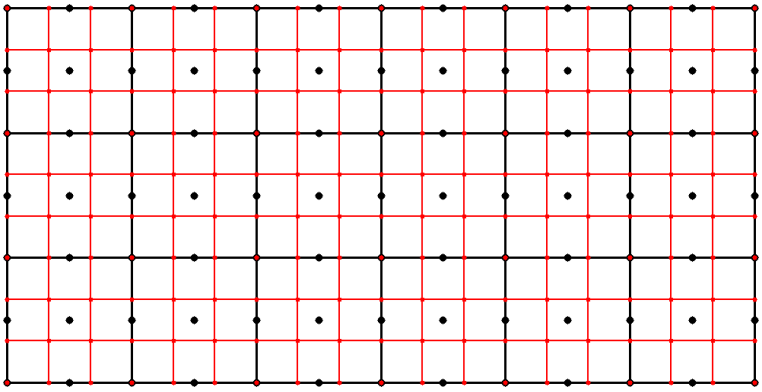

Figure 5.7: The independent thermal (in red) and mechanical (in black) structured grids representing the rectangular domain. Thermal elements are four-node quads and mechanical elements are nine-node quads. The mechanical grid resolution is defined by the aspect ratio, 2 in this case, and the number of mechanical elements in the vertical direction, 3 in this case. The thermal grid resolution is determined by the number of thermal elements per mechanical element, 3^2 in this case.

Once the grid is constructed and the temperature initialized, we start computing the evolution of the system with time. First, the heat diffusion step is performed, where we update the temperature in the nodes according to the result from the diffusion solver. Next, we compute the velocity field in mechanical nodes using MILAMIN. Then, we model the convective heat transport by advecting the temperature with the obtained velocities.
Using independent grids for the velocity and temperature values introduces some additional steps in our algorithm. This involves transfer of information between the two grids. The velocity is calculated based on the density variations that drive convection, which are of thermal origin. Hence, the information about temperature field must be passed to the mechanical grid, or more specifically to the integration points of the mechanical elements.
Using FEM, we solve the weak, or integral, form of the differential equations. The integral of temperature in each element need to be evaluated for the right hand side (RHS) of the Stokes equation. We use Gaussian quadrature to evaluate the integrals numerically. This involves sampling of the integrand in a prescribed number of integration points, which positions are given by the Gaussian integration rule. Hence, we interpolate the temperature values from the thermal grid onto the integration points of the mechanical grid.
During convective heat transport, the temperature field advects with the velocity provided by the mechanical solver. Hence, information about velocity field must be passed to the coordinates along the characteristic lines, as required by the ODE solver. We interpolate the velocity-values using the mechanical shape functions. The algorithm is summarized in the following:

1. Perform the diffusion step
2. Evaluate the right hand side of the Stokes equation, by integrating temperature values

interpolated from the thermal grid

3. Calculate the velocity field using the mechanical solver
4. Advect temperature field using characteristics and the fourth-order Runge-Kutta method.

5.3 Modeling results

5.3.1 Spatial resolution

We monitor the temperature distribution in the system and the Nusselt number at the top boundary. We study the results for different spatial resolutions, varying the mechanical grid from 10 to 100 elements in the vertical direction, and varying the number of thermal elements per mechanical element from 1x1 to 5x5. We present the results obtained with grids consisting of 25 and 100 mechanical elements in vertical direction, for all thermal elements configurations, in Figure 5.8.
We refer to the upwellings and downwellings observed in the figures as plumes. Several qualitative parameters are defined for the purpose of describing the different convective patterns. We choose to look at the number of plumes in the system. This number is influenced by how close the bases of neighboring plumes are positioned, as well as the branching of the plume with one tail feeding several plume heads. We also look at the thickness of the plume tails and the sharpness of the interface between the plume and the interior. The ability of a plume tail to extend all the way from the bottom to the top, or vice versa, is another qualitative parameter we consider. This parameter is influenced by the obliqueness of the tail with respect to the horizontal boundaries, the amount of wiggling of the tail, as well as the amount of smearing along its travel. The last descriptive parameter we define is the number of relatively small disconnected structures present in the interior. Due to the initial random perturbations that we introduce to the system, the convective patern of the same system varies for each simulation. However, we expect the qualitative parameters that we defined for the description of the patterns to be approximately the same for each simulation of the same system.
Studying the temperature distribution in the top five plots of Figure 5.8, we observe that it varies for different thermal grid resolutions. The number of plumes increases for finer thermal grids, both due to narrower spacing between neighbouring plumes and to the increased branching. The plume tails are thicker for coarser resolutions, with more smeared interfaces between the plumes and the interior. In the top plots, which present the coarsest resolution, some of the plume heads are smeared to such extent that only the tails can be identified. In the case of the coarsest resolution, top plot of Figure 5.8, there are no plumes that extend all the way from the top to the bottom, or vice versa, as they appear to be bent away from the opposing horizontal boundary, as well as highly smeared. We see more disconnected structures in the interior of the system for higher resolution cases.

The higher resolution results, with 100 mechanical elements in vertical direction, are presented in the bottom five rows of Figure 5.8. We see that changing the thermal grid resolution in this case doesn't result in as high variation in temperature patterns as was observed for the case of 25 mechanical elements in vertical direction. However, we still observe a larger number of plumes for higher thermal grid resolutions. The tails of the plumes are slightly thicker in the top plot, with coarsest resolution, compared to the bottom four where the thicknesses of the plumes don't vary much. There appears to be more smearing of interfaces between the plumes and the interior in the top plot, compared to the bottom four, where the sharpness of interfaces is quite similar. Nearly all of the plumes in the top plot extend all the way from the top to the bottom, and vice versa, with their tails oriented nearly perpendicular to the horizontal boundaries. The tails of the plumes in the bottom four figures have a large variation in their orientations with respect to the horizontal boundaries, and they also appear to wiggle more. However, these plumes have relatively longer tails and manage to extend all the way from the top to the bottom, and vice versa. No disconnected structures can be observed in the top plot, while several are resolved in the bottom four figures.
In general, we observe that the coarser thermal grids result in more diffuse temperature fields, compared to finer grids, and hence more detailed structures can be observed with higher resolutions. Increasing the resolution of the mechanical grid reveals how unstable the plumes are with respect to the direction of their propagation.
Time evolution of the Nusselt number computed at the top boundary for each grid resolution is presented in Figures 5.9 and 5.10. For the coarse grid of 25 mechanical elements in the vertical direction, we observe that the Nusselt number of the system after it has reached the dynamic equalibrium varies for different thermal grid resolutions. The Nusselt number increases as we refine the thermal grid. In case of the higher mechanical grid resolution, with 100 mechanical elements in the vertical direction, the Nusselt number obtained with different thermal grid resolutions is quite similar. This indicates that the convergence has been reached for these resolutions.
To illustrate how the Nusselt number varies for different grid resolutions, its time-average is plotted against the number of thermal elements in horizontal direction, and presented in Figure 5.11.

5.3.2 Time resolution

In order to test whether the time resolution that is used for the simulations, $\triangle t = 1 \cdot 10^{-6} \frac{b^2}{\kappa}[s]$, is an appropriate one, we vary the timestep size between $\triangle t = 5 \cdot 10^{-7} - 1 \cdot 10^{-5} \frac{b^2}{\kappa}[s]$. Convection patterns obtained after a total time of simulation of $3 \cdot 10^{-3} \frac{b^2}{\kappa}[s]$, with a subsequently refined time resolution, are presented in Figure 5.12. Time evolution of the Nusselt number computed at the top boundary for different time resolutions is presented in Figure 5.13. The similarity of the obtained convective patterns, as well as the Nusselt number after the dynamic steady state is reached, for different time resolutions indicates that the convergence of solution is reached for the timestep that we use in the simulations.

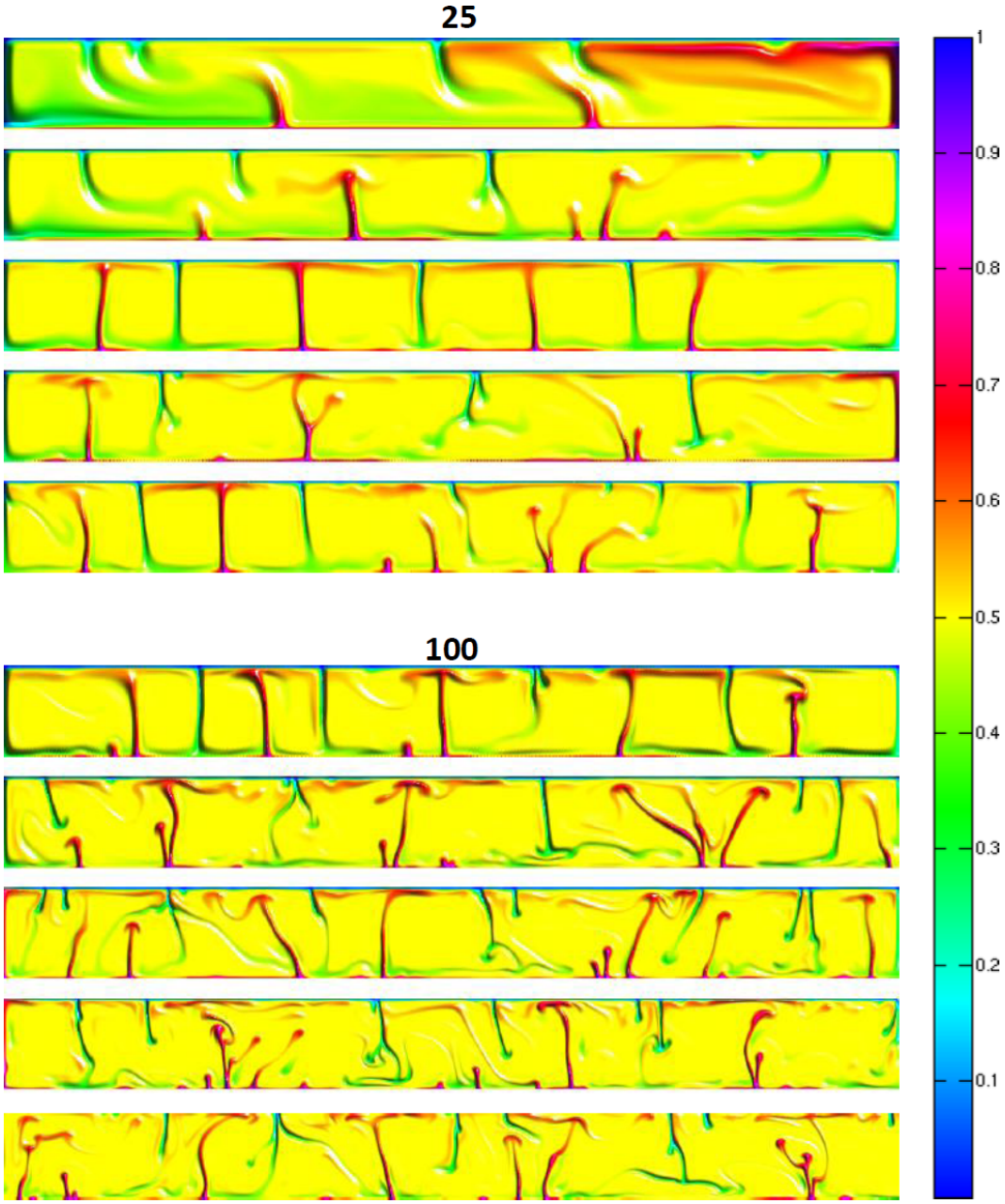

Figure 5.8: Convection pattern after $3 \cdot 10^{-3} \frac{b^2}{\kappa}[s]$. Aspect ratio = 10, number of mechanical elements in the vertical direction is 25 in the top five figures and 100 in the bottom five figures. Number of thermal elements per mechanical element increases downwards for each mechanical resolution: 1,4,9,16,25. The timestep size is $1 \cdot 10^{-6} \frac{b^2}{\kappa}[s]$.

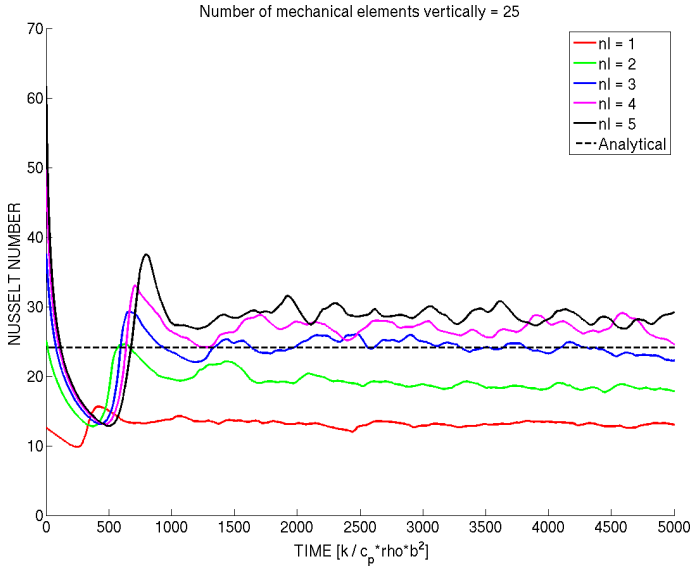

Figure 5.9: Time evolution of the Nusselt number computed at the top boundary for varying thermal grid resolution. In the legend, *nl* denotes number of thermal elements along one side of a mechanical element. Number of mechanical elements in the vertical direction = 25. The timestep size is $1 \cdot 10^{-6} \frac{b^2}{\kappa}[s]$.

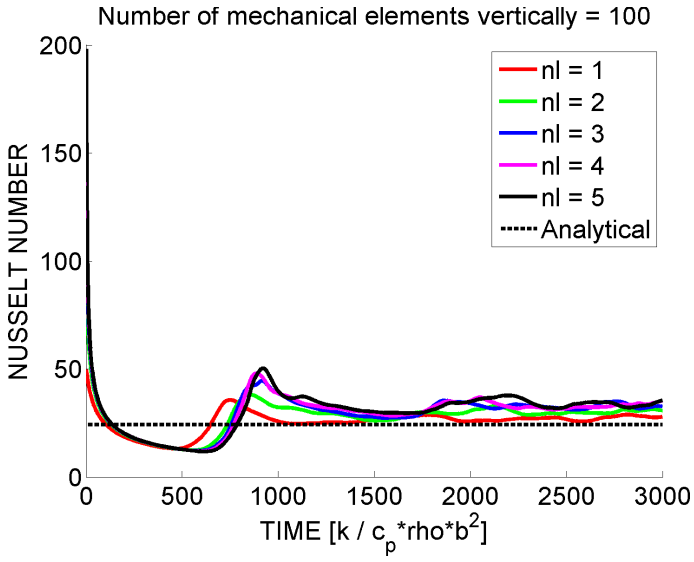

Figure 5.10: Time evolution of the Nusselt number computed at the top boundary for varying thermal grid resolution. In the legend, *nl* denotes number of thermal elements along one side of a mechanical element. Number of mechanical elements in the vertical direction = 100. The timestep size is $1 \cdot 10^{-6} \frac{b^2}{\kappa}[s]$.

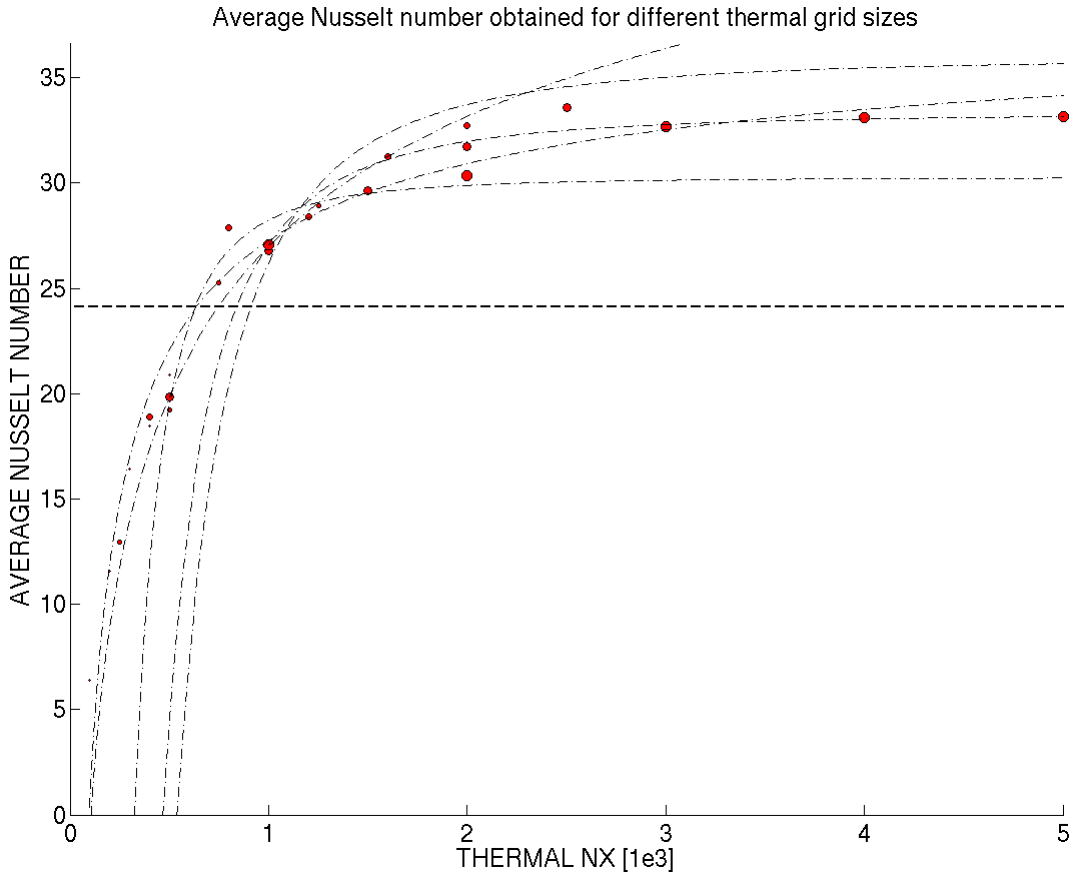

Figure 5.11: Time average of the Nusselt number obtained with different thermal and mechanical grid resolutions. The size of the circular markers represent the grid resolutions. The smallest marker corresponds to the result obtained with 10 mechanical elements in vertical direction and 1 thermal element per mechanical element. The largest marker corresponds to the result obtained with 100 mechanical elements in vertical direction and 25 thermal elements per mechanical element. The Nusselt number according to the boundary layer theory is plotted as a thick black line. Thin dashed lines are the fitted power-law functions. The timestep size is $1 \cdot 10^{-6} \frac{b^2}{\kappa}[s]$. Total time of simulation is $3 \cdot 10^{-3} \frac{b^2}{\kappa}[s]$.

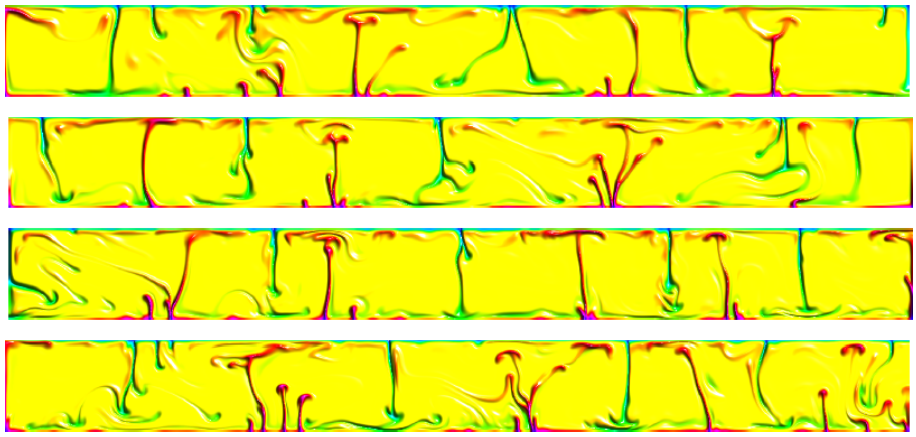

Figure 5.12: Convection pattern after $5 \cdot 10^{-3} \frac{b^2}{\kappa}[s]$. Aspect ratio = 10, number of mechanical elements in the vertical direction = 100, number of thermal elements per mechanical element = 16. The timestep size decreses downwards: $5 \cdot 10^{-7}$, $1 \cdot 10^{-6}$, $5 \cdot 10^{-6}$, $1 \cdot 10^{-5}$ $\frac{b^2}{\kappa}[s]$.

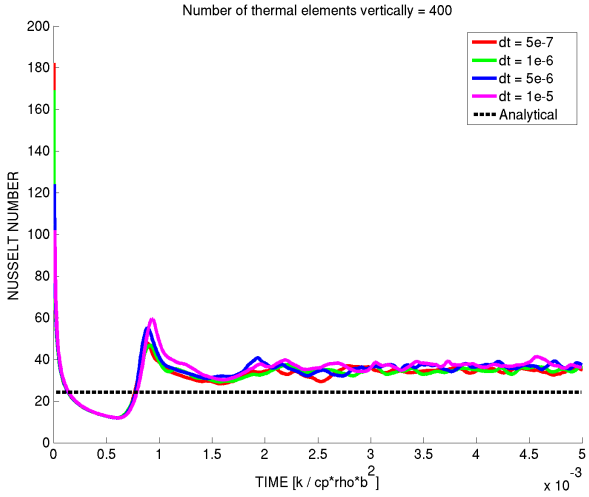

Figure 5.13: Time evolution of the Nusselt number computed at the top boundary for varying time resolutions. The spatial resolution for the presented simulations is determined by the number of mechanical elements in the vertical direction, which is 100, and the number of thermal elements per mechanical element, which is 16. In the legend, dt denotes the stepsize, which dimensional value is given by $dt\frac{b^2}{\kappa}[s]$.

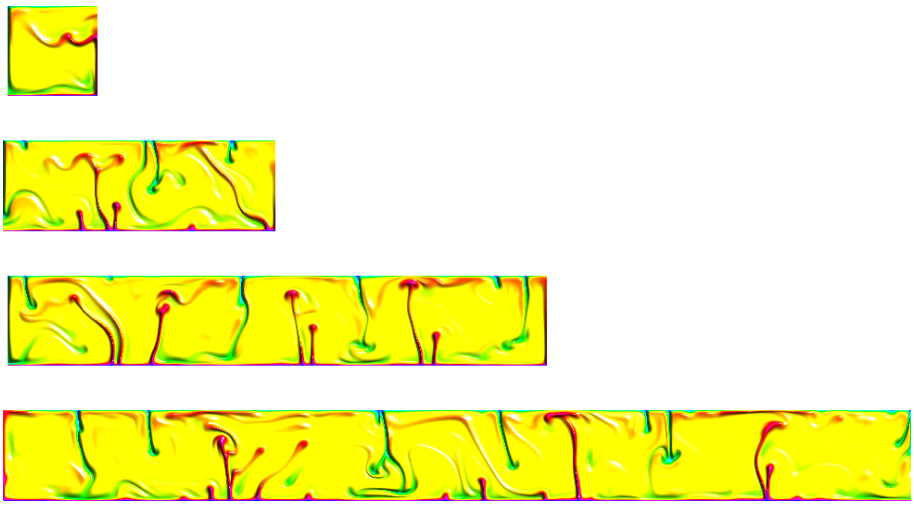

Figure 5.14: Convection pattern after $3 \cdot 10^{-3} \frac{b^2}{\kappa}[s]$. Aspect ratio increases downwards: 1, 3, 6, 10. Number of mechanical elements in the vertical direction = 100, number of thermal elements per mechanical element = 16. The timestep size is $1 \cdot 10^{-6} \frac{b^2}{\kappa}[s]$.

5.3.3 Aspect ratio

It is interesting to study how the presence of lateral boundaries affects the numerically calculated Nusselt number. The effect of the boundaries poses a constraint when we wish to compare the numerical solution with the analytical prediction for an infinitely long layer, provided by the thermal boundary layer theory. The effects of the boundaries is studied by varying the aspect ratio from 1 to 10. Convection patterns obtained after a total time of simulation of $3 \cdot 10^{-3} \frac{b^2}{\kappa}[s]$ for different aspect ratios are presented in Figure 5.14. Time evolution of the Nusselt number computed at the top boundary for different aspect ratios is presented in Figure 5.15. For different aspect ratios, we observe similar convective patterns and Nusselt number after the dynamic steady state has been reached. This shows that the aspect ratio doesn't have much influence on our numerical results.

5.3.4 Flow visualization with markers

To visualize the flow, we use passive markers that are initially distributed randomly throughout the domain of our computational model. The markers are divided into three layers, based on their initial vertical positions, and indexed. This way, we can keep track of the layers as they advect with the velocities computed for each time step of the simulation.
Distribution of the markers at four different times are presented in Figures 5.16 for two different resolutions: one with 10 mechanical elements in vertical direction, and the other with 50, respectively. Number of thermal elements per mechanical element is 5x5 in both cases. The timestep size is $1 \cdot 10^{-6} \frac{b^2}{\kappa}[s]$.

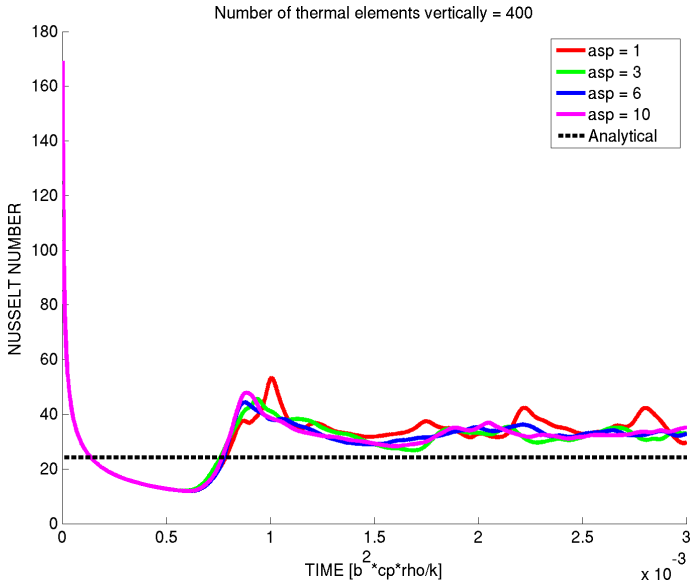

Figure 5.15: Time evolution of the Nusselt number computed at the top boundary for varying aspect ratios, denoted *asp* in the legend. Number of mechanical elements in the vertical direction = 100, number of thermal elements per mechanical element = 16. The timestep size is $1 \cdot 10^{-6} \frac{b^2}{\kappa}[s]$.

In figures presenting the flow patterns after 1000 timesteps, plot number two from top for both mechanical grid resolutions, we observe a periodicity in the structure of the layers. We can identify up to five cells in the coarser grid case, with patches of yellow markers lying on the bottom, separated by the columns of black markers. In the finer grid case, we can identify up to eight cells of yellow markers piled up at the top, and separated by the thin columns of black markers. We use fewer markers to visualize the flow for the coarser resolution, which makes it difficult to compare the flow patterns with those for the high resolution grid at the end of simulation. For the higher resolution grid, a more detailed flow pattern can be observed at the end of the simulation.

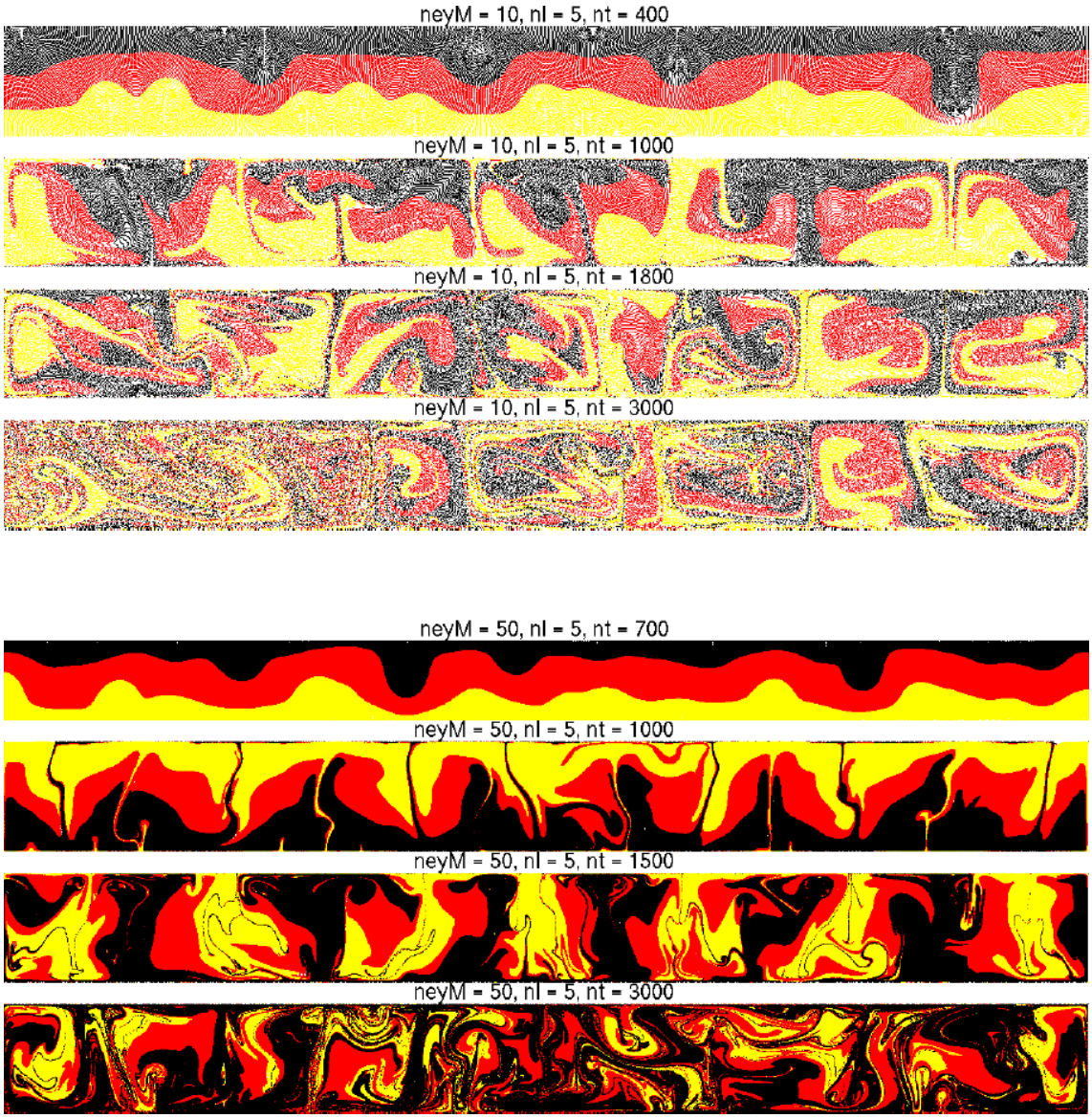

Figure 5.16: Three layers of tracer markers advected with velocities computed during the thermomechanical simulation. Number of mechanical elements in the vertical direction is 10 in the top five figures and 50 in the bottom five figures. The number of thermal elements per mechanical element is 5x5 in all figures. Results for four different timesteps are presented for each resolution. The timestep size is $1 \cdot 10^{-6} \frac{b^2}{\kappa} [s]$.

Chapter 6

Dense basal layer

6.1 Description of the physical model

We apply the developed thermomechanical FEM code to model convection of a fluid comprised by two chemically distinct materials with temperature-dependent viscosity in a rectangular domain. The fluid is confined in an impermeable box and is heated from below, with no internal heating. We assume that we have an infinite Prandtl number fluid with Newtonian rheology and that the Boussinesq approximation applies. The nondimensional form of the governing equations is as following:

$$\begin{aligned} \frac{\partial u_i}{\partial x_i} &= 0 \quad \text{Mass conservation} \\ 0 = -\frac{\partial p}{\partial x_i} - \bar{g}_i T Ra_1 + \frac{\partial}{\partial x_j}\Big[\mu\Big(\frac{\partial u_i}{\partial x_j} + \frac{\partial u_j}{\partial x_i}\Big)\Big] &\quad \text{Momentum conservation} \\ \frac{DT}{Dt} = \frac{\partial}{\partial x_i}\Big(\bar{\kappa}\frac{\partial T}{\partial x_i}\Big) &\quad \text{Energy conservation} \end{aligned} \tag{6.1}$$

where Ra_1 is the Rayleigh number evaluated at the bottom boundary.
The fluid is comprised by two chemically distinct materials: a dense layer along the bottom boundary overlain by a material of lower density and higher viscosity. Density and viscosity of the entire fluid are both temperature- and chemistry-dependent. Density variations are expressed as a linear combination of thermal and chemical contributions:

$$\triangle\rho = \triangle\rho_{th} + \triangle\rho_{ch} = \rho_1^1 \alpha \triangle T + (\rho_1^1 - \rho_1^2)\Phi \quad \text{Density variation} \tag{6.2}$$

where ρ_1^1 and ρ_1^2 are the densities of the ambient material and the dense layer, respectively, evaluated at temperature T_1 at the bottom boundary. Φ is a binary phase function that takes on value 0 for the ambient material and 1 for the dense layer. The density difference between the two materials is determined by the buoyancy number $B_r = \frac{\triangle\rho_{ch}}{\triangle\rho_{th}}$.

Viscosity depends on temperature exponentially. Chemical viscosity variations are applied through a scaling parameter q_i that varies for different materials:

$$\mu = q_i \exp\Big(- \theta(T - T_1)\Big) \quad \text{Viscosity variation} \tag{6.3}$$

The dimensionless parameter θ determines the viscosity ratio and is given by:

$$\theta \equiv ln\Big(\frac{\mu_0}{\mu_1}\Big) \tag{6.4}$$

where $\mu_0 = \mu(T_0)$ and $\mu_1 = \mu(T_1)$ are the viscosity values of the ambient material at temperatures at the top and bottom boundaries, respectively. In this model we scale the viscosity with μ_1 for nondimensionalization. q_i is a dimensionless parameter used to scale the viscosity value depending on the chemistry of the material.

6.2 Description of the numerical model

Heat transport is modelled using the diffusion and advection solvers that were presented in detail in the preceding chapters. Material transport is modeled using marker-in-cell technique, discussed in the following sections. The mechanical solver MILAMIN (Dabrowski et al., 2008) is utilized for solving the Stokes equation.

6.2.1 Spatial discretization

We use structured rectangular elements for spatial discretization. To reduce the computational cost, two independent grids, thermal and mechanical, are introduced, as was motivated and described in the preceding chapter. We use four-node quads for the elements of the thermal grid and nine-node quads for the elements of the mechanical grid. The aspect ratio of the rectangular domain is 4.
The nodes of the grid that do not have a boundary value prescribed to them are referred to as free nodes. The approximate solution is obtained for all the free nodes by solving the discretized form of the governing equations, including the equation describing the chemistry- and temperature-dependence of viscosity. In order to find a solution, the initial and boundary conditions must be specified.
Mechanical boundary conditions are free slip. The thermal boundary conditions are given by constant temperatures of the bottom and top surfaces, and zero heat flux at lateral boundaries. The intial thermal conditions vary with the grid resolution, as was discussed in the previous chapter.

6.2.2 Materials represented by markers

Different materials in our model are represented by markers. Markers are distributed randomly within each element, and initially there is an equal number of markers in each element. The markers are labelled so that we can keep track of each material throughout the simulation.

Linear least squares for extrapolation

The material-dependent values of density and viscosity must be transferred from markers to integration points of the mechanical elements in order to be integrate the element stiffness matrix.
Assume we have a function ϕ which values are known in all marker-positions. We wish to evaluate this function in the positions of integration points of the mechanical elements. We use the method of least squares to extrapolate ϕ from markers to element nodes, and then use shape functions to interpolate these ϕ-values from nodes to the integration points. First, we find which mechanical element each marker belongs to and find the local coordinates of the markers in their respective elements. We evaluate shape functions using the local coordinates, and store these values in a matrix $\hat{A}_{mark}$. $\hat{A}_{mark}$ has as many rows as there are markers in the element, nm_{el}, and as many columns as there are nodes, and hence shape functions, in each element, $nnod_{el}$. We define ϕ_{nodes}, ϕ_{mark} and ϕ_{ip} to be the values of ϕ evaluated in nodal, markers-, and integration points-positions, respectively.
A linear system of equations must be solved in order to obtain ϕ_{nodes}, but it has no solution, since there are more equations than unknowns. However, we can find a solution that minimizes the square of residual function, $\hat{r}$, given by:

$$\hat{r} = \phi_{mark} - \hat{A}_{mark} * \phi_{nodes} \tag{6.5}$$

According to the method of linear least squares, the solution, $\tilde{\phi}_{nodes}$, that minimizes $|\hat{r}|^2$, is given by:

$$\tilde{\phi}_{nodes} = \left(\hat{A}^T_{mark} * \hat{A}_{mark}\right)^{-1} * \hat{A}^T_{mark} * \phi_{mark} \tag{6.6}$$

Once $\tilde{\phi}_{nodes}$ has been evaluated, we can obtain the approximate values $\tilde{\phi}_{ip}$ by solving:

$$\hat{A}_{phi} * \tilde{\phi}_{nodes} = \tilde{\phi}_{ip} \tag{6.7}$$

where $\hat{A}_{phi}$ is the matrix where shape functions evaluated in local integration coordinates are stored. In order to test the performance of the least squares method, we study the case of a single element. The element contains markers that represent two different materials, referred to as the background material and the inclusions. The materials are distinguished by a binary function ϕ that is prescribed to each marker. We define a reference case with a nine-node element containing $2 \cdot 10^5$ markers. We extrapolate ϕ from markers to nodes

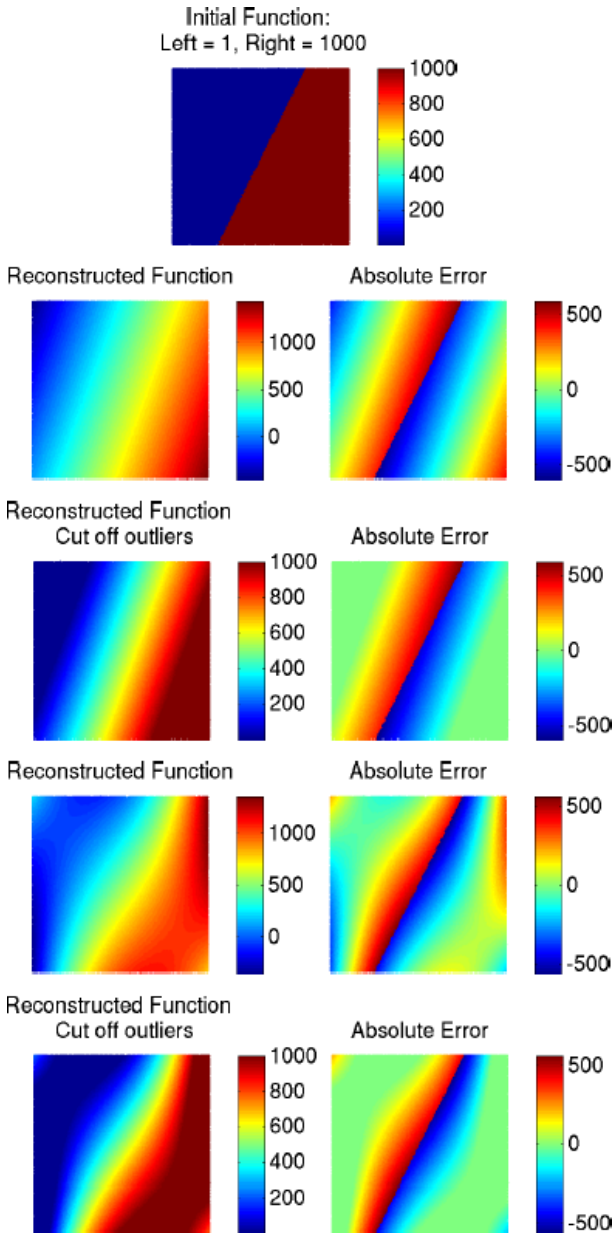

Figure 6.1: Reconstructed function values in the markers after using the least squares method from Equation 6.6. We use $2 \cdot 10^5$ markers distributed randomly throughout the element. *Top:* Initial function values in the markers. *Second row:* Reconstructed function and absolute error for a four-node element. *Third row:* Reconstructed function and absolute error for a four-node element, after cutting off outliers. *Fourth row:* Reconstructed function and absolute error for a nine-node element. *Fifth row:* Reconstructed function and absolute error for a nine-node element, after cutting off outliers.

the least squares method from Equation 6.6, to obtain $\tilde{\phi}_{nodes}$. To evaluate the error, we intepolate $\tilde{\phi}_{nodes}$ back onto markers using shape functions, and compare the recontructed values with the initial ones. The result is presented in the fourth row of Figure 6.1.
We can investigate how the number of nodes in the element influences the result of extrapolation with least squares. We use the same configuration as in the reference case, except for the number of element nodes that is now four instead of nine. The result is presented in the second row of Figure 6.1. We observe that the material distribution is poorer represented in this case compared to the reference case. This can be a combined effect of the error from least squares method during extrapolation, as well as the lower order shape functions that are used for interpolation from nodes back onto markers.
The main source of error in the reconstructed function comes from using the least squares method during extrapolation from markers to nodes. We see in Figure 6.1 that the range of the reconstructed function exceeds the range of the initial function in the markers. This can cause serious artifacts when applying this method to extrapolate density and viscosity values in our thermomechanical model. Namely, we may get unphysical results such as negative density and viscosity values. To avoid the difference in ranges between the initial and the reconstructed functions, we set the reconstructed function values that fall outside the initial range equal to values that define this range. That way, we preserve the well-approximated distribution of the two materials within the element, given by the least squares method, while avoiding values that lie outside the given range. The results are presented in the third and fifth rows of Figure 6.1 for the nine-node and four-node elements. This is the approach we use in our thermomechanical simulation.

6.2.3 Coupled thermomechanical solver

Once the grid is constructed, and temperature and material properties initialized, we start computing evolution of the system with time. The advection-diffusion equation is solved the same way as was done for the homogeneous case, described in Section 5.2.2. Convective transport of material is modelled using the method of shooting back characteristics with the fourth-order Runge-Kutta method.
To compute velocities, we need to evaluate the chemical density contribution to the right hand side of the Stokes equation, as well as the material-dependent factor that scales viscosity which enters the Stokes equation. These material-dependent properties are prescribed in markers. We interpolate the values in markers onto integration points of the mechanical elements using the method of least squares that was presented in Section 6.2.2. Then the velocities are computed by solving the Stokes eqution with MILAMIN.
Next, the heat diffusion step is performed, where we update temperature values in thermal nodes according to the results from the diffusion solver. Then, we model the convective heat transport by interpolating the velocities obtained from the Stokes solver onto the coordinates along the characteristic lines, as required by the ODE solver. We interpolate the velocity-values using the mechanical shape functions. The algorithm for time evolution is summarized in the following:

1. Interpolate the material-dependent contributions of density and viscosity onto integration points of mechanical elements
2. Evaluate the RHS of the Stokes equation in the integration points of the mechanical elements
3. Evaluate the viscosity values in integration points of the mechanical elements
4. Calculate velocities in mechanical grid nodes using Stokes solver
5. Perform the diffusion step and update temperature values in thermal grid nodes
6. Advect temperature values and markers with the velocities obtained from the Stokes solver

6.3 Modeling results

We model the thermomechanical evolution of a fluid comprised by two materials: a dense layer along the bottom boundary overlain by an ambient material of lower density. We study how the temperature field of the system and the distribution of the dense layer vary with time, as well as their dependence on the buoyancy ratio B_r, the viscosity ratio between the two materials $\frac{\mu_1^1}{\mu_1^2}$, and the viscosity ratio due to temperature variations $\frac{\mu_0^1}{\mu_1^1}$. We present results for five different values of the buoyancy ratio, varying from $B_r = 0.1$ to $B_r = 0.5$. Results for three different viscosity ratios are presented: $\frac{\mu_1^1}{\mu_1^2} = 1$, 10, and 1000. Two values of viscosity ratios due to temperature variations are presented: $\frac{\mu_0^1}{\mu_1^1} = 1$ and 10. We investigate how different parameters affect the ability of the dense boundary layer to be swept into thermochemical piles, and the stability and longevity of these piles.

We first study the isoviscous case, where the difference between the two materials is only due to chemical density variations, and there is no viscosity-dependence on temperature or material. In Figure 6.2 the results for the three lowest values of buoyancy ratios are presented: $B_r = 0.1$, 0.2, and 0.3, corresponding to density differences between the dense layer and the ambient material of $\frac{\triangle\rho_{ch}}{\rho_1^1} = 0.42\%$, 0.84%, and 1.26%. The simulation time of the presented models is 500($\pm$50) Ma.

The dense layer in the model with the lowest buoyancy ratio, $B_r = 0.1$, is observed to be gravitationally unstable. It gets more and more entrained into the ambient material with time, and follows the convective flow. The dense layer is also unstable for the buoyancy ratio of $B_r = 0.2$, although there seems to be less entrainment in this case, with larger patches of dense material present in the system, compared to the case with $B_r = 0.1$. Comparing the temperature distribution and the material distribution, we can observe how the cold downwellings of the ambient material sweep the dense layer and shape it into separate domains. The sweeping is even more evident in the model with $B_r = 0.3$. In this case, the dense layer appears to be swept into piles that appear to be more gravitationally stable

than the layers of lower buoyancy ratio. The piles in the $B_r = 0.3$ model have sharp lateral boundaries, and the entrainment of the dense layer into the ambient material appears to be mostly taking place at these boundaries. The convective dynamics within the piles, together with the sweeping by the cold downwellings, determines the shape of the piles.
Time evolution of the isoviscous models with the two highest values of buoyancy ratio are presented in Figures 6.3 and 6.4. In the beginning stage of the simulation, before the cold downwellings reach the bottom, we observe initiation of convection in the dense layer. The hot upwellings are present within the dense layer, but don't rise through the ambient material. The convective dynamics within the dense layer shape its top surface. As cold downwellings of the ambient material reach the layer, they sweep it into separate piles. These piles have sharper boundaries and are higher for the $B_r = 0.4$ model, than for the $B_r = 0.5$ model, which is more flattened. The entrainment of the dense layer into the ambient material is taking place in these two models as well, although not as rapidly as in cases with lower buoyancy ratio. We observe also in these two models that the shape of the piles is dynamically supported by the upwellings within these piles, and is altered by the sweeping of the downwellings.
The spatial resolution that we use for this isoviscous layer is given by 100 mechanical elements in the vertical direction and 3x3 thermal per mechanical elements. We use coarser resolution for the models that are presented in the following, namely 75 mechanical elements in the vertical direction and 2x2 thermal per mechanical elements.
We now introduce additional complexity to our model, by making the two materials differ both in density and viscosity, but still without the temperature-dependence of the viscosity of materials. In Figure 6.5 we present the results of temperature field and dense layer distribution for buoyancy ratios from $B_r = 0.1$ to $B_r = 0.5$ after 428 Ma of simulation time. Models with $B_r = 0.1$ and $B_r = 0.2$ appear not to be stable at all, with the dense layer being well mixed with the ambient material. Comparison of these results with the isoviscous case seems to infer that lower viscosity of the dense layer enhances the entrainment rate. more gravitationally stable structure is observed in the model with $B_r = 0.3$, although significant amount of entrainment into the ambient material is still taking place. We start seeing stable structures of dense material with dynamically supported shapes at buoyancy numbers $B_r = 0.4$ and $B_r = 0.5$. Higher topography of the piles is observed for the $B_r = 0.4$ model, than for the $B_r = 0.5$ model. In the $B_r = 0.4$ model, the piles are more numerous and have smaller lateral extent. The dense material is entrained into the overlying fluid through thin tails that rise from the sides and the top surface of the piles.
We increase the viscosity ratio between the two materials to $\frac{\mu_1^1}{\mu_1^2} = 1000$ and present snapshots of the resulting temperature field and dense layer distribution in Figure 6.6, for buoyancy ratios 0.2, 0.3 and 0.4. Vigorous convection appears to be taking place within the dense layer for this high viscosity contrast. For the model with $B_r = 0.2$ we observe that the layer divides into two large upwellings of dense material that rise along the sides of the rectangular box, and a doming pile of dense material in the center of the domain. Both in the large upwellings and in the doming pile vigorous convection is observed to be taking place. The model evolves into two downwellings and a thin tail of an upwelling comprised

by the dense material, as observed in the second row of Figure 6.6. Vigorous convection is also taking place in the dense layer with $B_r = 0.3$. The convective dynamics within the dense layer shape its topography. The dense material evolves into two large plumes. A thicker one rises along the lateral boundary, and a plume with a thin tail and a large head rises in the center of the domain. We can observe downwellings within the plume head of the dense material. A snapshot of the system after 71.3 Ma of simulation time for the model with $B_r = 0.4$ is presented in the bottom row of Figure 6.6. Vigorous convection that shapes the topography of the dense layer may be observed.

The last set of models that we present have a temperature dependent viscosity and the two materials that only differ in their densities. The viscosity ratio due to temperature variations is $\frac{\mu_0^1}{\mu_1^1} = 10$. We present the results after 428 Ma of simulation time for models with buoyancy ratios from $B_r = 0.2$ to $B_r = 0.5$ in Figure 6.7. Similarly as in the cases when we decreased the viscosity of the dense layer, Figure 6.5, the rate of entrainment of the dense layer into the ambient material increases when we introduce temerature dependence of viscosity. The dense layer in the model with $B_r = 0.2$ is not stable at all, while the model with $B_r = 0.3$ appears to have some stable structure, although most of the layer has been mixed with the ambient material. We observe stable piles of the dense layer in the model with $B_r = 0.4$. The convective dynamics support the topography of these piles. The shape of the piles is also determined by the sweeping by cold downwellings. The piles appear to be lower for the case of the temperature dependent viscosity, compared to the piles in the case of chemically dependent viscosity. For the buoyancy ratio of $B_r = 0.5$, two time frames are presented in the two bottom rows. After 428 Ma of simulation time the dense layer hasn't been separated into piles, but its surface topography has been altered by the convective motions within the layer, and the cold downwellings that land on top of the layer. After 428 Ma of simulation time, we see piles forming for the model with $B_r = 0.5$, with some material being entrained through the thin tails rising from its sides and top surface.

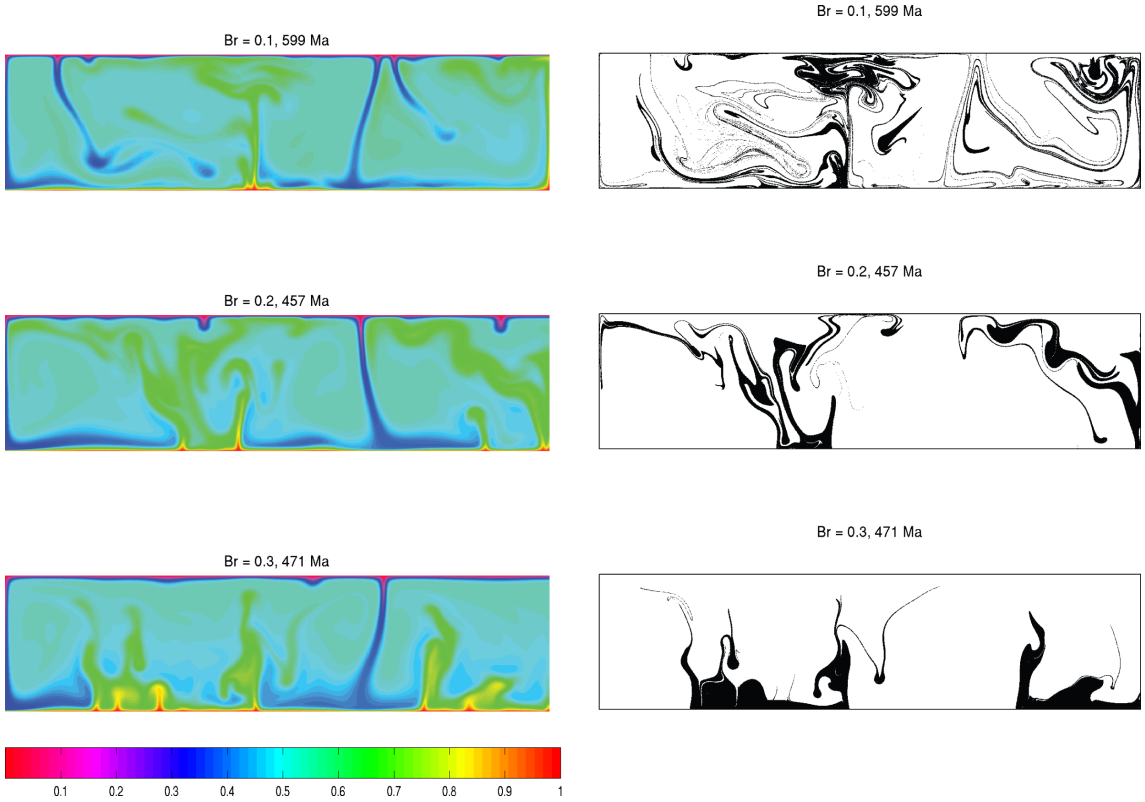

Figure 6.2: The temperature field (*left*) and the distribution of the dense heterogeneous layer (*right*) after approximately 500(±50) Ma of simulation time. The Rayleigh number is $Ra_0 = 10^7$. Buoyancy ratios increase downwards: $B_r = 0.1$, 0.2, and 0.3, corresponding to density differences between the dense layer and the ambient material of $\frac{\triangle \rho_{ch}}{\rho_1^1} = 0.42\%$, 0.84%, and 1.26%. The viscosity ratio between the two materials $\frac{\mu_1^1}{\mu_1^2} = 1$, and the viscosity ratio due to temperature variations $\frac{\mu_0^1}{\mu_1^1} = 1$. Number of mechanical elements in vertical direction = 100. Number of thermal per mechanical elements = 3x3.

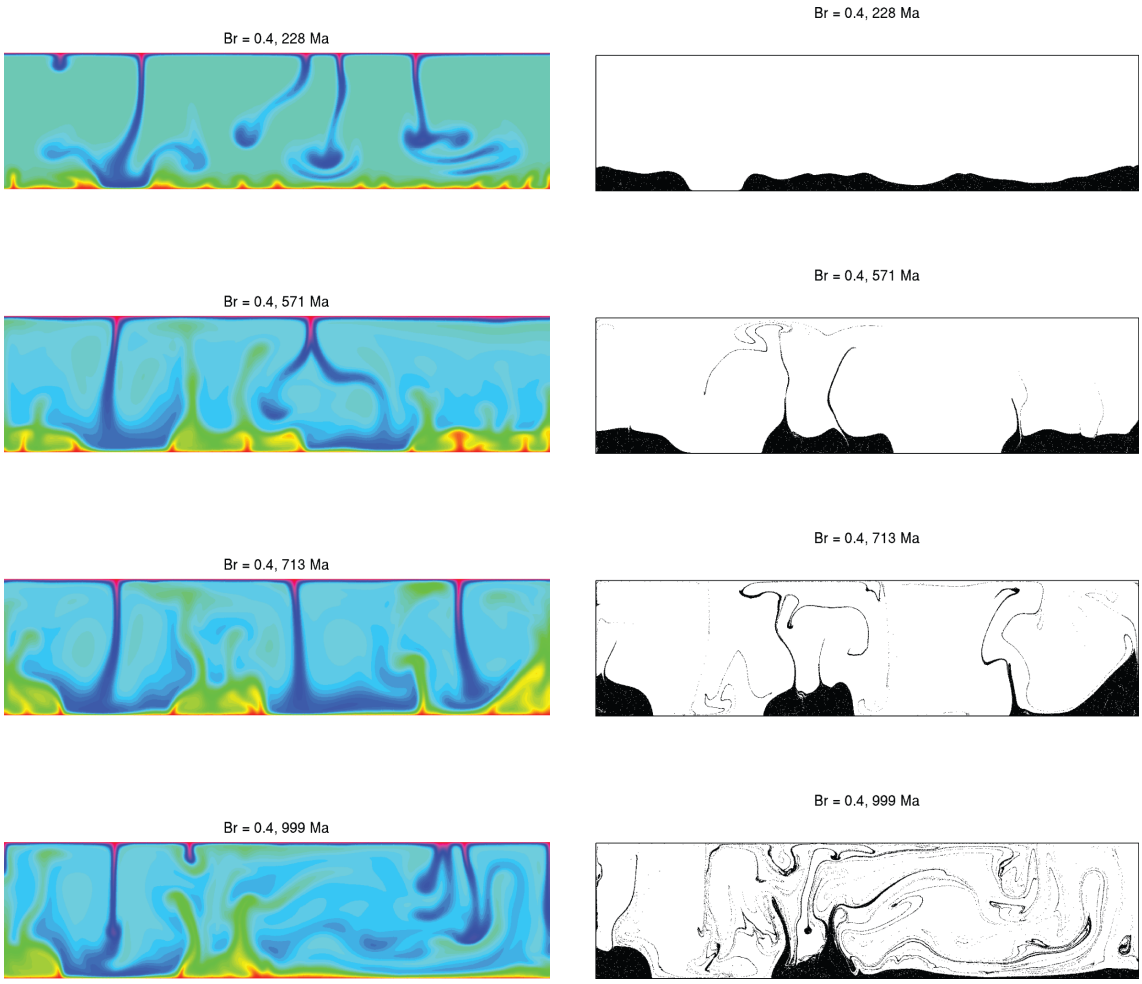

Figure 6.3: Time evolution of the temperature field (*left*) and the distribution of the dense heterogeneous layer (*right*). The Rayleigh number is $Ra_0 = 10^7$. Buoyancy ratio $B_r = 0.4$, corresponding to a density differences between the dense layer and the ambient material of $\frac{\triangle \rho_{ch}}{\rho_1^1} = 1.7\%$. The viscosity ratio between the two materials $\frac{\mu_1^1}{\mu_1^2} = 1$, and the viscosity ratio due to temperature variations $\frac{\mu_0^1}{\mu_1^1} = 1$. Number of mechanical elements in vertical direction = 100. Number of thermal per mechanical elements = 3x3.

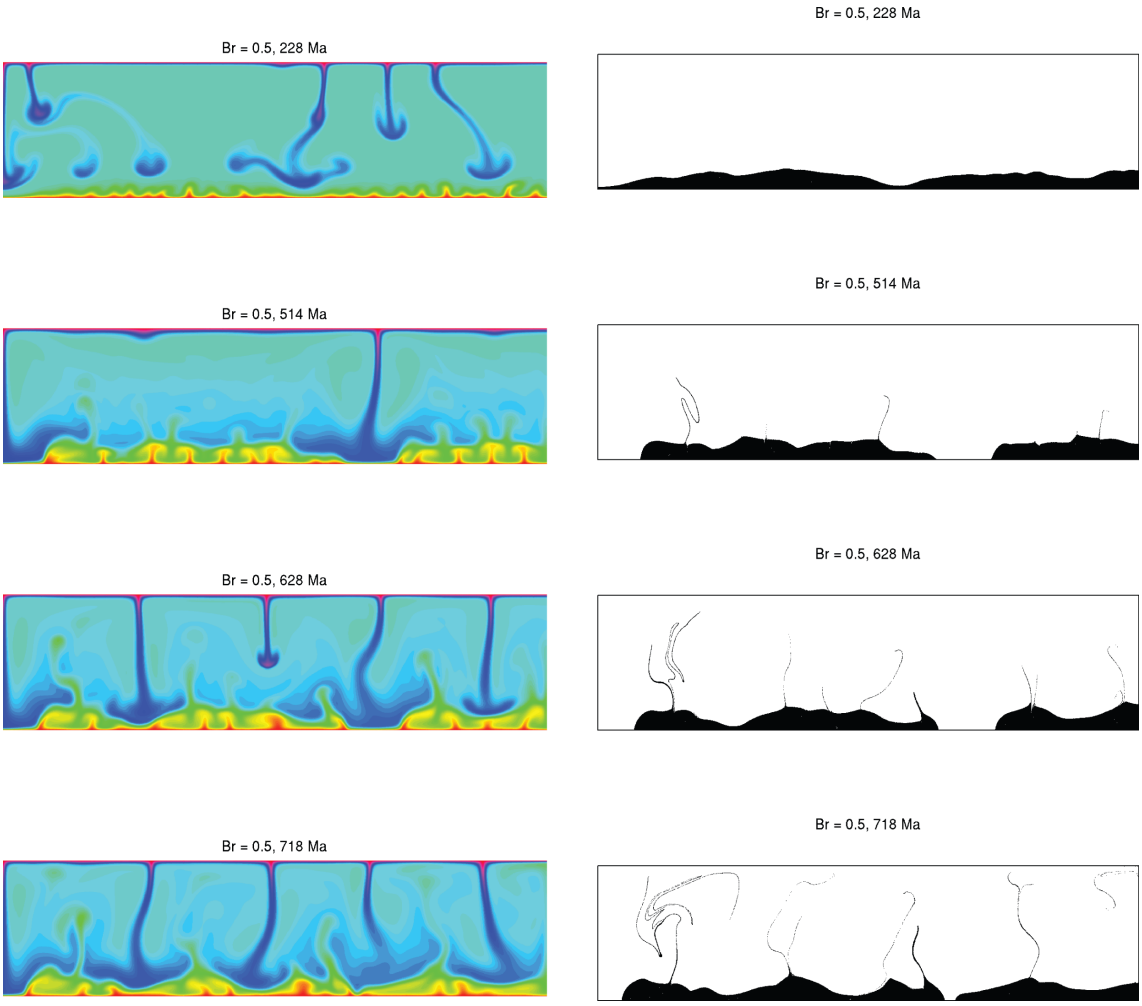

Figure 6.4: Time evolution of the temperature field (*left*) and the distribution of the dense heterogeneous layer (*right*). The Rayleigh number is $Ra_0 = 10^7$. Buoyancy ratio $B_r = 0.5$, corresponding to a density differences between the dense layer and the ambient material of $\frac{\triangle \rho_{ch}}{\rho_1^1} = 2.1\%$. The viscosity ratio between the two materials $\frac{\mu_1^1}{\mu_1^2} = 1$, and the viscosity ratio due to temperature variations $\frac{\mu_0^1}{\mu_1^1} = 1$. Number of mechanical elements in vertical direction = 100. Number of thermal per mechanical elements = 3x3.

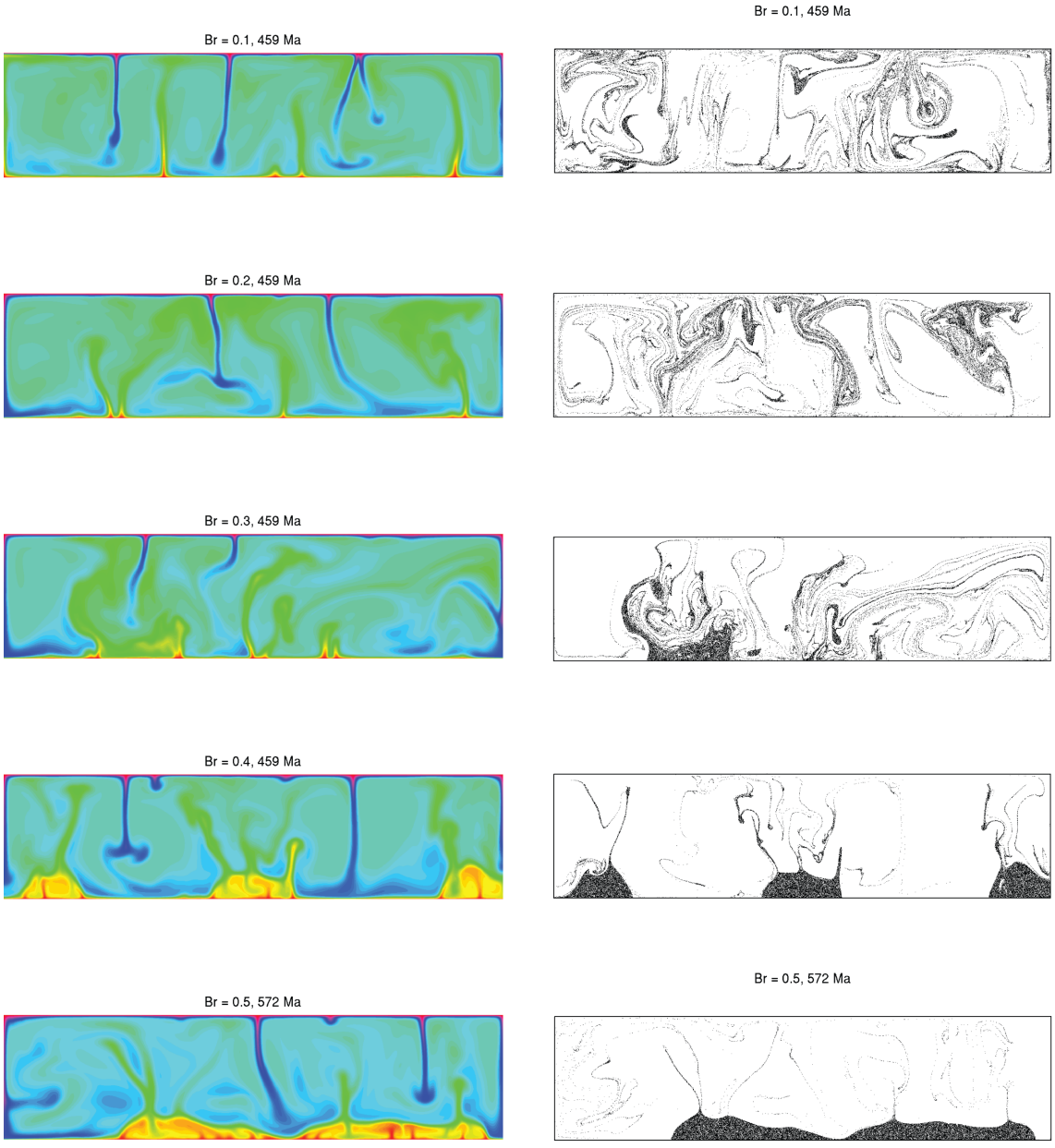

Figure 6.5: The temperature field (*left*) and the distribution of the dense heterogeneous layer (*right*) after 459 Ma of simulation time. The Rayleigh number is $Ra_0 = 10^7$. Buoyancy ratios increase downwards: $B_r = 0.1$, 0.2, 0.3, 0.4, and 0.5, corresponding to density differences between the dense layer and the ambient material of $\frac{\triangle \rho_{ch}}{\rho_1^1} = 0.42\%$, 0.84%, 1.26%, 1.7%, and 2.1%. The viscosity ratio between the two materials $\frac{\mu_1^1}{\mu_1^2} = 10$, and the viscosity ratio due to temperature variations $\frac{\mu_0^1}{\mu_1^1} = 1$. Number of mechanical elements in vertical direction = 75. Number of thermal per mechanical elements = 2x2.

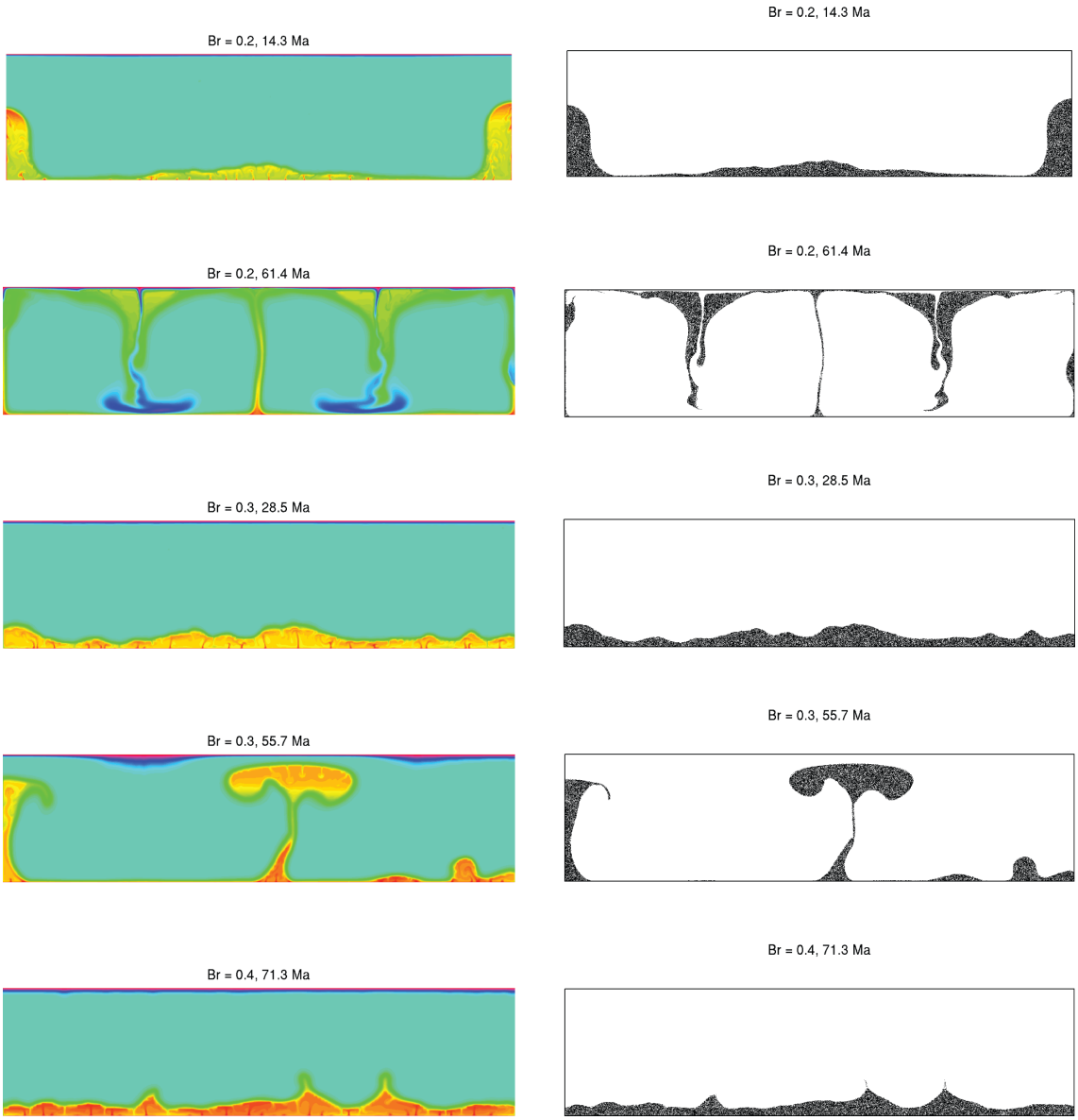

Figure 6.6: Snapshots of the temperature field (*left*) and the distribution of the dense heterogeneous layer (*right*) for models with high viscosity ratio between the two materials $\frac{\mu_1^1}{\mu_1^2} = 1 \cdot 10^3$. The Rayleigh number is $Ra_0 = 10^7$. Buoyancy ratios increase downwards: in the top two rows $B_r = 0.2$, in the second and third rows $B_r = 0.3$, and in the bottom row $B_r = 0.4$. The viscosity ratio due to temperature variations $\frac{\mu_0^1}{\mu_1^1} = 10$. Number of mechanical elements in vertical direction = 75. Number of thermal per mechanical elements = 2x2.

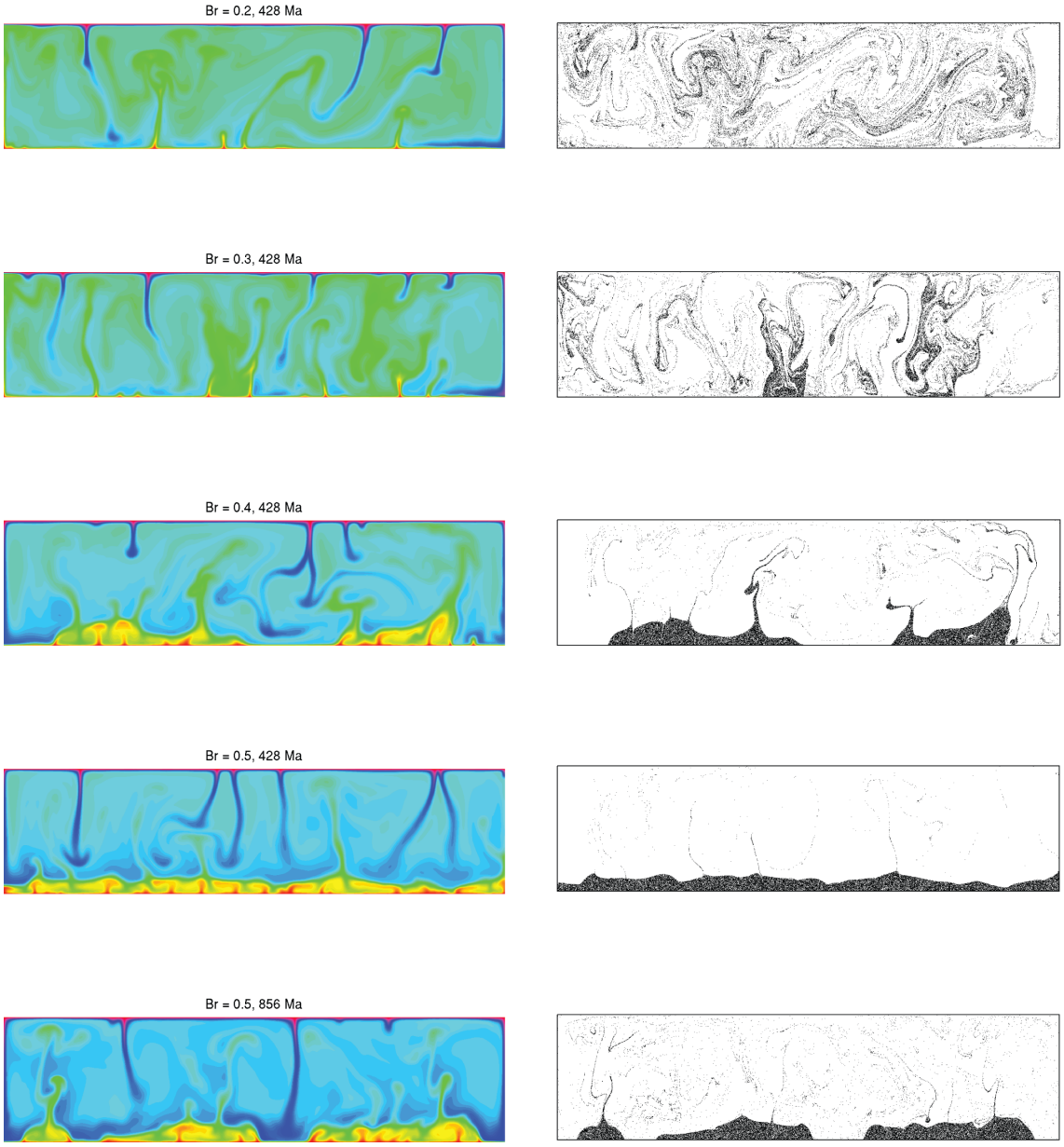

Figure 6.7: The temperature field (*left*) and the distribution of the dense heterogeneous layer (*right*) after 459 Ma of simulation time. The Rayleigh number is $Ra_0 = 10^7$. Buoyancy ratios increase downwards: $B_r = 0.2$, 0.3, 0.4, and 0.5, corresponding to density differences between the dense layer and the ambient material of $\frac{\triangle\rho_{ch}}{\rho_1^1} = 0.42\%$, 0.84%, 1.26%, 1.7%, and 2.1%. In the bottom row, the model with $B_r = 0.5$ is presented after 856 Ma of simulation time. The viscosity ratio between the two materials $\frac{\mu_1^1}{\mu_1^2} = 1$, and the viscosity ratio due to temperature variations $\frac{\mu_0^1}{\mu_1^1} = 10$. Number of mechanical elements in vertical direction = 75. Number of thermal per mechanical elements = 2x2.

6.4 Conclusions

The modelling results presented in this chapter show that the the density difference of at least 1.7% between the dense layer and the ambient material is required in order to achieve gravitational stability of the dense layer for times up to a billion of years. Decreasing the viscosity of the dense layer, or introducing temperature dependence of the viscosity, enhances the entrainment of the dense layer into the ambient material. These results also show that the topography of the thermochemical piles is dynamically supported by the convective motion within the pile. Sweeping of the pile by the cold downwellings of the ambient material significantly influences its shape. We observed plumes of denser material forming both on the top and on the sides of the piles.

We have studied the stability of a heterogeneous material confined in a rectangular box. The simplicity of our model poses limitations for how representative these results are for the case of mantle convection. Presence of lateral boundaries in our model clearly affects the material flow. The downwellings of cold ambient material observed in our models is yet another deviation from observations in nature. Also, a more systematic study is required of a larger range of buoyancy numbers, viscosity ratios between the materials and depth dependent values of viscosity, in order to describe their effects on the stability and shape of the thermochemical piles.

Bibliography

A.E.M. Baptista. Solution of advection-dominated transport by Eulerian-Lagrangian methods using the backwards method of characteristics. 1987.

M. Beuchert, Y. Podladchikov, and T. Torsvik. Long-term stability of Large Low Shear Velocity Provinces (LLSVPs) at the base of the mantle and Velocity Provinces at the base of the mantle and near the equator. 2010.

M.L. Boas. *Mathematical methods in the physical sciences*. John Wiley & Sons New York, 1983.

KE Bullen. The problem of the Earth's density variation. *Bulletin of the Seismological Society of America*, 30(3):235, 1940. ISSN 0037-1106.

M. Dabrowski, M. Krotkiewski, and DW Schmid. MILAMIN: MATLAB-based finite element method solver for large problems. *Geochemistry Geophysics Geosystems*, 9(4): Q04030, 2008. ISSN 1525-2027.

G.F. Davies and U. Christensen. Dynamic Earth: Plates, plumes and mantle convection. *American Journal of Physics*, 69:620, 2001.

J.R. Dormand and P.J. Prince. A family of embedded Runge-Kutta formulae. *Journal of Computational and Applied Mathematics*, 6(1):19–26, 1980. ISSN 0377-0427.

A.M. Dziewonski and D.L. Anderson. Preliminary reference Earth model* 1. *Physics of the earth and planetary interiors*, 25(4):297–356, 1981. ISSN 0031-9201.

A.M. Dziewonski, V. Lekic, and B.A. Romanowicz. Mantle Anchor Structure: An argument for bottom up tectonics. *Earth and Planetary Science Letters*, 299:69–79, 2010. ISSN 0012-821X.

E.J. Garnero and A.K. McNamara. Structure and dynamics of Earth's lower mantle. *Science*, 320(5876):626, 2008.

T. Gerya. *Introduction to numerical geodynamic modelling*. Cambridge University Press, 2010.

B.H. Hager. Subducted slabs and the geoid: constraints on mantle rheology and flow. *Journal of Geophysical Research*, 89(B7):6003–6015, 1984. ISSN 0148-0227.

B.H. Hager, R.W. Clayton, M.A. Richards, R.P. Comer, and A.M. Dziewonski. Lower mantle heterogeneity, dynamic topography and the geoid. *Nature*, 313(6003):541–545, 1985. ISSN 0028-0836.

M. Ishii and J. Tromp. Constraining large-scale mantle heterogeneity using mantle and inner-core sensitive normal modes. *Physics of the Earth and Planetary Interiors*, 146 (1-2):113–124, 2004. ISSN 0031-9201.

C. Jaupart, S. Labrosse, and JC Mareschal. Temperatures, heat and energy in the mantle of the Earth. *Treatise on Geophysics*, 7:253–303, 2007.

R. Jeanloz and S. Morris. Temperature distribution in the crust and mantle. *Annual Review of Earth and Planetary Sciences*, 14:377–415, 1986. ISSN 0084-6597.

E. Knittle. The solid/liquid partitioning of major and radiogenic elements at lower mantle pressures: Implications for the core-mantle boundary region. *The Core-Mantle Boundary Region, Geodyn. Ser*, 28:119–130, 1998.

I.C.P. Kundu. Fluid Mechanics, chapter Dynamic Similarity, 2008.

X.F. Liu, A.M. Dziewonski, et al. Global analysis of shear wave velocity anomalies in the lower-most mantle. *The Core-Mantle Boundary Region, Geodyn. Ser*, 28:21–36, 1998.

D.E. Loper and T. Lay. The core-mantle boundary region. *J. geophys. Res*, 100:6397–6420, 1995.

A.K. McNamara and S. Zhong. Thermochemical structures beneath Africa and the Pacific Ocean. *Nature*, 437(7062):1136–1139, 2005. ISSN 0028-0836.

M. Murakami, K. Hirose, H. Yurimoto, S. Nakashima, and N. Takafuji. Water in Earth's lower mantle. *Science*, 295(5561):1885, 2002. ISSN 0036-8075.

S. Ni, E. Tan, M. Gurnis, and D. Helmberger. Sharp sides to the African superplume. *Science*, 296(5574):1850, 2002. ISSN 0036-8075.

R.L. Panton. Incompressible flow. 1996, 1996.

W.R. Peltier. Mantle viscosity and ice-age ice sheet topography. *Science*, 273(5280):1359, 1996. ISSN 0036-8075.

W.H. Press, S.A. Teukolsky, W.T. Vetterling, and B.P. Flannery. Numerical recipes 3rd edition: The art of scientific computing. 2007.

VN Puchkov. The controversy over plumes: Who is actually right? *Geotectonics*, 43(1): 1–17, 2009. ISSN 0016-8521.

G. Schubert, D.L. Turcotte, and P. Olson. *Mantle convection in the Earth and planets*. Cambridge University Press, 2001.

N.H. Sleep. Mantle plumes from top to bottom. *Earth-Science Reviews*, 77(4):231–271, 2006. ISSN 0012-8252.

B. Steinberger and A.R. Calderwood. Models of large-scale viscous flow in the earth's mantle with constraints from mineral physics and surface observations. *Geophysical Journal International*, 167(3):1461–1481, 2006.

B. Steinberger and R. Holme. Mantle flow models with core-mantle boundary constraints and chemical heterogeneities in the lowermost mantle. *J. geophys. Res*, 113:05403, 2008.

E. Tan and M. Gurnis. Metastable superplumes and mantle compressibility. *Geophys. Res. Lett*, 32(10.1029), 2005.

T.H. Torsvik, M.A. Smethurst, K. Burke, and B. Steinberger. Large igneous provinces generated from the margins of the large low-velocity provinces in the deep mantle. *Geophysical Journal International*, 167(3):1447–1460, 2006. ISSN 1365-246X.

D.L. Turcotte and G. Schubert. *Geodynamics*. Cambridge Univ Pr, 2002. ISBN 0521666244.

RD Van der Hilst, S. Widiyantoro, KC Creager, TJ McSweeney, et al. Deep subduction and aspherical variations in P-wave speed at the base of Earth's mantle. *The Core-Mantle Boundary Region, Geodyn. Ser*, 28:5–20.